國立交通大學

電子工程學系 電子研究所

博士論文

三維的半極性$\{10\bar{1}1\}$平面與非極性$\{10\bar{1}0\}$平面核殼狀氮化銦鎵/氮化鎵多重晶面量子井光電元件之製作與特性研究

Fabrication and Characterization of Three Dimensional Core-shell InGaN/GaN Multi-Facet Qunatum Wells Optoelectronics Devices on Semipolar {10-11} and Nonpolar {10-10} Plane

研究生：張哲榮

指導教授：張俊彥　教授

中華民國一〇二年六月

三維的半極性$\{10\bar{1}1\}$平面與非極性$\{10\bar{1}0\}$平面核殼狀氮化銦鎵/氮化鎵多重晶面量子井光電元件之製作與特性研究

Fabrication and Characterization of Three Dimensional Core-shell InGaN/GaN Multi-Facet Qunatum Wells Optoelectronics Devices on Semipolar $\{10\bar{1}1\}$ Plane and Nonpolar $\{10\bar{1}0\}$ Plane

研 究 生：張哲榮	Student：Jet-Rung Chang
指導教授：張俊彥	Advisor：Chun-Yen Chang

國立交通大學
電子工程學系 電子研究所
博士論文

A Dissertation
Submitted to Department of Electronics Engineering and
Institute of Electronics
College of Electrical and Computer Engineering
National Chiao Tung University
in Partial Fulfillment of the Requirements
for the Degree of
Doctor of Philosophy
in
Electronics Engineering

May 2013
Hsinchu, Taiwan, Republic of China

中華民國一〇二年六月

三維的半極性{10$\bar{1}$1}平面與非極性{10$\bar{1}$0}平面核殼狀氮化銦鎵/氮化鎵多重晶面量子井光電元件之製作與特性研究

研究生：張哲榮 **指導教授：張俊彥 院士**

國立交通大學

電子工程學系 電子研究所

摘要

近年來，一維奈米結構由於擁有以下特點，如降低缺陷密度、增加光取出效率和主動層面積，引起廣大的研究興趣。此論文中，我們提出了核殼結構奈米柱光電元件，即奈米柱被有著多重奈米面的銦氮化鎵/氮化鎵多層量子井包覆，其有多重發光波長的特性，且在沒有螢光粉的情況下，仍能發出自然白光。製造方法如下：首先，利用奈米壓印的方式製造出氮化鎵奈米柱立於氮化鎵 c 平面上，這些奈米柱排列成十二重對稱的光子準晶體圖樣；接下來奈米柱樣品經歷重新成長，將多重量子井成長在奈米柱上且產生晶面。重長後的奈米柱，上部金字塔型頂端為半極性{10$\bar{1}$1}平面族，下部側壁為非

極性$\{10\bar{1}0\}$平面族，兩種平面族圍住整個箭頭形狀的奈米柱。同時，傳統(0001) c 平面上既存的極化效應亦可被成長半極性以及非極性面抑止。我們近一步探討銦含量在多重量子井奈米面上分布的情形,主要有兩種模型描述奈米柱上不同銦含量分佈：(一)質量傳輸模型，包含不同平面有不同濃度含量的表面擴散過程，和同一平面上有漸變濃度分布的氣相擴散過程；(二)表面適性模型,包含晶面交界處化學位能降低,和產生新的平面族使應力釋放,進而使銦濃度提高,故核殼結構奈米柱上不同位置的銦含量有顯著的差異。降溫亦使銦含量有顯著的提升。歸納以上，核殼結構奈米柱因為銦含量在多重奈米面上有不同的分布，具多重發光波長的特性，且調變重長參數可調變其色溫。此外，在核奈米柱排列成十二重光子準晶體結構研究中，亦可發現光激發雷射現象,特別是我們發現多重波峰雷射行為以及隨機雷射的特性。經過 FDTD 模擬的理論計算成功解釋不規則的共振訊號來自十二重光子準晶體結構排列。進一步，實驗結果觀察到激發臨界能量和面積尺寸大小成反比，這證明屬於隨機雷射的特性。

Fabrication and Characterization of Three Dimensional Core-shell InGaN/GaN Multi-Facet Qunatum Wells Optoelectronics Devices on Semipolar $\{10\bar{1}1\}$ and Nonpolar $\{10\bar{1}0\}$ Plane

Student: Jet-Rung Chang **Advisor: Prof. Chung-Yen Chang**

Department of Electronics Engineering and Institute of Electronics
National Chiao Tung University

Abstract

Recently, one-dimensional structures are attracting much interest in the reduction of dislocations, the promotion of light extraction efficiency and the enlarged active area. Further, high-efficiency full-color light sources with high brightness and low power consumption are required for mobile device displays. For full-color display applications, inorganic compound semiconductors have many advantages over organic materials, including high carrier mobility and radiative recombination rate, as well as long-term stability and reliability. However, conventional inorganic thin-film LEDs emit only a single color that is determined by the quantum well layer thickness and composition. Achieving multiple color generation from inorganic LEDs on a substrate is a major obstacle to using inorganic semiconductors in full color displays.

To overcome this obstacle, we used multifaceted gallium nitride (GaN) nanorod arrays with $In_xGa_{1-x}N/GaN$ MQWs anisotropically formed on the nanorod tips and sidewalls.

In this thesis, phosphor-free Core-shell semipolar (10-11) and nonpolar (10-10) InGaN/GaN core-shell nano-LEDs have been successfully demonstrated. A core-shell nanorod includes a shell of InGaN/GaN multi-quantum wells (MQWs) and a core of GaN nanorod. One thing worth noticing is that polychromatic emission with color temperature about 6,000 K (a natural white light) was observed. A core-shell nanorod includes a shell of InGaN/GaN multi-quantum wells (MQWs) and a core of GaN nanorod. The fabrication procedure as follows: The nanorods arrays arrange in a 12-fold symmetric photonic quasicrystal (PQC) pattern on *c*-plane GaN template were fabricated by nano-imprint lithography, and followed by the regrowth of MQWs on the crystalline facets of nanorods. After regrowth, each core-shell nanorod with arrow shape is composed of nonpolar $\{10\bar{1}0\}$ facets on sidewalls and semipolar $\{10\bar{1}1\}$ facets on a pyramidal top. Accordingly, the polarization effects can also be suppressed by growing semipolar and nonpolar planes of nanorods. The core-shell nanorod with an inhomogeneous indium content distribution could be realized by two mechanisms: One is the mass transport model, including the different surface diffusion constants cause the different indium incorporation efficiency on semipolar and nonpolar planes. In the other hand, the gradient indium distribution on each facet is influenced by the gas phase diffusion. The other one is the surface modification model, including the lower chemical potential at the intersection of growth planes, and strain relaxed by the new-born facets. Therefore, whole core-shell nanorod has the obvious difference of indium incorporation efficiency distribute from the bottom to top portion of nanorods.

In addition, a higher indium content of nanorods was also attained by lowering the regrowth temperature, whereas the degraded sidewalls of core-shell nanorods were caused by the lower species mobility. As a result, the polychromatic emission will be formed and the color temperature value can be tuned by the different regrowth parameters of MQWs nano-facets on nanorods. A phosphor-free white light emission have been achieved by the core-shell nanorods technology.

Worth a mention was that the random lasing action was achieved by nanorods arranged in a12-fold PQC pattern. We have observed a lasing action in an optically pumped 12-fold symmetric quasicrystal nanorod arrays. Under optical pumping, multiple lasing peaks emerged from broad emission background. The irregular multiple lasing wavelengths and the inverse dependence of threshold pump intensity on pump spot area resembles the characteristics of random lasing. The irregularity of resonant peaks is qualitatively explained by a simplified FDTD simulation.

誌 謝

時光荏苒，一轉眼我在交大已經過了十年多的求學生活，這一次真的要畢業了。這一刻即將來臨，穿上博士畢業服那一刻，心情頓時百感交集。

在研究所求學期間，非常感謝指導教授 張俊彥院士，能夠成為老師的學生深感榮幸。感謝老師的細心指導，提供了很好的研究環境與機會，總是在我最無助的時候給了我一股正向的力量，讓我勇敢往前進，持續做對的事情。研究生涯中，我遇到了許多的貴人：感謝郭浩中教授無私奉獻所學及研究資源全力相挺，給予實驗室自由的學術空間以及見解精闢的指導，讓我的研究順利，這一切我會銘記在心；感謝程育人老師教導我嚴謹的研究態度，並且不厭其煩的修改論文與研究方向，在研究中給予正確的研究方向與實驗靈感，還有善解人意與追根究柢的精神讓人深感佩服；感謝楊宗熺學長的細心指導，你的鼓勵與支持讓我有機會完成博士學位。感謝涂博閔同學一句話情義相挺至今，犧牲奉獻陪著大家一起努力做好研究，一路陪著我成長、漫漫長夜的討論與促膝長談至今仍然懷念;很感謝張世邦同學在這些年間願意一起共患難，細心教導我不論是實驗上或生活上的大小事，指引研究上的方向使我們能跟上其他團隊先進的實驗;感謝莊凱麟同學對於學術嚴謹的態度以及如何做完美流暢的報告真的讓我深深佩服；謝謝實驗室各位學長姐在實驗上的鼎力相助，在撰寫碩論和口試期間從旁指導。

更要謝謝實驗室曾經幫助我的同學及學弟妹：感謝昀瑾的合作幫忙，總是在我新接觸題目時給予的許多意見和幫助，陪我一起熬夜趕報告、研究討論，幫我扛了很多繁雜的工作…這個博士學位應當分你一半；感謝聰明的澳客國斌總是能夠旁徵引博解決實驗上遇到各種未知的現象，直到口試前仍間續不斷地幫我完成實驗以及投影片；連帶感謝新夥伴光智在準備口試期間的幫忙；感謝芝羽對實驗

室的付出與關懷，讓我代表全實驗室說聲“謝謝”；感謝同學博文、大為、祐誠、修博、婉儀、小杜、江耀、翌臻，我的博士研究生涯因為有你們而變得豐富寬廣；還有邱鏡學博士、李鎮宇博士、黃延儀博士、許世杰博士、羅廣禮博士，與你們一起研究的生活真的很精彩。還要感謝工研院：宣融經理於實驗上的支持及給予的自由度，讓我無後顧之憂能全心投入做研究；感謝郭 sir 細心的教導，並將元件的功力傳授給我，讓我功率大增；感謝每一位同事及同學在我攻讀博士期間能體諒與支持，謝謝林董、郭大哥、寶珠姐、阿美姊、嬤嬤桑、阿芳姊、小媽、阿香姊、訓志、宥萱、趙博、傅博、方博、廖博、胡博；還要感謝前輩照顧。另外，也感謝口試期間給予細心指導的張翼教授、綦振瀛教授、洪瑞華教授、陳冠能教授、羅廣禮研究員，這些寶貴的建議將使本論文更加完整。

最後，感謝我的爸媽提供我無後顧之憂的讀書環境，還有阿公、阿嬤、妹妹、姑姑、姑丈、阿姨、姨丈及眾多親友團，有你們的鼓勵，讓我能全心全力的完成博士學位，真的很感謝你們。以及多年來默默陪伴的欣穎，感謝有妳陪我一起度過這充實的學生時光。最後最後，將這本書獻給關心我支持我的每一個人，由衷的謝謝你們。

張哲榮 于 102 年 6 月 06 日

交通大學電子工程研究所

Eco-Electronics Research Group

ECO ELECTRONICS
NATIONAL CHIAO TUNG UNIVERSITY

Contents

Table Captions

Figure Captions

Chapter 1

Introduction

1.1 Specific Properties of Gallium-Nitride (GaN) Based Devices

The III-nitrides are a remarkable material system. With direct bandgap (Eg), III-nitrides are spanning from the deep ultraviolet (InN, Eg = 0.7 eV) through the ultraviolet (GaN, Eg = 3.4 eV) and visible to infrared (AlN, Eg = 6.0 eV) range. There have been great research interests in GaN material due to its promising applications in UV to blue optoelectronic devices and strong emission properties.

GaN based light-emitting diodes (LEDs) were applying for many aspects in daily life, *e.g.*, traffic lights, indoor lighting, liquid crystal display (LCD) backlighting, architecture illumination, *etc*. For global energy savings, LEDs was a new light source, but LEDs also had their own drawbacks and challenges, as stated in the following: the external quantum efficiency as a function of emission wavelengths in the visible range for LEDs was shown in Figure 1-1. Above 450 nm, UV and blue LEDs had the external quantum efficiency about 30-40%, but around 525 nm green LEDs only reach 10-20%, mainly due to quantum confined Stark effect (QCSE) became stronger at longer wavelengths, this is so-called green gap. The same as AlGaInP for red LEDs also became very dim in the green emission [1]. There are many factors have effect on EQE from fabrication flow chart of LED:

$$\eta_{EQE} = \eta_{IQE} \times \eta_{Ext} \times \eta_{Elect} \tag{1.1}$$

where η_{EQE} is the EQE, η_{IQE} is the internal quantum efficiency (IQE), η_{Ext} is the light extraction efficiency, η_{Elect} is the electrical loss.

Table 1-1 shows the standard red, green and blue LEDs efficiency of 12 mil chip size at injected current 20 mA with carrier density about 2×10^{17} cm^{-3}. If the IQE of green LED could be improved the realization of full collar LED is very promising. Conventional LEDs and LDs were usually grown on polar *c*-plane GaN, and the strained quantum well structures were grown along the polar direction. However, its related devices have a significant problem with strong built-in electric fields caused by both spontaneous and piezoelectric polarization, bending the energy bands of the InGaN active region, as shown in Figure 1-2 (a). These electric fields lead to a spatial separation of the electron and hole wavefunctions, it is the well-known QCSE. QCSE results in a reduced radiative recombination rate to lower the internal quantum efficiency and causes a large blue shift in the electroluminescence with increasing drive current. It is expected that nonpolar planes would eliminate QCSE, as shown in Figure 1-2 (b). The strain-induced polarization can be avoid by the employment of nonpolar planes, when the growth direction perpendicular to the polar *c*-axis. As the computed polarization charge, semipolar planes also have the similar effects for nonpolar planes to mitigate QCSE [2], as shown in Figure 1-3.

Crystal structure of GaN is most stable as the hexagonal wurtzite (WZ) type in space group $P6_3mc$. There are three low index faces compose in the hexagonal structure, including polar (0001) +*c*-plane (Ga-face), $(000\bar{1})$ –*c*-plane (N-face), nonpolar $(11\bar{2}0)$ *a*-planes and $(1\bar{1}00)$ *m*-planes. The high index facets such as semipolar $(10\bar{1}3)$, $(10\bar{1}1)$ and $(11\bar{2}2)$ planes are inclined to the [0001] polar direction, as shown in Figure 1-4.

On the other hand, the lighting efficiency decreases in long emission InGaN/GaN multi-quantum wells (MQWs) with increasing indium content. There are mainly three mechanisms to cause the strain relaxation including phase separation, plastic relaxation and elastic relaxation. The spinodal decomposition mainly caused by the thermodynamic properties of InGaN alloy. The large interatomic spacing difference (11%) between InN and GaN results in phase separation [3]. In addition, a high indium content of InGaN films requires fairly low growth temperatures also owing to the thermodynamic properties. At quite low growth temperature, InGaN films grow with high indium content but poor crystalline quality [4]. Moreover, InGaN thin film had pseudomorphic growth on the underlying GaN template. The deleterious dislocations lead to plastic strain relaxation when InGaN films exceed its critical thickness. The InGaN/GaN MQWs grown on three dimensional structures induce the elastic relaxation by Stransky-Krastanov transition [5]. The problem of low indium incorporation efficiency is exist in all crystllographic orientation of WZ stucture. However, several groups proposed semipolar planes such as $(10\bar{1}3)$, $(10\bar{1}1)$ and $(11\bar{2}2)$ with comparable high indium incorporation efficiency and little polarization effects than that observed in *c*-plane GaN [6-8].

1.2 Perspectives of GaN Based Polychromatic Nano-emitters

Conventionally devices are built in two-dimensional *c*-plane GaN structures but have the large QCSE. Several groups had proposed many methods to solve the QCSE in polar *c*-plane, such as thinner QW thickness [9], composition-graded barrier [10], pre-strain layer [11] and p-InGaN barrier [12], but the results were limited. Semipolar or nonpolar GaN substrate also had been proposed to avoid the polar orientation [8], but the cost was too high. In recent years, devices with one-dimensional nanostructure have gained substantial attention for their interesting properties and potential applications [13, 14]. The one-dimensional structures can be fabricated by top-down patterned etching like photolithography or bottom-up self-assembled growth processes such as the vapor-liquid-solid (VLS) growth mechanism [15].

The polychromatic emission of nano-emitters had been investigated by many groups. By using molecular beam epitaxy (MBE), different emission color control from blue to red with nanocolumn diameter from 143 nm to 270 nm of InGaN/GaN nanocolumn arrays [16]. Recent work to generate a phosphor-free natural white light emission (6000K) was using self-assembled GaN nanorods array with thick InGaN nanodisks to fabricate full-color InGaN nanodisk emitters [17]. By using metal organic chemical vapor deposition (MOCVD), Funato *et. al.* proposed phosphor-free monolithic polychromatic LEDs with different emission wavelength mainly owing to the different incorporation efficiency on the multi-crystalline micro-facets. Therefore, the fabrication of monoclinic full-color nano-emitters is expected to replace the blue LEDs with yellow phosphor to generate white light emission.

1.3 Motivation

In recent years, significant interest has developed in the potential of using one dimensional GaN nano structures as an alternative design to improve the efficiency of the commonly-used planar structure GaN light emitting diodes. The nanopillar structure provides several advantages over the planar structure. The nanopillar exhibits a significantly reduced defect density because it has only a small area of contact with the growth template. This small footprint reduces strain from the lattice and thermal expansion coefficient mismatch between the GaN nanopillar and the growth template [19-21], thus reducing piezoelectric polarization and improving electron-hole recombination efficiency [22, 23]. The reduced strain also allows for higher In concentration in InGaN/GaN MQWs for green-red color emission applications [16, 17, 24]. These advantages have been demonstrated in MQWs grown in the nanopillar axial direction, which is often the c-axis crystal direction. The nanopillar offers an additional option to grow MQWs on the pillar surfaces in a core-shell geometry. These surfaces can be nonpolar or semipolar crystal planes with zero or low polarization fields. The MQWs grown on these planes have a lower carrier density dependent wavelength change and a higher radiative recombination efficiency [25-27]. This structure can also result in a much larger active surface area than found in MQWs grown on the nanopillar axial direction. Due to the nature of their three dimensional structure, the growth and emission properties of core-shell MQWs can vary with different crystal planes and require investigation.

GaN nanopillars can be fabricated by either a bottom-up or top-down approach. The former grows vertical nanopillars upward from a substrate by molecular beam epitaxy or hydride vapor phase Epitaxy [16-18, 24]. The nanopillars are often formed by self-assembly. This approach provides less control over the size and location of nanopillars. The latter approach creates nanopillars by etching a flat substrate downward with circular etching masks [28], providing improved dimension and pattern control. The etching process usually produces damaged surfaces that may require repairs. Here, we report a fabrication process using top-down patterned etching followed by an epitaxial regrowth to create crystalline core-shell MQW nanopillar arrays.

As described in the above sections, the difficulties in growing devices on *c*-plane GaN with long wavelength emission is due to the QCSE along [0001] polar-direction. The employment of nonpolar or semipolar planes which are inclined or perpendicular to polar *c*-planes can eliminate or mitigate the QCSE. The indium phase separation of InGaN alloy exists in all crystalline direction of WZ structure; however, the indium incorporation efficiencies are different from different orientations. It is expected that a monolithic light emission can be fabricated by phosphore-free nano-emitters. In order to fabricate high lighting efficiency nano-emitter, we use one-dimensional core-shell nanorod structure which has the following advantages: the reduction of dislocations, the promotion of light extraction efficiency and the enlarged active area.

The lighting efficiency of LEDs is determined by the product of the internal quantum efficiency and the light extraction efficiency. The internal quantum efficiency is defined as the ratio of the number of injected electrons to that of electron-hole pairs which emitted from active area. The light extraction efficiency is defined as the ratio of the number of generated photons to the number of photons extracted from the devices.

According to the previous study [18], GaN nanorods have both $\{10\bar{1}1\}$

semipolar and $\{10\bar{1}0\}$ nonpolar planes under the MOCVD growth process. At the same time, the geometric structure in three-dimension of core-shell nanorods also enlarge the active area which is compared to the planar structures. Therefore, the two factors for the promotion of internal quantum efficiency are predictable.

In comparison to planar thin film devices, GaN-based LEDs with photonic quasicrystal (PQC) structures are attracting much interest [17]. The motivation for using a PQC structure is to promote the light extraction efficiency in optical devices. For the large refractive index difference of GaN-based semiconductor (n=2.5) and air (n=1), most of the light rays emitting from the planar active region are total internally reflected at semiconductor's surface. Therefore, enhancement of the light extraction efficiency is especially important. The critical anlge (θ_c=23.6°) for total internal reflection is obtained by using snell's law

$$\bar{n}_{air}\sin 90^\circ = \bar{n}_{GaN}\sin\theta_c \qquad (1.2.)$$

In this thesis, there is an open window for growing high efficiency optical devices with monolithic polychromatic emission by using core-shell InGaN/GaN MQWs grown on GaN nanorod. The experimental results, the specific properties of core-shell nanorods and the brief conclusions and future works are available in the following chapters.

1.4 References

[1] S. Nakamura, "Current status of GaN-based solid-state lighting," *MRS bulletin*, vol. **34**, pp. 101-107, 2009.

[2] H. Masui, *et al.*, "Nonpolar and Semipolar III-Nitride Light-Emitting Diodes: Achievements and Challenges," *Electron Devices, IEEE Transactions on*, vol. **57**, pp. 88-100, 2010.

[3] S. Keller, *et al.*, "Growth of bulk InGaN films and quantum wells by atmospheric pressure metalorganic chemical vapour deposition," *Journal of crystal growth*, vol. **170**, pp. 349-352, 1997.

[4] J. Speck and S. Rosner, "The role of threading dislocations in the physical properties of GaN and its alloys," *Physica B: Condensed Matter*, vol. **273**, pp. 24-32, 1999.

[5] M. Leyer, *et al.*, "The critical thickness of InGaN on (0001) GaN," *Journal of crystal growth*, vol. **310**, pp. 4913-4915, 2008.

[6] N. Okada, *et al.*, "Growth of Semipolar (11-22) GaN Layer by Controlling Anisotropic Growth Rates in r-Plane Patterned Sapphire Substrate," *Applied physics express*, vol. **2**, pp. 091001-1, 2009.

[7] R. Sharma, *et al.*, "Demonstration of a semipolar (1013) InGaN/GaN green light emitting diode," *Applied Physics Letters*, vol. **87**, pp. 231110-231110-3, 2005.

[8] B. Gil, "Symmetry properties and anisotropic excitonic response for GaN films grown on semipolar (11-22)-, (10-11)- and (10-13)-oriented GaN substrates," *Applied Physics Letters*, vol. **90**, pp. 121903-121903-3, 2007.

[9] J. Bai, *et al.*, "Influence of the quantum-well thickness on the radiative recombination of InGaN/GaN quantum well structures," *Journal of Applied Physics*, vol. **88**, p. 4729, 2000.

[10] T. Onuma, *et al.*, "Improved Emission Efficiency in InGaN/GaN Quantum Wells with Compositionally-Graded Barriers Studied by Time-Resolved Photoluminescence Spectroscopy," *Japanese Journal of Applied Physics Letters*, vol. **42**, pp. 1369-1371, 2003.

[11] C. Huang, *et al.*, "Enhanced efficiency and reduced spectral shift of green light-emitting-diode epitaxial structure with prestrained growth," *Journal of Applied Physics*, vol. **104**, pp. 123106-123106-7, 2008.

[12] J. Ryou, *et al.*, "Control of quantum-confined Stark effect in InGaN¢A GaN multiple quantum well active region by p-type layer for III-nitride-based visible light emitting diodes," *Applied Physics Letters*, vol. **92**, p. 101113, 2008.

[13] F. Qian, *et al.*, "Gallium nitride-based nanowire radial heterostructures for

nanophotonics," *Nano Letters*, vol. **4**, pp. 1975-1979, 2004.

[14] L. Gangloff, *et al.*, "Self-aligned, gated arrays of individual nanotube and nanowire emitters," *Nano Letters*, vol. **4**, pp. 1575-1579, 2004.

[15] R. Yan, *et al.*, "Nanowire photonics," *Nature photonics*, vol. **3**, pp. 569-576, 2009.

[16] H. Sekiguchi, *et al.*, "Emission color control from blue to red with nanocolumn diameter of InGaN/GaN nanocolumn arrays grown on same substrate," *Applied Physics Letters*, vol. **96**, pp. 231104, 2010.

[17] H. Lin, *et al.*, "InGaN/GaN nanorod array white light-emitting diode," *Applied Physics Letters*, vol. **97**, pp. 073101, 2010.

[18] Z. Zhang, *et al.*, "Effects of symmetry of GaN-based two-dimensional photonic crystal with quasicrystal lattices on enhancement of surface light extraction, " *Applied Physics Letters*, vol. **88**, p. 171103, 2006.

[19] J. Chang, *et al.*, “Strong luminescence from strain relaxed InGaN/GaN nanotips for highly efficient light emitters, ” *Opt. Express*, vol. **15**, p. 9357, 2007.

[20] J. Renard, *et al.*, “Evidence for quantum-confined Stark effect in GaN/AlN quantum dots in nanowires, ” *Phys. Rev. B*, vol. **80**, p. 121305, 2009.

[21] Q. Li and G. Wang, “Strain influenced indium composition distribution in GaN/InGaN core-shell nanowires,” *Appl. Phys. Lett.*, vol. **97**, p. 181107, 2010.

[22] Y. Chang, *et al.*, “High efficiency green, yellow, and amber emission from InGaN/GaN dot-in-a-wire heterostructures on Si(111),” *Appl. Phys. Lett.*, vol. **96**, p. 013106, 2010.

[23] Y. Hong, *et al.*, “Visible-Color-Tunable Light-Emitting Diodes,” *Adv. Mater.*, vol. **23**, p. 3284, 2011.

[24] H. Nguyen, *et al.*, “Controlling Electron Overflow in Phosphor-Free InGaN/GaN Nanowire White Light-Emitting Diodes,” *Nano Lett.*, vol. **12**, p. 1317, 2012.

[25] R. Koester, *et al.*, “M-Plane Core–Shell InGaN/GaN Multiple-Quantum-Wells on GaN Wires for Electroluminescent Devices,” *Nano Lett.*, vol. **11**, p. 4839, 2011.

[26] C. Lee, *et al.*, “GaN/In1−xGaxN/GaN/ZnO nanoarchitecture light emitting diode microarrays,” *Appl. Phys. Lett.*, vol. **94**, p. 213101, 2009.

[27] T. Yeh, *et al.*, “Vertical nonpolar growth templates for light emitting diodes formed with GaN nanosheets,” *Appl. Phys. Lett.*, vol. **100**, p. 033119, 2012.

[28] Q. Li, *et al.*, “ptical performance of top-down fabricated InGaN/GaN nanorod light emitting diode arrays,” *Opt. Express*, vol. **19**,p. 25528, 2011.

Table 1-1. The efficiency of 12 mil standard red, green and Blue LED at injected current 20 mA with carrier density about 2×10^{17} cm^{-3}.

	η_{EQE}	η_{IQE}	η_{Ext}	η_{Elect}
Red	53 %	80 %	70 %	95 %
Green	23 %	**30 %**	80 %	95 %
Blue	57 %	75 %	80 %	95 %

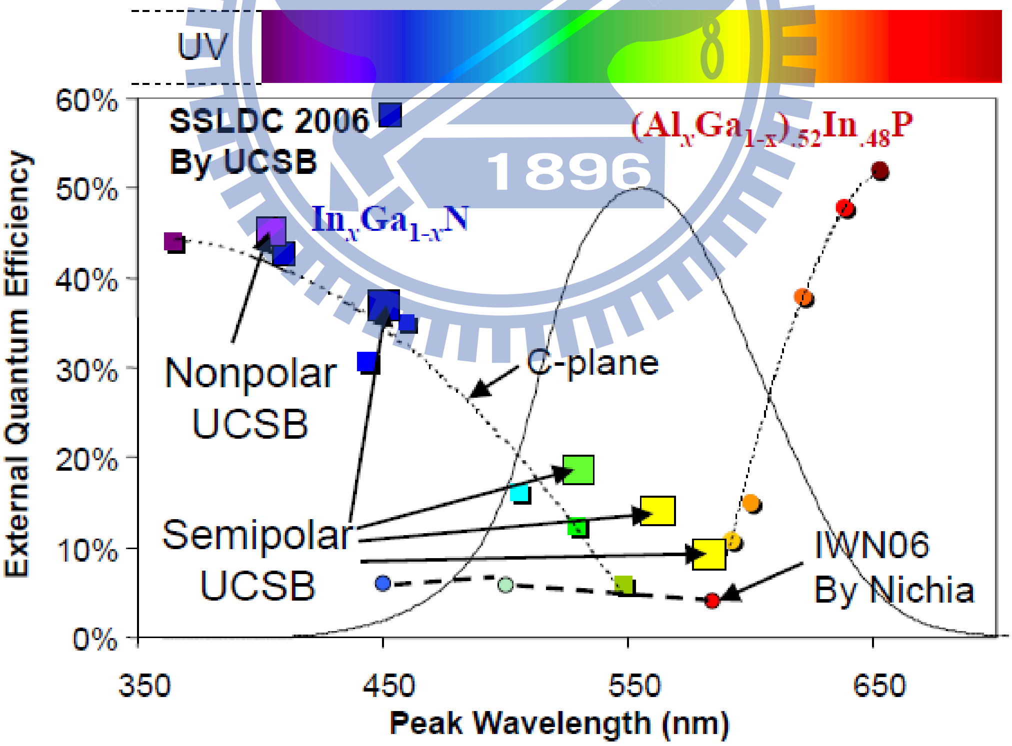

Figure 1-1. External quantum efficiency as a fuction of peak wavelength with two different materials of InGaN/GaN and AlGaNInP MQWs [1].

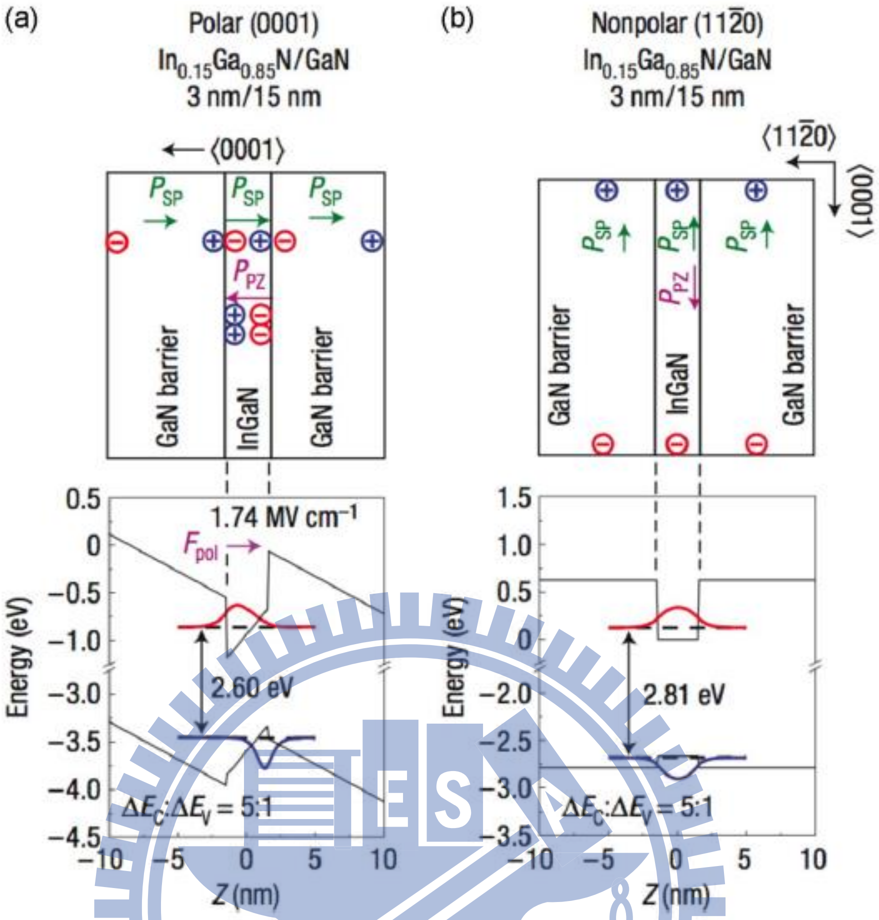

Figure 1-2. The quantume well structures of InGaN/GaN on (a) polar c-axis and (b) nonpolar orientations and theie band diagrams [2].

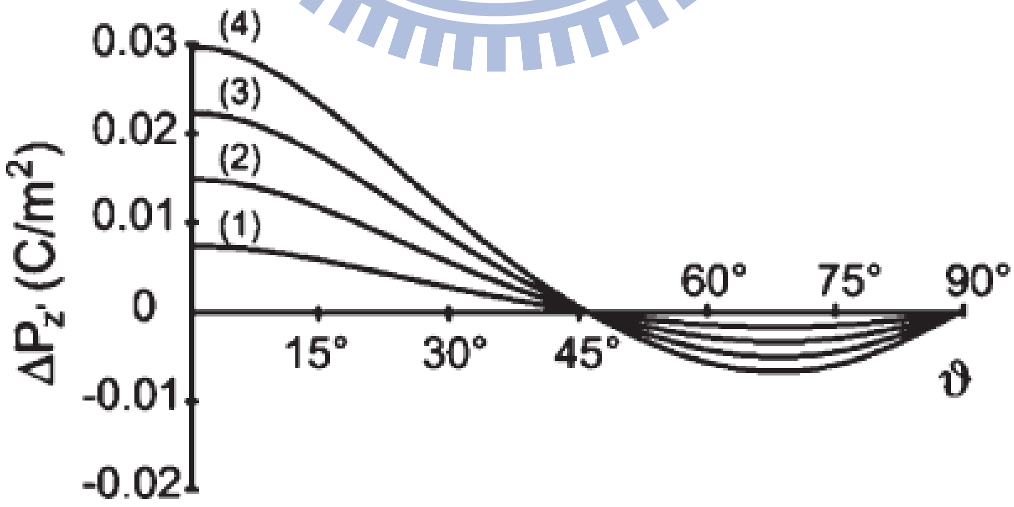

Figure 1-3. Polarization (spontaneous and piezoelctric) effect as a function of tilt angle of the growth plane with respect to polar [0001] direction [2].

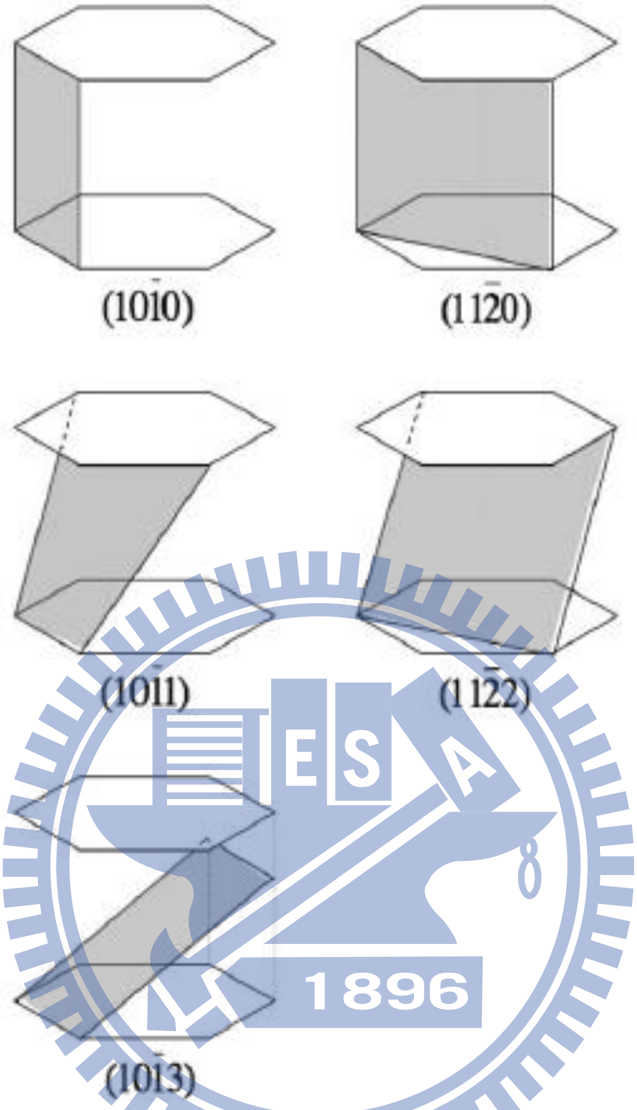

Figure 1-4. Schematic illustration of GaN hexagonal crystal structure which indicate the polar {0001} surfaces, the nonpolar {11-20} and {1-100} surfaces, and the semipolar {10-13}, {10-12}, and {11-22} surfaces [2].

Chapter 2

Experimental Apparatus

2.1 Metalorganic Chemical Vapor Deposition (MOCVD)

Metalorganic Chemical Vapor Deposition (MOCVD) is the most common epitaxial technique used in both industry and research. It has the benefit of high growth rate on large area wafers. One problem with MOCVD is that it requires complicated and sometimes vary hazardous gases in order to produce the epitaxial layer. Compound semiconductors are grown from the surface reaction of organic compounds or metalorganics and hydrides containing the required species. In growing GaN hydride mixture containing ammonia and trimethyl-gallium (TMGa), highly diluted by hydrogen or nitrogen, is led into the reactor separately. Figure 2-1 shows a schematic drawing of the MOCVD subsystem. The vapor pressure of the MO source is a function of temperature. By placing the MO bottle in a bath containing a mixture of water and glycol, the vapor pressure can be controlled over a wide range of temperature. The carrier gas “bubbled” through the MO liquid and transport into the line. The amount of vapor transported into the line depends on the flow rate of the carrier gas (Φ_c), the pressure in the bottle (P_b) and the vapor pressure P_{vap} of the MO (Φ_{MO}). When growing epitaxial films in the reactor, it is of great importance to know how much source material is introduced. Since the volume and the temperature of the source bottle is constant, the perfect gas law can be used to determine the flow rate of MO (Φ_{MO}). During a time interval Δt, $\Phi_{MO} \cdot \Delta t\ \alpha\ n$ moles of source material is defined from the bottle. According to the perfect gas law:

$$\frac{\phi}{P_b} = constant \rightarrow \frac{\phi_{MO}}{P_{vap}} = \frac{\phi_c}{P_s} \tag{2.1}$$

where P_c is the partial pressure of the carrier gas in the bottle. In the gas panel configuration shown in Figure 2-1, the pressure in the bottle is controlled from the following line. The partial pressure of the source gas can be expressed as $P_c = P_b - P_{vap}$. Inserting into Equation 2.1 the flow rate of the MO (in cm^3/min) can be evaluated.

The precursor molecules NH_3 and TMGa are fed in separately into the reactorchamber. In the reactor reactions take place both on the wafer and before the molecules reach the wafer. Formation of the epitaxial layer occurs by the reaction:

$$Ga(CH_3)_3 + NH_3 \rightarrow GaN + CH_4 \tag{2.2}$$

Figure 2-2 illustrates the growth process with impinging precursors and rest products. Due to the low cracking efficiency of ammonia and adatom mobility the growth of GaN is carried out at very high temperature around 1000℃ ~1100℃ to high crystalline quality. Many of the difficulties involving the growth of GaN are due to the high volatility of nitrogen. The pressure of nitrogen in the vapor must not be below a certain value to produce the solid without other phases. If the pressure is too low, a Ga liquid phase is formed resulting in droplet formation on the surface of crystal ($GaN + 3/2H_2 \rightarrow Ga + NH_3$). An alternative precursor to NH_3 for atomic nitrogen is dimethyl-hydrazine [1]. It has successively been used for growth of GaN [2]. Dimethyl-hydrazine has a relatively low decomposition temperature compared to NH_3. At 420℃ it decompose up to 50% [3], while NH3 only 15% at 950℃.

One thing to be mentioned is that MOCVD is a diffusion controlled process, as the region II in Figure 2.3. This regime appears at moderate temperatures. Compared with the chemical reaction regime the mass transport rate of the reactant gaseous species is much lower than that of the chemical reaction, *i.e.* $h_G << k_S$. The coating growth is limited by the mass transport from the bulk gas to the substrate surface. In this case a steep concentration gradient within the boundary layer is generated and the reactant gaseous species are nearly consumed on the substrate surface.

In this regime, the temperature dependence of the growth rate becomes mild, which is attributed to the gaseous species diffusivity. The growth rate of the coating increases linearly with the partial pressure increasing of the reactant gaseous species (p_{react}), which is confirmed through experimental work as shown in Figure 2.3. The growth rate is inversely proportional to the total pressure in the system. The mass transport rate can be considerably enhanced through a decrease in the total pressure. This is the main reason that most CVD processes are operated at reduced pressures. An increase in the gas velocity in the bulk is useful to reduce the thickness of the boundary layer and, hence, results in a more rapid growth rate of coatings.

For the growth of monolithic materials the high growth rate is much more important than the thickness uniformity from an economical view. The MOCVD processes are often performed in the mass transport regime. The higher processing temperatures are used for thermal gradient CVI and forced CVI processes in which fast growth rates are needed to ensure the rapid densification of the composites.

2.2 Nano-Imprint Lithography Equipment

Nanoimprint lithography (NIL) is a novel technology which can achieve flexible dimension range on semiconductor devices. The first publication in 1995 was from Chou *et al.* on thermal NIL. After that, many NIL methods, including thermal nano imprint lithography (NIL), UV NIL and Obducat's proprietary Simultanous Thermal and UV (STU®) imprint process, are developing quickly on past few years. It becomes a significant technology for scientists studying. Helmut Schift defined: *NIL as a parallel patterning method in which a surface pattern of a stamp is replicated into a material coated on a hard substrate by mechanical contact and 3D material displacement, to be used in fields until now reserved to electron beam lithography (EBL) and photolithography (PL).* Nanoimprint lithography (NIL) is a next generation lithography (NGL) candidate technology.

One of the serious issues is contamination the stamp after imprinting process. Obducat's nanoimprint lithography (NIL) technology has solved it by using the Intermediate Polymer Stamp (IPS®). Obducat is the world-leading naoimprint lithography equipment supplier. The Eitre® Nano Imprint Lithography (NIL) series, including Eitre® 3, 6, and 8, is the studying and development machines which offer a flexible and efficient lithography solution. Table 2-1 shows all above have similar functions. There are different on imprinting wafer sizes and suitable for replicating patterns in the micro- and nanometer range. All Obducat nanoimprint lithography (NIL) systems are equipped with standard full area thermal imprint and offers using the patented Soft Press® technology. For example, Figure 2-4 shows the NIL Eitre® 6 facility on National Nano Device Laboratories (NDL). It possesses thermal and UV source to model different patterns. The specific design of the heater which provides a homogeneous temperature distribution across the whole imprint area is embedded in the substrate chuck and the UV source is embedded on the roof over the substrate chuck. The uniform heating and light source make it possible to use a wide range of imprint polymer.

2.3 Inductively Coupled Plasma Reactive Ion Etching (ICP-RIE)

It has been demonstrated that conventional RIE is perfectly capable of etching sub-100 nm structures. The only limitation is its relatively low etch rate, which is normally less than 200 nm min^{-1} for Si. The etching rate in RIE directly depends on plasma density. For the conventional RIE system as shown in Figure 2.5, plasma density increases with increase of RF power. However, increasing RF power will also increase the self-biasing voltage on the cathode where the etching sample is situated. The consequence is the increase of ion bombardment energy, hence deterioration of etching selectivity. This becomes a particularly serious problem in sub-100 nm RIE, because the masking layer is always thin to enable photon or e-beam patterning of polymer resist at sub-100 nm feature dimension.

Inductively coupled plasma (ICP) system has cleverly solved the problem. In an ICP source, the plasma generation is separated from etching chamber, as shown in Figure 2-6. Radio frequency power is coupled into plasma chamber by an induction coil from outside. The sample stage is connected to a second RF power source as an auxiliary RF source to enhance the production of plasma. Electromagnetic field generated by inductive coupling coil can sustain electron cycling movement in plasma for a long period, which has greatly increased ionization probability while keeping the pressure low in the etching chamber. As the sample stage has an independent input of RF power, the self-biasing voltage can be independently controlled. Therefore, an ICP system can produce very high plasma density ($>5\times10^{11}$ cm^{-3}) compared to conventional RIE (10^{8}~10^{10} cm^{-3}), as well as maintain low ion bombardment energy. The conflict between high plasma density and high etch selectivity encountered in conventional RIE systems has been resolved. With such high plasma density and high etching selectivity, high etching rate and deep RIE (DRIE) become possible.

ICP-RIE has been widely used for etching other materials, especially the III-nitride semiconductors. The ICP with high plasma density offers much higher etch rate and selectivity than it is possible by conventional RIE. For example, GaN or sapphire is known to be difficult to etch. With a conventional RIE, the etch rate is less than 5nm min^{-1}. Using an ICP-RIE the etch rate is nearly 10 times enhanced. Inductively coupled plasma systems are widely used to etch III–V semiconductor materials which are of great importance in high frequency and optoelectronic applications currently.

2.4 Electron Microscopy

2.4.1 Scanning Electron Microscopy (SEM)

It is worthwhile to understand the technique and type of instrument of SEM. Very simply; the SEM scans a sample with a beam of electrons that interact with the sample. Some of those electrons and other electrons generated during this process escape from the sample and reach a detector. The number of electrons that reach the detector at each point on the sample depends on the topology of the sample and the atomic weight of the atoms at the surface, and these variations in signal strength lead to image formation.

A SEM column consists of an electron gun, one or two condenser lenses, an objective aperture, and an objective lens [4]. The electron gun produces a source of electrons and accelerates the electrons to energy of 1~30 keV. This occurs in a vacuum environment ranging from 10^{-4} to 10^{-10} Torr. The electron lenses in the column are used to demagnify the image of the gun crossover and focus a final spot on the specimen on the order of 1 nm~1 μm with a beam current in the range of 1pA~1μA. The condenser lens controls the amount of demagnification and the probe forming or objective lens focuses the final probe on the specimen. A schematic of a typical SEM is shown in Figure 2-7.

The lens and aperture system in the column provide control of the beam through manipulation of the probe diameter, probe current, and convergence angle. These three parameters can be controlled and used to achieve high depth-of-field, high-resolution, or high beam current for x-ray microanalysis. A small convergence angle is needed for high depth-of-field imaging and can be obtained with a small objective aperture and a long working distance. High resolution imaging requires a small probe size which can be obtained with a strong condenser lens, an objective aperture, and a short working distance. Finally, x-ray microanalysis may require higher beam currents which can be obtained by weakening the condenser lens and removing the objective aperture.

The interactions between the electron beam and the specimen in a SEM are the source for a wide variety of signals that can be collected and used to characterize the sample as in Figure 2-8. The electron beam-specimen interactions are a result of elastic and inelastic scattering processes that occur simultaneously within the sample. The region in which the electrons interact with the specimen is called the interaction volume. The interaction volume can extend from a few nanometers to a few microns below the surface depending on the beam and sample parameters. Elastic scattering events produce large angular changes in the trajectory of the beam electrons inside the sample, but result in little or no change to the energy of the electron, thus giving rise to the overall shape of the interaction volume. Elastic scattering primarily gives rise to backscattered electrons (BSE). Inelastic scattering events result in the transfer of energy from the beam electrons to the tightly bound inner-shell electrons and loosely bound outer-shell electrons of the atoms in the specimen with very little angular change in the trajectory of the beam electron. During a single inelastic scattering event the beam electron can transfer an amount of energy ranging from less than 1 eV to the full energy carried by the beam electron. Inelastic scattering limits the range of the electrons within the specimen by eventually reducing the electron energy to zero. Inelastic scattering gives rise to phonons (lattice vibrations), plasmons (electron oscillations), auger electrons, characteristic x-rays, continuum x-rays, secondary electrons (SE), and electron hole pair (EHP) generation. EHP generation in a material with a bandgap is the basis for the EBIC and CL signals.

The incident electrons interact with a certain volume of the sample called the interaction volume. There are numerous analytical expressions that have been used to model the size and shape of this interaction volume, which will not be covered here. The interaction volume depends on a number of factors, including the beam energy, the atomic number of the specimen, and the angle the incoming probe beam makes with the sample surface. The number of backscattered and secondary electrons (BSE and SE) produced will depend on these parameters and others such as the topology of the sample, and will result in the image contrast observed. Several detection systems are depicted in Figure 2-9 and 2-10.

2.4.2 Transmission Electron Microscopy (TEM)

The transmission electron microscopy (TEM) is used to characterize the microstructure of materials with very high spatial resolution. Information about the morphology, crystal structure and defects, crystal phases and composition, and magnetic microstructure can be obtained by a combination of electro-optical imaging (2.5Å point resolution), electron diffraction, and small probe capabilities. The trade-off for this diverse range of structural information and high resolution is the challenge of producing very thin samples for electron transmission.

The TEM uses a high energy electron beam transmitted through a very thin sample to image and analyze the microstructure of materials with atomic scale resolution. The electrons are focused with electromagnetic lenses and the image is observed on a fluorescent screen, or recorded on film or digital camera. The electrons are accelerated at several hundred kV, giving wavelengths much smaller than that of light: 200kV electrons have a wavelength of 0.025Å. Unfortunately, whereas the resolution of the optical microscope is limited by the wavelength of light, that of the electron microscope is limited by aberrations inherent in electromagnetic lenses, to about 1~2 Å.

Because even for very thin samples one is looking through many atoms, one does not usually see individual atoms. Rather the high resolution imaging mode of the microscope images the crystal lattice of a material as an interference pattern between the transmitted and diffracted beams. This allows one to observe planar and line defects, grain boundaries, interfaces, *etc*. with atomic scale resolution. The bright-field/dark-field imaging modes of the microscope, which operate at intermediate magnification, combined with electron diffraction, are also invaluable for giving information about the morphology, crystal phases, and defects in a material. Finally the microscope is equipped with a special imaging lens allowing for the observation of micro-magnetic domain structures in a field-free environment.

The TEM is also capable of forming a focused electron probe, as small as 20Å, which can be positioned on very fine features in the sample for micro-diffraction information or analysis of x-rays for compositional information. The latter is the same signal as that used for SEM composition analysis, where the resolution is on the order of one micron due to beam spreading in the bulk sample. The spatial resolution for this compositional analysis in TEM is much higher, on the order of the probe size, because the sample is so thin. Conversely the signal is much smaller and therefore less quantitative. The high brightness field-emission gun improves the sensitivity and resolution of x-ray compositional analysis over that available with more traditional thermionic sources.

Sample preparation for TEM generally requires more time and experience than for most other characterization techniques. A TEM specimen must be approximately 1000Å or less in thickness in the area of interest. The entire specimen must fit into a 3mm diameter cup and be less than about 100 μm in thickness. A thin, disc shaped sample with a hole in the middle, the edges of the hole being thin enough for TEM viewing, is typical. The initial disk is usually formed by cutting and grinding from bulk or thin film/substrate material, and the final thinning done by ion milling. Other specimen preparation possibilities include direct deposition onto a TEM-thin substrate (Si_3N_4, carbon); direct dispersion of powders on such a substrate; grinding and polishing using special devices (t-tool, tripod); chemical etching and electro-polishing; lithographic patterning of walls and pillars for cross-section viewing; and focused ion beam (FIB) sectioning for site specific samples.

Artifacts are common in TEM samples, due both to the thinning process and to changing the form of the original material. For example surface oxide films may be introduced during ion milling and the strain state of a thin film may change if the substrate is removed. Most artifacts can either be minimized by appropriate preparation techniques or be systematically identified and separated from real information.

2.4.3 Scanning Transmission Electron Microscopy (STEM)

High-resolution STEM capabilities are needed in order to overcome the SEM resolution limits created by the interaction volume in bulk samples. Originally, STEM capabilities were achieved by using convergent-beam TEM in spot mode. In the traditional TEM mode, two condenser lenses are adjusted to illuminate the specimen with a nearly parallel beam of electrons. The transmitted electrons are then focused by the objective lens to form a real image. Convergent-beam TEM in spot mode uses a series of condenser lenses to demagnify the original gun crossover to a spot on the specimen [5]. Scan coils can then be used to move the spot across the specimen. A TEM with scanning capabilities is often referred to as a STEM in the literature.

In a dedicated STEM, the optical design is more closely related to a SEM than a TEM. A source of electrons is produced by an electron gun and accelerated to an energy of approximately 200~400keV. In a cold Field Emission STEM (FESTEM), the initial crossover is on the order of 5.0 nm. The vacuum is capable of reaching 1.0×10^{-8} Pascal in the electron gun and approximately 3.0×10^{-5} Pascal in the specimen chamber. The optics system focuses the electron beam to a final spot on the sample on the order of 0.5 nm with a beam current of approximately 1 nA [6]. While bulk specimens can be analyzed in a SEM, a thin sample on the order of hundreds of nanometers is used for STEM analysis. The high energy electron beam and thin sample decrease the size of the interaction volume and improve the resolution. As discussed in Section 2.4, several signals including SE, BSE, x-rays, photons, and EHPs are produced from the interaction volume that is created within the thin specimen and can be detected and used for imaging. In addition, the transmitted electrons can be detected with a high-angle annular dark field (HAADF) detector or a bright field (BF) detector. The HAADF detector is an annular detector placed concentrically about the post-specimen optical axis. The HAADF detector detects transmitted electrons that have been scattered through high angles. The acceptance angle of the HAADF detector is typically between 50mrad~200mrad, but can often be controlled with a projector lens. HAADF images are often called "Z-contrast" images because the cross section for Rutherford elastic scattering is proportional to Z2 [5, 6]. Therefore, high-Z regions of a specimen would scatter more electrons and have a higher intensity than low-Z regions [5, 6]. The BF detector is an axial detector that is usually placed after the HAADF detector and detects transmitted electrons that have undergone low angles of scatter.

2.4.4 X-Ray Energy-Dispersive Spectrometer (X-Ray EDS)

The x-ray energy dispersive spectrometer (XEDS) is the only X-ray spectrometer currently used in TEMs. It is remarkably compact, efficiency, and sensitive. The

XEDS produces spectra which are plots of X-ray counts (intensity) versus X-ray energy. When electrons ionize an atom, the emitted characterisitic X-ray energy is unique to the ionized atom. When electrons are slowed by interaction with the nucleus, they produce a continuum of bremsstrahlung X-rays. A combination of Si(Li) and Ge detectors can detect Kα lines from all the elements, from Be to U [5].

2.5 Optical and Electrical Characterization Methodology

2.5.1 Photoluminescence Spectroscopy (PL) and Cathodoluminescence Spectroscopy (CL)

When a solid is supplied with a certain type of energy it may emit photons, or undergo a process called luminescence. The luminescence process can be categorized according to the excitation source. Photoluminescence (PL) is due to photon excitation, chemiluminescence is due to energy supplied by a chemical reaction, thermoluminescence is due to energy supplied by heating, electroluminescence is due to excitation by application of an electric field, and cathodoluminescence (CL) is due to excitation by an electron source. The mechanisms leading to the emission of light in a solid are similar for the different types of excitation sources described above and can provide complimentary information [7, 8].

Photoluminescence (PL) depends on the nature of the optical excitation. The excitation energy selects the initial photoexcited state and governs the penetration depth of the incident light. The emission signal depends on the density of photoexcited electrons, and the intensity of the incident beam can be adjusted to control this parameter. When the type or quality of material under investigation varies spatially, the PL signal will change with excitation position. In addition, pulsed optical excitation provides a powerful means for studying transient phenomena. Short laser pulses produce virtually instantaneous excited populations, after which the PL signal can be monitored to determine recombination rates.

PL is simple, versatile, and nondestructive. The instrumentation that is required for ordinary PL work is modest: an optical source and a spectrophotometer. A typical PL set-up is shown in Figure 2-11. Because the measurement does not rely on electrical excitation or detection, sample preparation is minimal. This feature makes PL particularly attractive for material systems having poor conductivity or undeveloped contact technology. Measuring the continuous wave PL intensity and spectrum is quick and straightforward. Instrumentation for time-resolved detection, such as single photon counting, can be expensive and complex. Even so, PL is one of the only techniques available for studying fast transient behavior in materials.

The advantages of PL analysis derive from the simplicity of optical measurements and the power to probe fundamental electronic properties. The chief drawback of PL analysis also follows from the reliance on optical techniques: the sample under investigation must emit light. Indirect-bandgap semiconductors, where the conduction band minimum is separated from the valence band maximum in momentum space, have inherently low PL efficiency. Nonradiative recombination tends to dominate the relaxation of excited populations in these materials. This problem can be augmented by poor surface quality, where rapid nonradiative events may occur. Nevertheless, once a PL signal is detected, it can be used to characterize both radiative and nonradiative mechanisms.

The choice of excitation is critical in PL measurement. The excitation energy and intensity will have profound effects on the PL signal. Although the excitation conditions must be considered carefully, the strength of the PL technique relies heavily on the flexibility that these adjustable parameters provide. Because the absorption of most materials depends on energy, the penetration depth of the incident light will depend on the excitation wavelength. Hence, different excitation energies probe different regions of the sample. The excitation energy also selects the initial excited state in the experiment. Because lasers are monochromatic, intense, and readily focused, they are the instruments of choice for photoluminescence excitation. A relatively inexpensive He-Cd or diode laser will often satisfy the basic requirement of light exceeding the bandgap energy. In more demanding experiments, the laser is chosen carefully to probe a particular depth or to excite a particular species.

Cathodoluminescence (CL) is a SEM-based technique that can be used for the characterization of semiconductor materials and devices. A typical CL set-up is shown in Figure 2-12. SEM-based and CL can provide information on the concentration and distribution of luminescent centers, distribution and density of electrically active defects, and electrical properties including minority carrier diffusion lengths and lifetimes. CL is the emission of light as the result of electron or "cathode-ray" bombardment. The CL phenomenon was first reported in the middle of the 19th century during experiments on electrical discharges in evacuated glass tubes. Luminescence was observed when cathode rays struck the glass tubes [7, 8]. The observation of luminescence due to cathode ray bombardment eventually led the J.J. Thomson to the discovery of electron in 1897. Now, CL is widely used in cathode-ray tubebased instruments such as oscilloscopes, televisions, and electron microscope fluorescent screens.

The CL signal is generated by detecting photons, in the ultraviolet to infrared range, that are emitted as a result of electronic transitions between the conduction band and valence band, between levels due to impurities and defects in the fundamental gap, or between impurity and defect levels and the valence band. The transition energies and probabilities can be affected by external perturbations, such as stress and electric fields. CL analysis performed in an electron microscope can be divided into spectroscopy and microscopy.

In CL microscopy, luminescence images or maps of areas of interest are obtained by a scanning or parallel beam. In panchromatic CL imaging the combined intensity of all CL wavelengths within the response of the detector are used to create the image. In monochromatic CL imaging, the light is coupled into a monochromator and CL images can be created from a selected wavelength bandpass [7, 8].

In direct band gap semiconductor materials, the minimum of the conduction band and the maximum of the valence band occur at the same momentum value in an energy versus momentum plot. Momentum is conserved in direct band gap transitions and the transitions appear vertical on energy versus momentum plots. In these materials, the most likely radiative transitions are between the filled states of the conduction band minimum and the empty states of the valence band maximum. If the material is an indirect band-gap material, the maximum of the valence band and minimum of the conduction band do not occur at the same momentum value, and therefore phonon participation is required to conserve momentum. The recombination of electrons and holes results in the simultaneous emission of a photon and a phonon. Since the probability of this process is lower than direct transitions, intrinsic emission is relatively weak compared to extrinsic luminescence in an indirect band gap material. A simplified set of radiative transitions that lead to luminescence emission in semiconductors containing impurities is shown in Figure 2-13 and a description of each process follows.

Process 1 produces intrinsic luminescence due to direct recombination between an electron in the conduction band and a hole in the valence band and results in the emission of a photon with energy close to that of the band gap. The recombination may occur from states close to the corresponding band edges, but the thermal distribution of carriers typically leads to a Gaussian shaped spectrum with the peak corresponding to the transition with the maximum electron and hole concentration [7, 8].

Process 2 is excition decay that is typically observable at lower temperatures. An excition is a bound electron-hole pair and excitionic states exist just below the conduction band. In most III-V compounds, recombination emission of the excitonic state produces photons of energies approximately equal to the band gap of the semiconductor; therefore this process can also be considered an intrinsic process. The intrinsic luminescence band is often referred to as the near-band-gap band because excitons and shallow recombination centers may contribute to the emission at room temperature [7, 8].

Process 3, 4, and 5 correspond to transitions that start or finish on localized states of impurities within the band gap, such as donors or acceptors. These transitions produce extrinsic luminescence. Transitions between deep donor and deep acceptor levels can lead to emission with photon energies significantly below the band gap. Shallow donor or acceptor levels can be very close to the conduction band and valence bands. For example, silicon is a shallow donor in gallium nitride located approximately 20 meV below the conduction band [9]. Transitions that occur between a shallow donor and acceptor states or between donor and acceptor states and the conduction band or valence bands may be difficult to distinguish from intrinsic luminescence. In these cases, CL measurements can be performed at cryogenic temperatures using liquid nitrogen or liquid helium as a cryogen. CL spectra can be sharpened into lines and series of lines corresponding to transitions between well-defined energy levels due to a reduction in the thermal excitation of carriers. There is also an increase in the CL intensity as the temperature is lowered because radiative recombination becomes more favored as compared to the competing non-radiative recombination. An additional advantage of performing CL at cryogenic temperatures is the reduction of electron bombardment damage [7, 8].

2.5.2 Time-Resolved Photoluminescence (TRPL)

Figure 2-144 shows the experimental setup of the TRPL (the same as temperature dependent PL setup). Pulsed photo-excitation for the TRPL was provided by the frequency doubled (2ω) or frequency tripled (3ω) beams of a mode-locked Ti : Sapphire laser (Coherent MIRA900) pumped by Verdi V8 (532 nm Nd:YVO_4 diode-pumped solid-state laser CW output) was used as pumping source. The wavelength of Ti: Sapphire laser can be tuned from 668 nm to 938 nm, the pulse width is 200 fs. The repetition rate of the laser is 76 MHz. To direct examine the optical properties of InGaN/GaN MQW LEDs and avoid the absorption of GaN film, the pumping light source was a frequency doubled Ti: Sapphire laser operated on 400 nm with 10 mW. The luminescence signal dispersed through a 0.55-meter monochromator (HORIBA ® Jobin Yvon Triax 550) was detected by the photomultiplier tube (PMT). The luminescence decay was measured with time correlated single photon counting (TCSPC) system in conjunction with monochromator using gratings whose grooves are 2400 grooves/mm. Time-resolution for the detection is about 4 ps. For temperature dependent experiment, the samples were mounted in a closed-cycle He cryostate, pump was used to draw out air in cryostate to obtain high vacuum (~10^{-3} torr), and temperature from 15 K to room temperature (300 K).

2.5.3 Temperature Dependent Photoluminescence (TDPL)

If there are some defect energy level existed in energy band gap of semiconductor, they also could contribute to radiative recombination process. Therefore we could observe the multiple emission peaks in the PL spectra, and the intensity of the emission peaks is related to the contribution of the individual radiative recombination process. In general, there are four possible radiative recombination transitions in semiconductor (shown in Figure 2-13). By analyzing the spectra of material, we can direct inspect the purity of material. On the other hand, temperature dependent PL is a useful method to extract the thermal activation energy of optical transition. The temperature dependent PL intensity is general expressed as:

$$I(T) = \frac{I(0)}{1 + A\,e^{\frac{-E_a}{kT}} + B\,e^{\frac{-E_b}{kT}}} \tag{2.3}$$

where A, B is the coefficient related to defect density, and Ea, Eb is the activation energy, k is Boltzmann constant, I(T) is the intensity of light emission at temperature T, and the I(0) in our experiment is about 15 K due to the nonradiative recombination is suppressed. The activation energy is the physical value that means the transition energy barrier from radiative recombination to nonradiative recombination, which can represent the exciton binding energy, localized energy, band offset of QW, energy difference between defect energy level to conduction band or valence band and …etc.

By plotting the Arrhenius plot for PL intensity, we can extract the activation energy to analyze the origin of radiative recombination. Moreover, temperature dependent emission energy shift (also call S-Curve) is also used to analyze the exciton localization effect in InGaN MQWs.

2.5.4 Electroluminescence (EL) Spectroscopy

When a solid is luminescence in response to the running electrical current through the materials, it's called electroluminescence (EL). The output of EL is relied on a number of factors such as the optical properties and physical structures of the active region, the selection of the doping agent, the level of doping concentration, the electrical properties of two conductive regions which are used for cathode and anode contacts, and the properties of the electrical contacts through which the electrical current injected.

The equipment of electroluminescence spectrum is shown in Figure 2-155, which include probe station, current source, and power-meter module. Keithley 2601A can provide precisely continuous current with laser diode and measure relative voltage in parallel. An integration sphere was used to collect emitting power from our samples and to improve the accuracy of power measurement. The samples were placed on a platform of the probe station and injected bias current with microprobe. Threshold condition, slope efficiency, turn-on voltage and differential resistance can be obtained from L-I-V information by adjusting bias current. Emission spectrum of the device was measured by optical spectrum analyzer. A multi-mode fiber probe was placed close to the emission aperture to take optical spectra [9].

2.6 References

[1] C. Sartel, *et al.*, "Low temperature homoepitaxy of GaN by LP-MOVPE using Dimethylhydrazine and nitrogen," *Superlattices and Microstructures*, vol. **40**, pp. 476-482, 2006.

[2] H. Sato, *et al.*, "Preparation of GaN films on sapphire by metalorganic chemical vapor deposition using dimethylhydrazine as nitrogen source," *Applied Physics Letters*, vol. **68**, p. 3617, 1996.

[3] R. Lee and G. Stringfellow, "Pyrolysis of 1, 1 dimethylhydrazine for OMVPE growth," *Journal of electronic materials*, vol. **28**, pp. 963-969, 1999.

[4] J. Goldstein, *Scanning electron microscopy and X-ray microanalysis* vol. **1**: Springer Us, 2003.

[5] D. B. Williams and C. B. Carter, "The Transmission Electron Microscope," *Transmission Electron Microscopy*, pp. 3-22, 2009.

[6] P. Nellist, "Introduction to Scanning Transmission Electron Microscopy," *Journal of Microscopy*, vol. **191**, pp. 109-110, 1998.

[7] B. Yacobi and D. B. Holt, *Cathodoluminescence microscopy of inorganic solids*: Springer Us, 1990.

[8] C. R. Brundle, *et al.*, *Encyclopedia of Materials Characterization: surfaces, interfaces, thin films*: Gulf Professional Publishing, 1992.

[9] H. Morkoc, *et al.*, *Handbook of Nitride Semiconductors and Devices, Materials Properties, Physics and Growth*: Wiley-VCH, 2009.

Table 2-1. Three types of NIL Eitre® functions.

	Eitre® 3	*Eitre® 6*	*Eitre® 8*
Imprint Area	Up to 3"	Up to 6"	Up to 8"
Clean-room Compatibility	Class 100	Class 100	Class 100
Computer Controlled User Interface	Standard	Standard	Standard
Thermal Imprint	Standard	Standard	Standard
UV Imprint	Option	Option	Option
STU®	Option	Option	Option
IPS®	Option	Option	Option
Water Cooling	N/A	Option	Standard
Optical Alignment	N/A	Option	Option
Substrate-Stamp separation unit	N/A	Option	Option

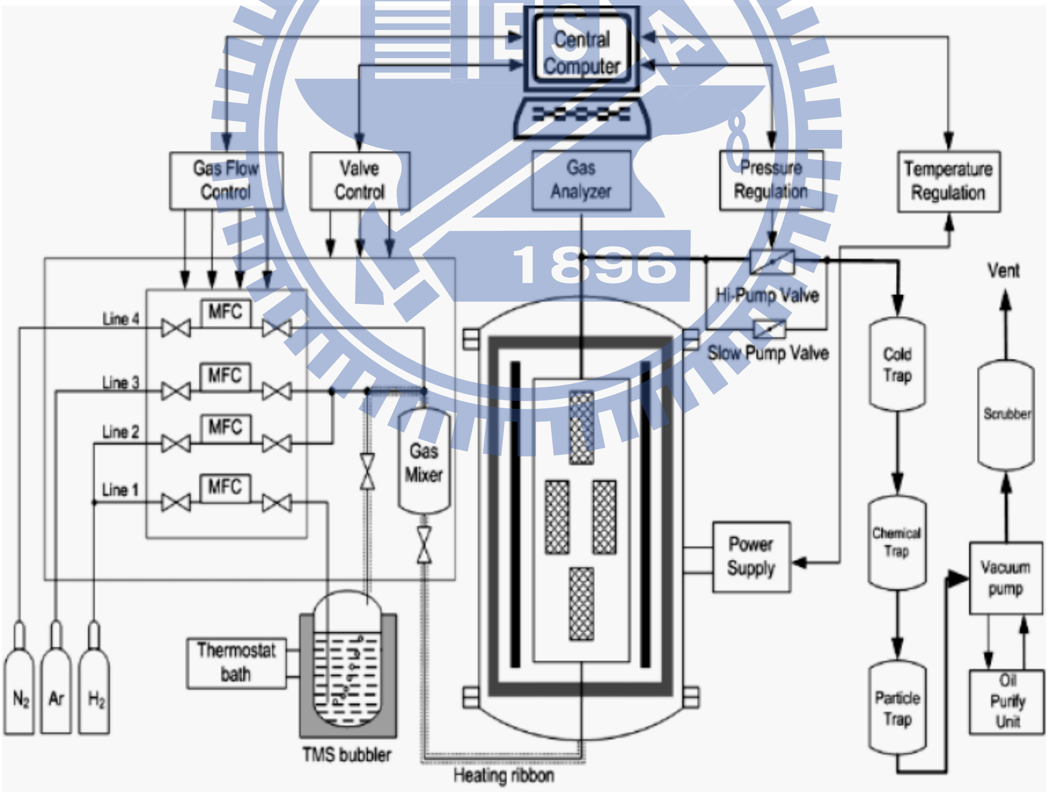

Figure 2-1. Description of subsystems in a MOCVD apparatus.

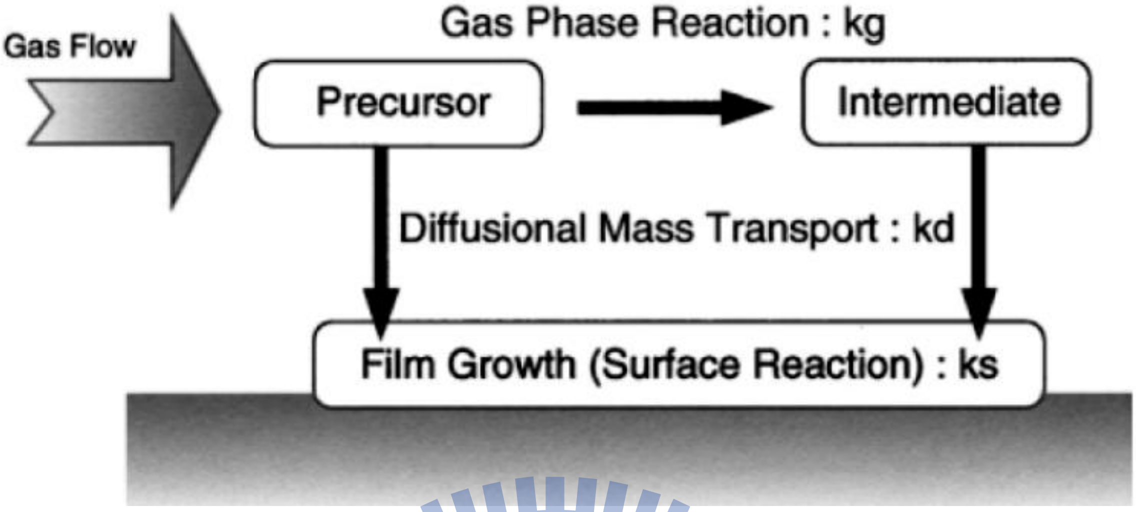

Figure 2-2. Illustration of the precursors impinging on the wafer surface and the restproducts.

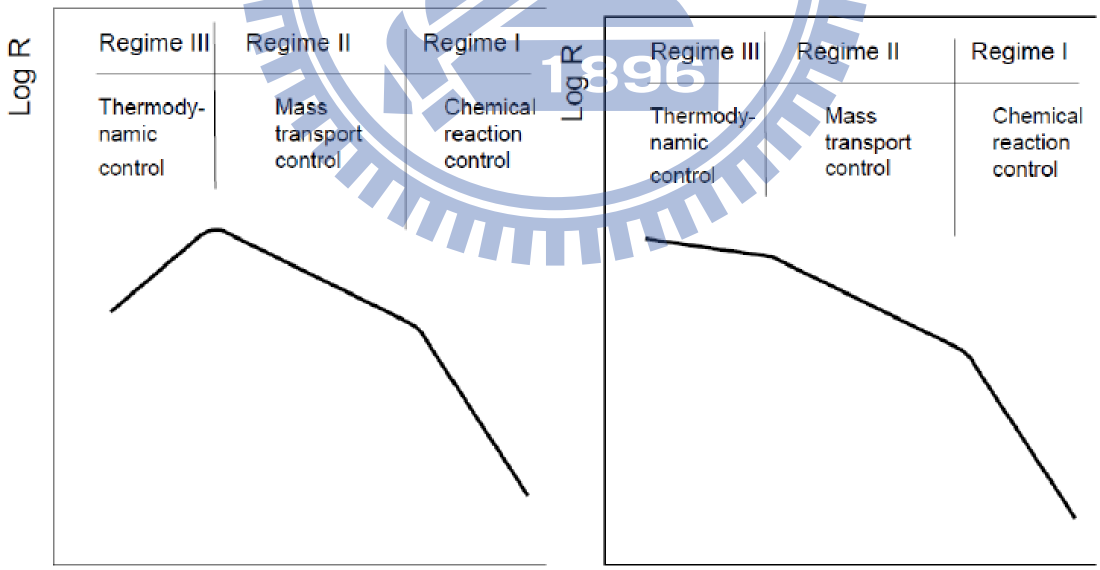

(a) (b)

Figure 2-3. Temperature dependence of the deposition rate: (a) exothermic reaction and (b) endothermic reaction

Figure 2-4. NIL Eitre® 6 on National Nano Device Laboratories.

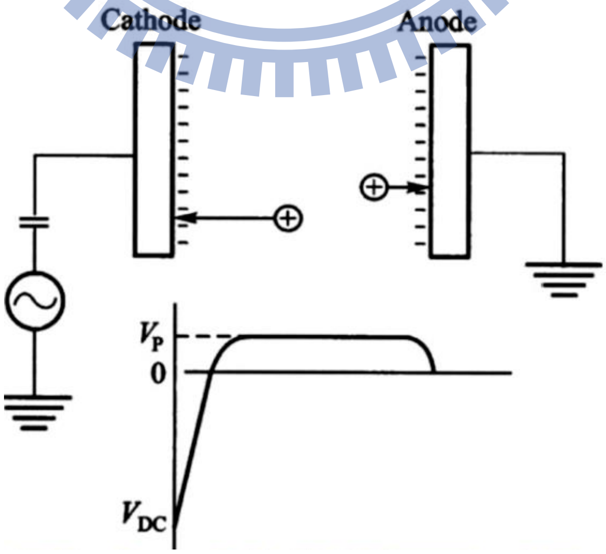

Figure 2-5. Fundamental physical operating mechanism of HDP-RIE.

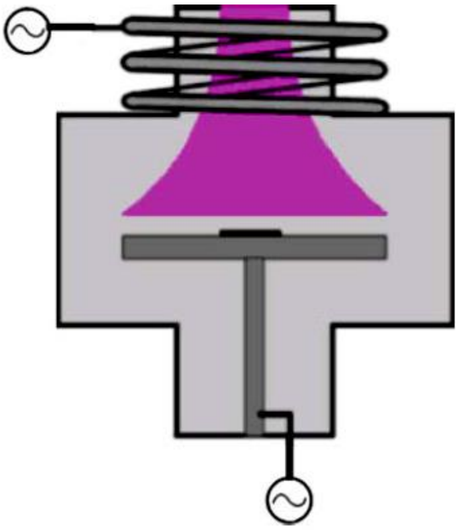

Figure 2-6. Schematic of inductive coupling plasma source.

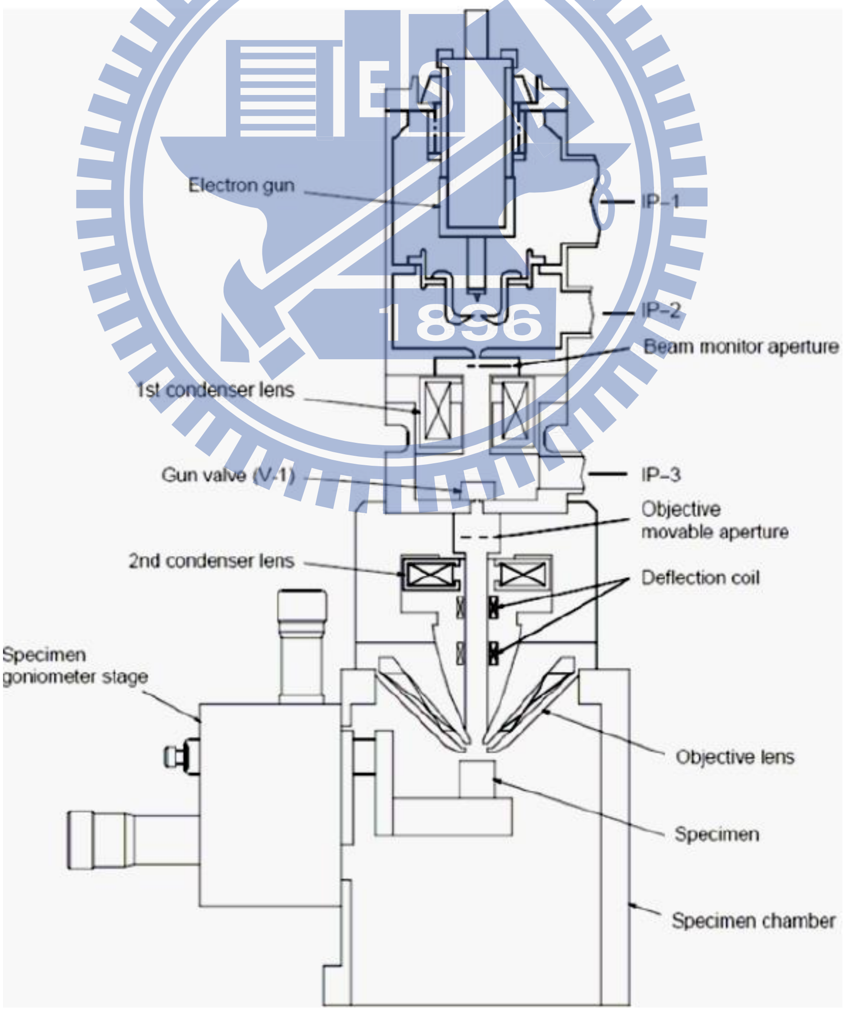

Figure 2-7. Schematic of SEM instrument.

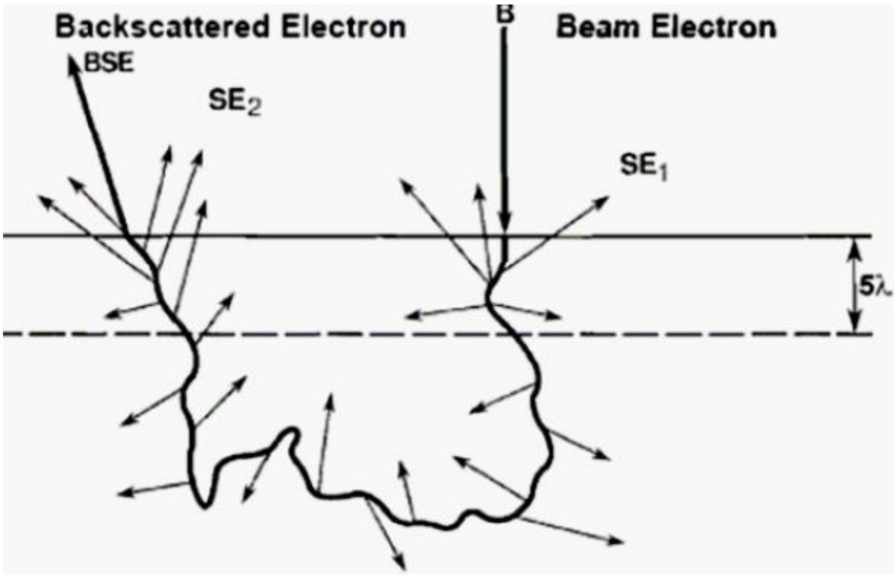

Figure 2-8. Schematic illustration of the origin of two sources of secondary electron generation in the sample.

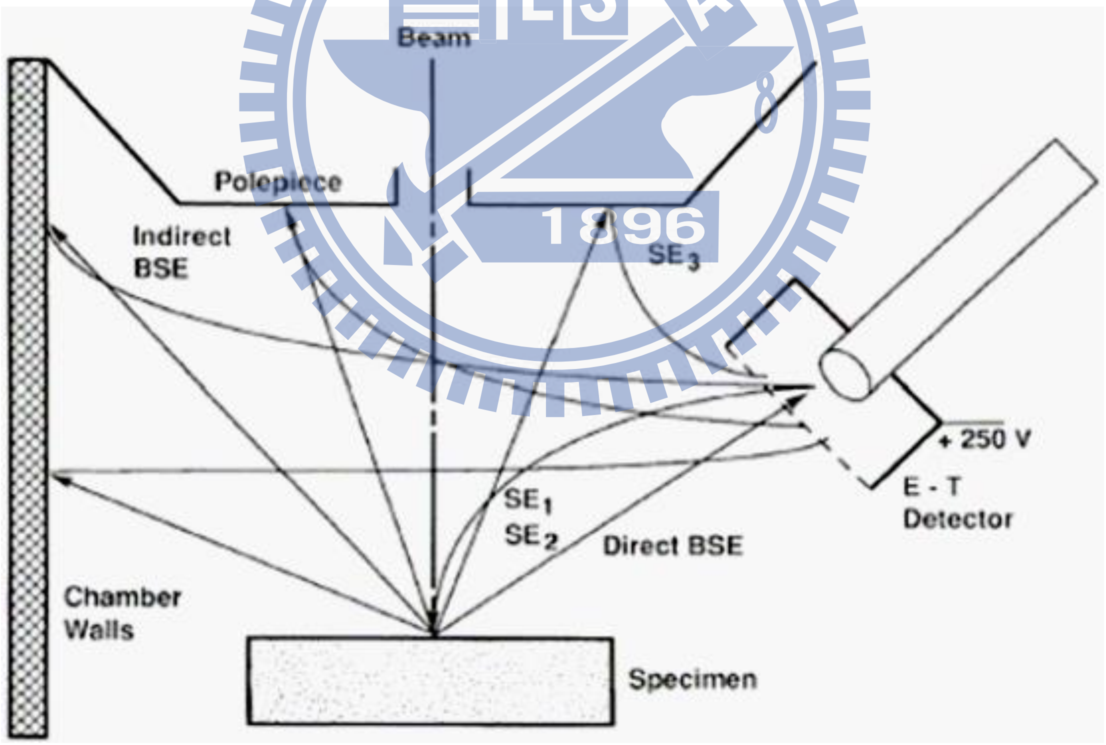

Figure 2-9. Schematic illustration of the indirect collection of backscattered electrons by a positively biased E-T detector.

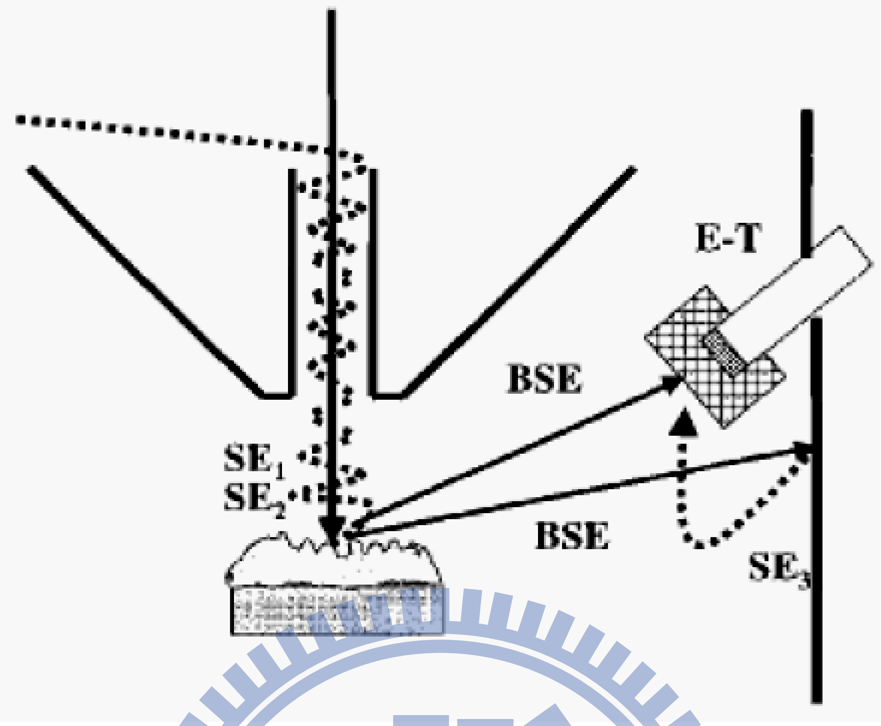

Figure 2-10. Through-the-lens (TTL) detector for SE used in high-performance field emission SEMs.

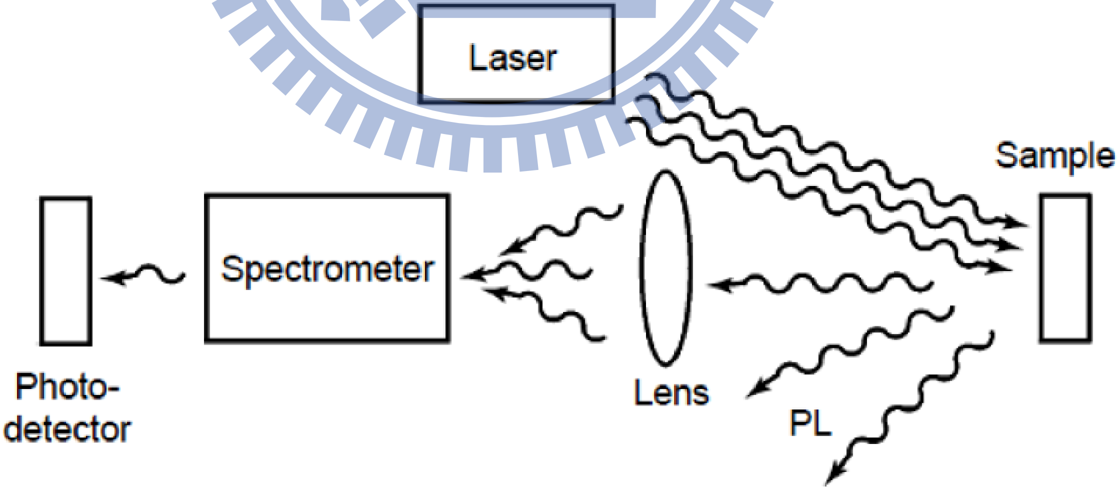

Figure 2-11. Typical experimental set-up for PL measurements.

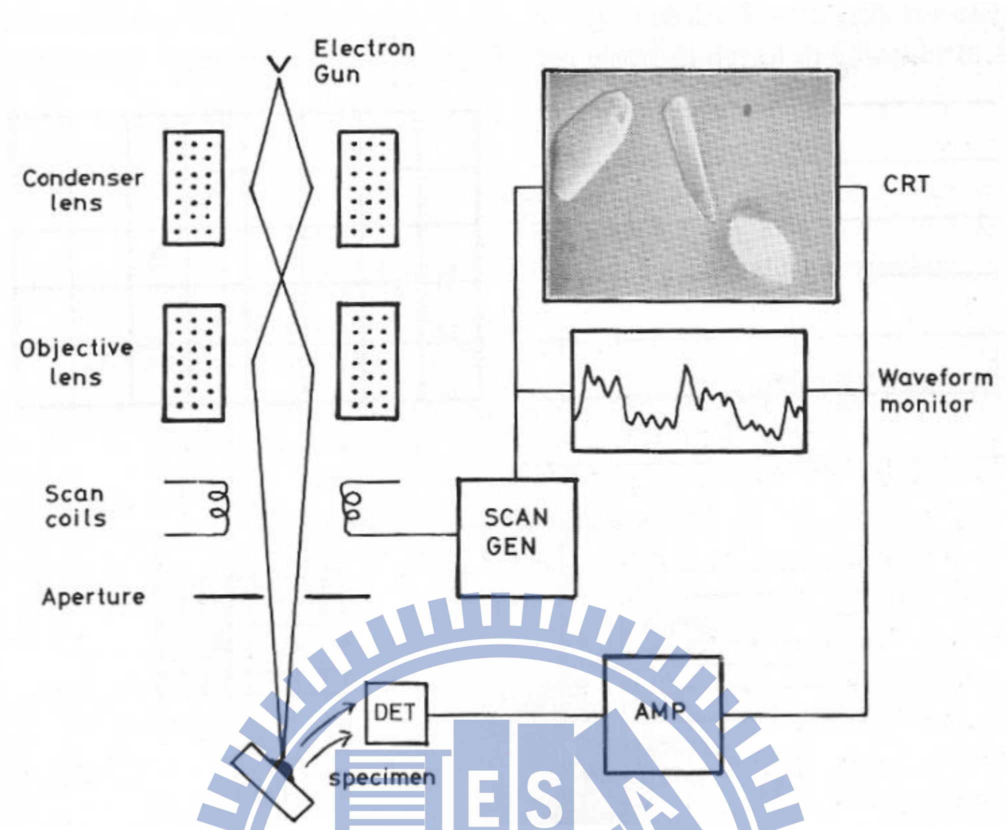

Figure 2-12. Schematic diagram of CL.

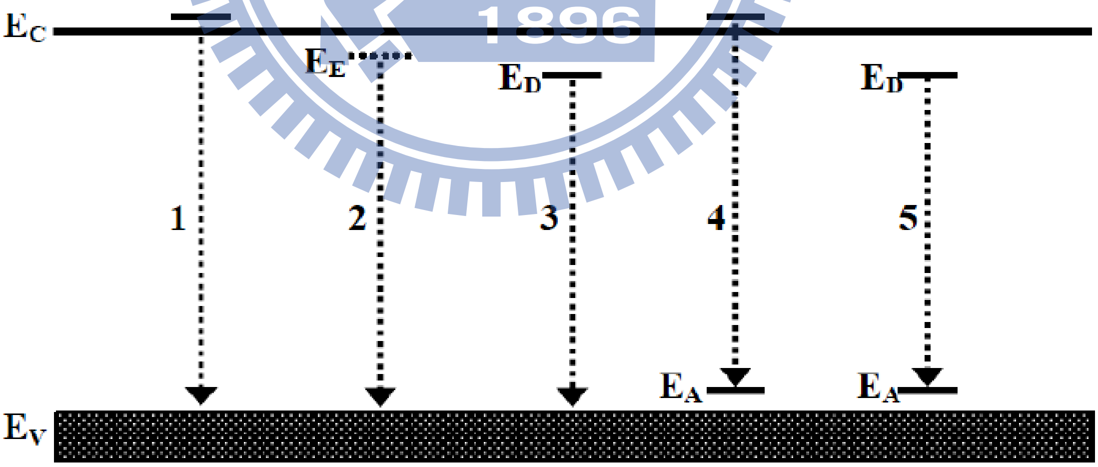

Figure 2-13. Schematic of the luminescence transitions between the conduction band (E_C), valence band (E_V), excition (E_E), donor (E_D), and acceptor (E_A) levels in a luminescent material.

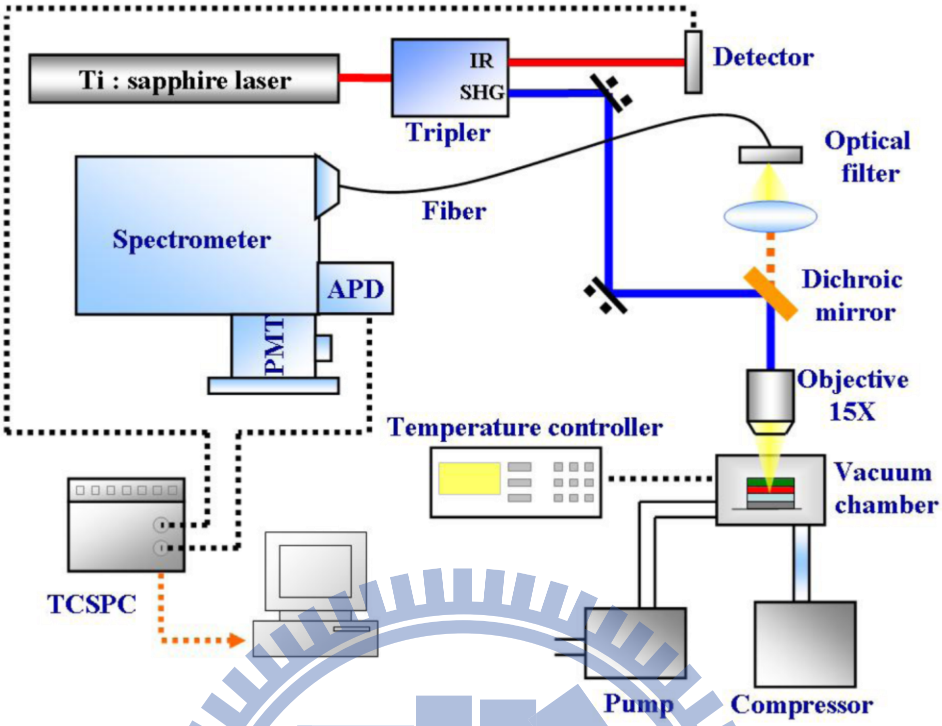

Figure 2-14. The schematic setup of TRPL system.

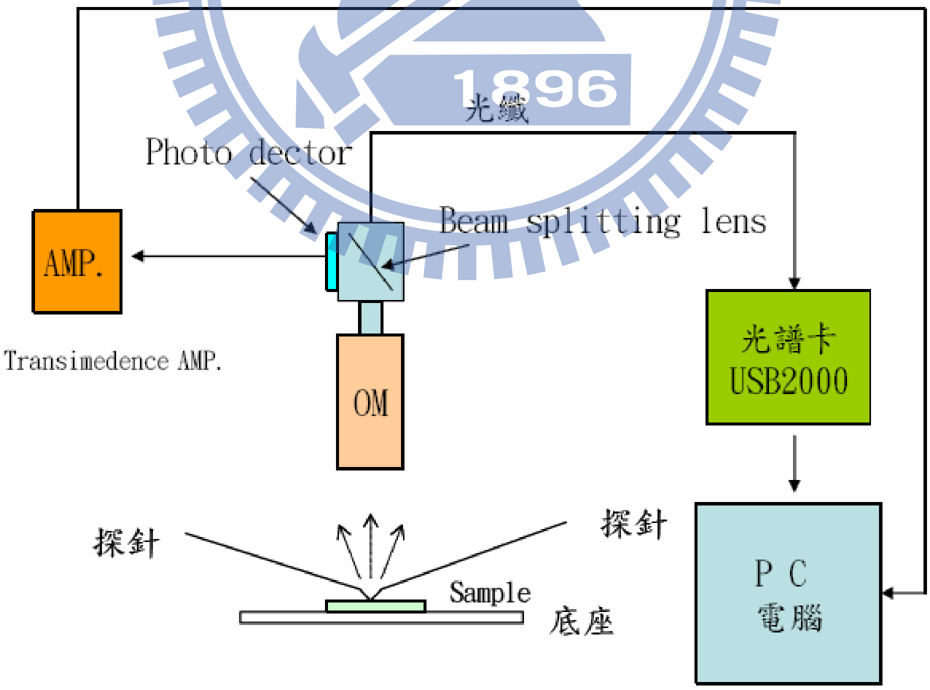

Figure 2-15. EL system includes all components.

Chapter 3

Fabrication of 3-D Core-shell InGaN/GaN Multi-Facet Qunatum Wells Optoelectronic Devices on Semipolar $\{10\bar{1}1\}$ and Nonpolar $\{10\bar{1}0\}$ Plane

The III-nitride based LED has gained great research interests due to its promising potential in high efficient lighting applications. The band gap of InGaN semiconductor can be potentially varied from UV (3.4 eV) to near infrared (0.7 eV) [1]. In principle, such devices can cover the entire visible spectrum, thereby promising multiple color lighting applications without the use of down-converting phosphors which have significant Stokes shift energy loss. Conventional InGaN/GaN MQWs in a GaN based LED are often grown on c-plane GaN surface. The emission wavelength is typically in the blue region, where the efficiency is optimal. To have emission wavelength in the green to red region, higher In incorporation in the InGaN MQWs is required. However, the efficiency drops rapidly as In concentration increases.[2, 3] One of the primary causes is the large strain induced piezoelectric field due to the lattice mismatch among the sapphire growth template, GaN, and InGaN. The piezoelectric field results in significant spatial separation of electron and hole wave function in MQWs and leads to low quantum efficiency [4, 5]. One possible way to reduce this detrimental effect is to use different crystal planes with lower polarization field. Experimental demonstrations have been reported for MQWs grown on semipolar and nonpolar substrates, showing promising potential in improving emission efficiency [6-8]. These substrates are, however, not readily available.

The semipolar and nonpolar crystal surfaces can be found in naturally formed crystalline structure by 3-D epitaxial growth. Nano size hexagonal pyramids can be grown by selective area growth on the opening holes of a SiO2 masked c-plane GaN substrate, which is more readily available [9]. The pyramid facets are typically $\{10\bar{1}1\}$ or $\{11\bar{2}2\}$ semipolar planes. In addition to the intrinsic low polarization field of these crystal planes, the small footprint of 3D nano structure on the substrate can also provide better strain relaxation, resulting in lower defect density and the further reduction of the piezoelectric field. Previous Photoluminescent (PL) studies of MQWs grown on these nano-scale facets have demonstrated significant reduction in the polarization field and the increase of internal quantum efficiency [10,11]. There have been strong interests in using these semipolar pyramid facets for LED applications, in particular high In content LEDs [12, 13]. The experiments were however mostly carried out by photo excitation. Reports on electrical performance are very limited [13,14]. A thick layer of p-GaN was grown on top of the nanopyramids to planarize the surface for electrical contacts, which could compromise the electrical performance due to its high resistivity [13,14]. Even though the nanopyramid structure shows promising advantages in optical emission properties, the 3D nano geometry often poses challenges for making electrical injection, which is an important issue for practical device realization. In this chapter, the fabrication flow charts of Fabrication of 3-D Core-shell InGaN/GaN Optoelectronics Devices were introduced, the selective area growth (SAG) was used in our experiment, we used the Silicon dioxide (SiO_2), which was deposited by plasma-enhance vapor deposition (PECVD) to prevent GaN from growing on the side walls in the epitaxial regrowth. The spatially morphology, defect reduction and the enlarged area of Core-Shell MQWs in photonic quasi-crystal arrays were explained by schematic figures, SEM, and TEM analyses..

3.1 Procedures of 3-D Core-shell InGaN/GaN Multi-Facet Qunatum Wells Structure on Semipolar $\{10\bar{1}1\}$ and Nonpolar $\{10\bar{1}0\}$ Plane

Currently, sapphire was usually used as substrate to grow high quality GaN by heteroepitaxy. The sapphire substrate has many advantages include low cost, transparent nature, thermal stability and a mature technology for nitride growth. In this section, we have demonstrated the 3-D Core-shell InGaN/GaN MQWs structure on GaN nanorod. A core-shell nanorod includes a shell of InGaN/GaN multi-quantum wells (MQWs) and a core of GaN nanorod.

3.1.1 Growth Procedure of Nanorods on C-plane (0001) GaN Epilayer Template by Nano-Imprint Lithography

Figure 3-1 shows he flow chart for the fabrication of GaN nanorods. First, the epitaxial growth of a (0001) *c*-plane GaN layer on (0001) *c*-plane sapphire substrate was performed by AXITRON 2600HT Metal Organic Chemical Vapor Deposition (MOCVD) reactor. The epitaxial relationship between GaN and sapphire is $(0001)_{GaN} \parallel (0001)_{Sapphire}$. The metallorganic compounds of trimethylgallium (TMGa) and ammonia (NH_3) were used as the precursors for Ga and N, respectively. Prior to growth, the sapphire substrates were thermal annealed in hydrogen ambient, then a 2 μm u-GaN template and a 3 μm n-GaN had grown by MOCVD on a *c*-plane sapphire substrate, respectively. The fabrication procedures of GaN nanorods are as follows: First, the e-beam evaporation of nickel (Ni) thin layer was covered over the GaN template. A 0.5μm SiO_2 thin film was deposited by plasma-enhanced chemical-vapor deposition (PECVD), followed by a 0.2 μm spin-coated photoresist layer over the

SiO_2 mask. The sample was then embossed by using the Si master which was fabricated by traditional photolithography and anisotropic wet etching on Si template. Figure 3-2 shows the flow chart of IPS-STU® technology of nano-imprint lithography, including Intermediate Polymer Stamp (IPS®) and Simultaneous Thermal and UV (STU®). The imprint pattern was created by Soft Press® and was identical copy for the master pattern. Then the patterned photoresist was thermally annealed for silicon on glass hardening.

The pattern photoresist was transferred to SiO_2 hard-mask by reactive ion etching (RIE) with CHF_3/O_2 mixture. The SiO_2 and Ni disks were used as hard masks in inductively coupled plasma reactive ion etching (ICP-RIE) to etch down exposed GaN and form GaN nanorods. The hard masks were removed by wet etching process in the end. Finally, the average height, diameter and pitch size of GaN nanorods were 1μm, 350nm and 750nm, respectively. The geometry of nanorods arranged in a 12-fold pattern will be discussed in next section.

3.1.2 Regrowth of Core-Shell InGaN/GaN MQWs on GaN Nanorods on Semipolar $\{10\bar{1}1\}$ and Nonpolar $\{10\bar{1}0\}$ Plane

After previous GaN nanorod formation, the nanorods samples were reloaded into MOCVD reactor. The regrowth process formed the crystalline facets on the etched nanorod surfaces. Six pairs of InGaN/GaN multiple quantum wells (MQWs) also grew on the nanorod crystalline facets. The metallorganic compounds of trimethylgallium (TMGa), trimethylindium (TMIn) and ammonia (NH_3) were used as the precursors for Ga, In and N, respectively, with H_2 and N_2 as the carrier gas. The reactor pressure was kept 300 Torr in all regrowth process. The schematic illustration of the regrowth process is shown in Figure 3-3, the thin n-GaN, pre-srain and the core-shell InGaN/GaN MQWs layers were conformably grew on GaN nanorods. The growth time was 250 sec for wells and 500 sec for barriers. The regrowth temperature of MQWs was 700℃/805℃ for sample HT and 645℃/805℃ for sample LT. The morphology of core-shell nanorods will be discussed as following.

The nanorod arrays were fabricated from a GaN epitaxial template by nano-imprint patterned etching (Figure 3-4 (a)), an average height of GaN nanorods was about 1 μm, followed by epitaxial regrowth to form crystalline facets. Figure 3-4 (b) and (c) showed that the regrowth InGaN/GaN MQWs on GaN nanorods of sample HT and sample LT, respectively. The schematic illustration of growing core-shell InGaN/GaN MQWs on GaN nanorods was shown in Figure 3-4 (d).

The imprint patterned etching created nanorod arrays in a 12-fold symmetric PQC pattern as depicted in Figure 3-4. Such a pattern does not have translational symmetry but has long range order and 12-fold rotational symmetry. The usage of PQC arrays of nanorods arranged in a two-dimensional 12-fold pattern can change the light propagation direction [15]; as a result, the enhancement of light extraction can be expected.

Conventional *c*-plane GaN hetroepitaxial layers grown on sapphire substrates by MOCVD result in a noticeable high threading dislocation (TD) density on the order of mid 10^{-8}~10^{-9} cm^{-2}, caused by a large lattice mismatch (~14%) and the thermal coefficient difference between GaN and sapphire. The formation of defects including TDs may deteriorate InGaN/GaN MQWs and act as nonradiative recombination centers which can damage the performance of devices [16]. Therefore, reducing the number of TDs is essential for fabricating high efficiency devices. There are about five dislocations per square micrometer of *c*-plane GaN template with a typical TDs density. For top-down etching via the NIL process to translate 12-fold PQC pattern and eliminate dislocations on the template. The process of defect reduction is shown in Figure 3-5 (a). To evaluate the number of TDs which were eliminated by NIL technology, a calculation was performed by the filling factor as given in:

$$\text{Filling factor} = \frac{\text{12 rods}}{\text{12 } \times \text{equilateral triangle} + 6 \times \text{square}} = 0.24 \tag{3.1}$$

The aforementioned PQC pattern is a 2-D pattern filled with squares and equilateral triangles whose edges have same length (superlattice constant a =750 nm), as shown in Figure 3-5 (b) [17]. There are 12 equilateral triangles and 6 squares in a single 12-fold pattern, and the 12 nanorods are placed at vortices, as drawn in Figure 3-5 (c). Figure 3-5 (d) reveals a top-view SEM micrograph of GaN nanorods with radius about 175 nm and the pitch size about 750 nm. Relative to the underlying *c*-plane GaN layer, about one order of magnitude reduction in the number of TDs can be surmised from filling factor as depicted in Figure 3-6 (a). Further, the red circle indicates a TD which is buried in the underlying template as shown in the cross-sectional STEM image of Figure 3-6 (b). However, the relatively large diameter of GaN nanorods with 350 nm results in few GaN nanorods with TDs proceeding from the *c*-plane GaN template. After regrowth, TDs were bended to the side-wall surface then passing through the shell of MQWs in Figure 3-7.

Then, the core-shell nanorod samples were carried out in MOCVD reactor by varying regrowth temperature of MQWs. Under a regrowth temperature of MQWs at 700 ℃, core-shell nanorods reflect smooth side and top facets with the GaN [0001] direction along the growth direction, as shown in Figure 3-8 (a)-(d). On the contrary, sample LT with the rough sidewall reveals a degraded surfaces of a reduced regrowth temperature at 645℃, as shown in Figure 3-8 (e)-(g). This phenomenon is mainly due to the lower species mobility with the lower temperature, resulting in undefined facet selective growth of the border portion between $\{10\bar{1}1\}$ facets and $\{10\bar{1}0\}$ facets [18].

From the top-view SEM image (Figure 3-8 (a) and (c)), sample HT, half the number of nanorods with perfect pyramid $\{10\bar{1}1\}$ facets on the top of core-shell nanorods. However, there are half the number of nanorods have $\{10\bar{1}n\}$ facets appearing on the pyramid top, as shown in Figure 3-8 (d), the further investigation of crystalline facet will be discussed in the following section. Sample LT has the similar morphology of all core-shell nanorods where $\{10\bar{1}n\}$ facets appears on the pyramid $\{10\bar{1}1\}$ facets, as shown in Figure 3-8 (g). As shown in Figure 3-8 (b) and (f), the epitaxial regrowth of InGaN/GaN MQWs on GaN nanorods formed $\{10\bar{1}0\}$ *m*-plane facets on the sidewalls and $\{10\bar{1}1\}$ hexagonal pyramid on the top of core-shell nanorods. An average height of nanorods after regrowth of sample HT about and sample LT are about 1.73 μm and 1.80μm, respectively. Each arrow-shaped nanorod is composed of a shell of InGaN/GaN MQWs on a core of GaN nanorods. In addition, we calculated the effective emitting area of core-shell MQWs conformally grown on semipolar and nonpolar facets of nanorods and MQWs grown on conventional *c*-plane by:

$$\text{Increasing of active area} = \frac{(s\text{-plane} + m\text{-plane}) \times 6 \text{ facets} \times 12 \text{ rods}}{12 \times \text{equilateral triangles} + 6 \times \text{squares}} \tag{3.2}$$

After regrowth, each arrow-shaped core-shell nanorods have six *m*-planes and *s*-planes. Given in the parameters of Figure 3-5 (c), Figure 3-8 (a) and (e), the enlarged active area of core-shell nanorods is compared to planar *c*-plane by a factor of 5.

In short, the core-shell InGaN/GaN MQWs grown on GaN nanorods with a reduced growth temperature from 700℃ to 645℃ were indicated to sample HT and sample LT, respectively. The surface morphology and the emission energies of core-shell nanorods were observed by scanning electron microscopy (SEM) and SEM-based cathodoluminscence (CL), separately. The crystalline quality and growth rate of MQWs were characterized by transmission electron microscopy (TEM) whereas indium content distribution was by TEM-based energy-dispersive spectrometer (EDS). The photoluminescence (PL) spectra were studied on the optical properties of core-shell nanorods. Those experimental results will be shown in the following chapter 4 and 5.

3.2 Procedures of 3-D Core-shell InGaN/GaN Multi-Facet Qunatum Wells LED Devices on Semipolar $\{10\bar{1}1\}$ and Nonpolar $\{10\bar{1}0\}$ Plane

In this section, we used the side wall passivation by PECVD to inhibit the epitaxial regrowth on the sidewall and under-layer region in the MOCVD regrowth process. Rather than SOG process, the PECVD process was a great benefit to being uniform and crack-free. As following, n-type GaN layer was grown by MOCVD using two step growth conditions.

3.2.1 Fabrication of Nanorods and SiO_2 Sidewall Passivation

Figure 3-9 (a)-(k) are the detailed process flow for fabricating the nanorod and the sidewall passivation process. The InGaN-based LED wafer was grown on a 2-in c-sapphire substrate through a metal organic chemical vapor deposition (MOCVD) system. First, 2-µm un-doped GaN and 3-µm n-type (Si doped) GaN was deposited by MOCVD; Second, 300 nm SiO_2 thin film was deposited by PECVD as etching hard mask; Third, PMMA mask was spin on using spin-coater; Fourth, the nanodisk with diameter of 350 nm and spacing about 400 nm was formed by NIL technology; Fifth, hard mask was transferred by RIE using CF_4 and Ar mixing gas; Sixth, GaN nanorod was formed by ICP using Cl_2 and BCl_3 mixing gas with high power radio frequency; The GaN nanorod was formed, the side-wall passivation process was used the following step; Seventh, passivation layer (SiO_2) deposited on GaN nanorod uniformity by using PECVD; Eighth, PMMA sacrificing Layer by spin coater was spin on; Ninth, O_2 plasma was used to etch the tip PMMA; Tenth, the top SiO_2 was removed by RIE using CHF_3 and Ar mixing gas, and the PMMA would protect the bottom of SiO_2; At least, we used the O_2 plasma to remove the PMMA for MOCVD regrowth.

Figure 3-10 (a) and (b) shows the spin-on-glass (SOG) coating and PECVD SiO_2 passivation were to prevent GaN from growing on the side walls in the epitaxial regrowth. The process of SOG coating was our previous work. Obviously, it revealed that the surrounded SiO_2 is not good enough. More detail information about SOG process can be seen in Figure 3-10 (a), it was found that sidewall passivation is non-uniform and easy to crack after annealing. On the contrary, the process of PECVD SiO_2 is a good step. It would show the potential of simple fabrication process with better step coverage. It is easy to control in comparison with the previous SOG process. Figure 3-11 (a) is the fitting curve of the etching rate of PMMA in O_2 plasma, the slope is about -5.77 nm/sec through the linear fit, Figure 3-11 (b) is cross section view of the nanorod template after PMMA coating, it is quite smooth and the thickness of the film about 1520 nm, and Figure 3-11 (c) and (d) are bird's-eye view and cross section view, which are about 920 nm after 100 seconds O_2 plasma etching, the etching surface is very smooth and uniform; Figure 3-11 (e) and (f) are bird's-eye view and cross section view, which are about 370 nm after 200 seconds etching. The characteristic of regrowth on GaN NR was discussed on the next section.

3.2.2 Device Fabrication of Core-Shell InGaN/GaN MQWs LED Devices on Semipolar $\{10\bar{1}1\}$ and nonpolar $\{10\bar{1}0\}$ Plane

The fabrication steps are shown in Figure 3-12. The GaN nanopillars were first fabricated by patterned top-down etching of an n-doped GaN substrate. The sidewall passivation coating was to prevent GaN from growing on the side walls in the epitaxial regrowth. The nanopillar side walls were coated as described in chapter 3.2.1, followed by a MOCVD epitaxial regrowth to grow Core-shell InGaN/GaN MQWs on the tops of nanopillars. p-GaN conformal to the pyramid facets was subsequently grown to form arrays of Core-shell LEDs. Different In flow rates and growth parameters were adjusted to grow two different emission conditions. The core-shell InGaN/GaN MQWs grown on GaN nanorods with growth temperature (Tg) of 830℃ and 860℃ were labeled as Core-shell HT-LED and LT-LED. A standard LED fabrication process was used to fabricate LED chips, where indium tin oxide (ITO) was used as a transparent conducting layer (not shown here).

3.3 Summary

The semipolar and nonpolar crystal surfaces can be found in naturally formed crystalline structure by 3-dimensional epitaxial growth. Nano-size hexagonal pyramids and sidewall were grown by selective area growth on the opening of a SiO_2-surrounded-mask GaN nanorod on c-plane sapphire substrate, which is more readily available. The facets of pyramid were recognized as {10-11} or {10-12} semipolar planes. On the other hand, the facets of sidewall were recognized as {1-100} nonpolar planes. Here, we report the fabrication of core-shell LEDs. High In content MQWs were investigated. A thin p-GaN layer conformal to the core-shell geometry was grown on the nanopyramid facets. In chapter 4, the surface morphology and the emission energies of core-shell nanorods were observed by scanning electron microscopy (SEM). The crystalline quality and growth rate of MQWs were characterized by transmission electron microscopy (TEM) whereas indium content distribution was by TEM-based energy-dispersive spectrometer (EDS). The photoluminescence (PL) spectra were studied on the optical properties of core-shell nanorods. In the measurement of temperature dependent photoluminance (TDPL), the degree of polarization effect was investigated. And the faster radiative lifetime by reducing the quantum confine Stark effect (QCSE) was estimated via the time-resolved photoluminesce (TRPL). Calculating the radiative lifetime by IQE and dynamic carrier lifetime, the dimensional of exciton emission in nanostructure will be fitted. In chapter 5, the finite-difference time-domain (FDTD) will be introduced to simulate the light extraction efficiency (LEE) enhancement of the conversional of pattern sapphire substrate (PSS) c-plane LED is about 45% and Core-shell LED is about 147%. Finally, the L-I-V curves of Core-shell LEDs were investigated by electroluminescence (EL) measurement. The emission region of Core-shell LED was altered with the increasing injection current, and the result was in agreement with the simulation result with finite element method (FEM). Those detailed results will be shown in the following chapters.

3.4 Reference

[1] J. Wu, *et al.*, "Small band gap bowing in In1−xGaxN alloys," *Applied Physics Letters*, vol. **80**, p. 4741, 2002.

[2] P. T. Barletta, *et al.*, "Development of green, yellow, and amber light emitting diodes using InGaN multiple quantum well structures," *Applied Physics Letters*, vol. **90**, p. 151109, 2007.

[3] D. Fuhrmann, *et al.*, "Optimization scheme for the quantum efficiency of GaInN-based green-light-emitting diodes," *Applied Physics Letters*, vol. **88**, p. 071105, 2006.,.

[4] Y. L. Lai, *et al.*, "Effects of the material polarity on the green emission properties of InGaN/GaN multiple quantum wells," *Applied Physics Letters*, vol. **89**, p. 151906, 2006.

[5] F. Bernardini, *et al.*, "Spontaneous polarization and piezoelectric constants of III-V nitrides," *Phys. Rev. B*, vol. **56**, p. R10024, 1997.

[6] N. Akopian, *et al.*, "Optical evidence for lack of polarization in (11-20) oriented GaN/(AlGa)N quantum structures," *Applied Physics Letters*, vol. **86**, p. 202104, 2005.

[7] M. Ueda, *et al.*, "Epitaxial growth and optical properties of semipolar (11-22) GaN and InGaN/GaN quantum wells on GaN bulk substrates," *Applied Physics Letters*, vol. **89**, p. 211907, 2006.

[8] R.Sharma, *et al.*, "Demonstration of a semipolar (10-13) InGaN/GaN green light emitting diode," *Applied Physics Letters*, vol. **87**, p. 231110, 2005.

[9] K. Hiramatsu, "Epitaxial lateral overgrowth techniques used in group III nitride epitaxy," *J. Phys.: Condens. Matter*, vol. **13**, p. 6961, 2001.

[10] T. Kim, *et al.*, "Highly efficient yellow photoluminescence from {11–22} InGaN multiquantum-well grown on nanoscale pyramid structure," *Applied Physics Letters*, vol. **97**, p. 241111, 2010.

[11] H. Yu, *et al.*, "Photoluminescence study of semipolar {10-11} InGaN/GaN multiple quantum wells grown by selective area epitaxy," *Applied Physics Letters*, vol. **90**, p. 141906, 2007.

[12] C. Liu, *et al.*, "Light Emission from InGaN Quantum Wells Grown on the Facets of Closely Spaced GaN Nano-Pyramids Formed by Nano-Imprinting," *Appl. Phys. Express*, vol. **2**, p. 121002, 2009.

[13] I. H. Wildeson, *et al.*, "GaN nanostructure design for optimal dislocation filtering," *J. Appl. Phys.*, vol. **108**, p. 044303, 2010.

[14] Y. H. Ko, *et al.*, "Electrically Driven Quantum Dot/Wire/Well Hybrid Light-

Emitting Diodes," *Adv. Mater.*, vol. **23**, p. 5364, 2011.

[15] Z. Zhang, *et al.*, "Effects of symmetry of GaN-based two-dimensional photonic crystal with quasicrystal lattices on enhancement of surface light extraction," *Applied Physics Letters*, vol. **88**, p. 171103, 2006.

[16] J. S. Speck and S. Rosner, "The role of threading dislocations in the physical properties of GaN and its alloys," *Physica B: Condensed Matter,* vol. **273**, p. 24-32, 1999.

[17] M. Zoorob, *et al.*, "Complete photonic bandgaps in 12-fold symmetric quasicrystals," *Nature*, vol. **404**, p. 740, 2000.

[18] N. A. Fichtenbaum, *et al.*, "Metalorganic chemical vapor deposition regrowth of InGaN and GaN on N-polar pillar and stripe nanostructures," *Japanese journal of applied physics*, vol. **46**, pp. L230-L233, 2007.

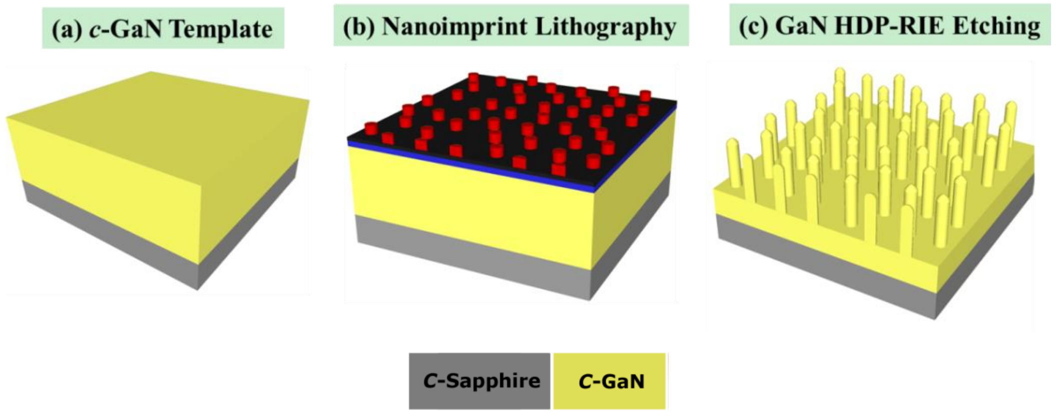

Figure 3-1. The flow chart for the fabrication of GaN nanorods. (a) A 2μm c-plane GaN template on c-plane sapphire substrate. (b) Prior to the etching process, a Ni, SiO_2 and photoresist thin film were deposited layer-by-layer on the underlying GaN template. Then the photoresist was patterned by the NIL process. (c) The pattern was transferred into the GaN template by dry etching process. The height, diameter and pitch size of GaN nanorods were 1μm, 350 nm and 750 nm, respectively.

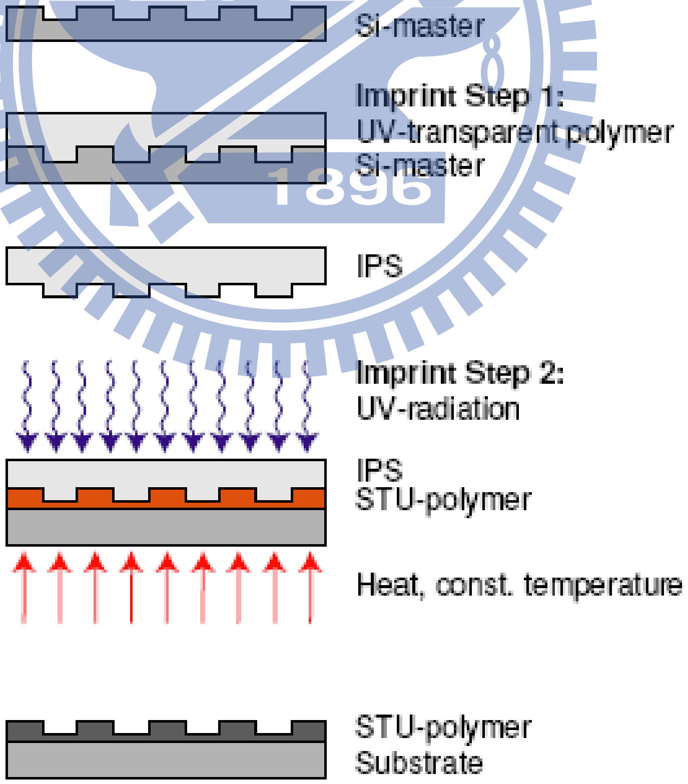

Figure 3-2. IPS-STU® technology of nano-imprint lithography, including Intermediate Polymer Stamp (IPS®) and Simultaneous Thermal and UV (STU®).

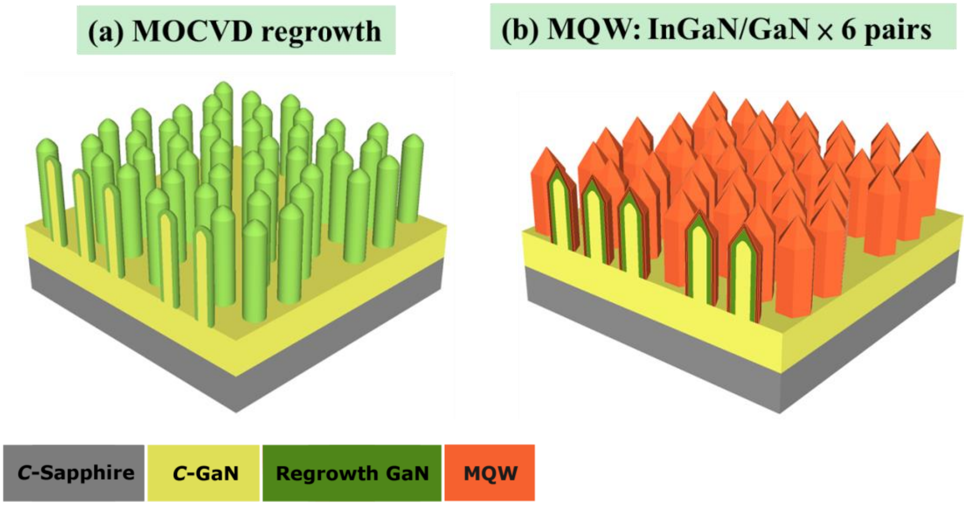

Figure 3-3. The schematic illustration of the regrowth process: (a) The deposition of n-GaN and the pre-strain layer on GaN nanorods. (b) Six pairs of InGaN/GaN MQWs conformally grew on GaN nanorods.

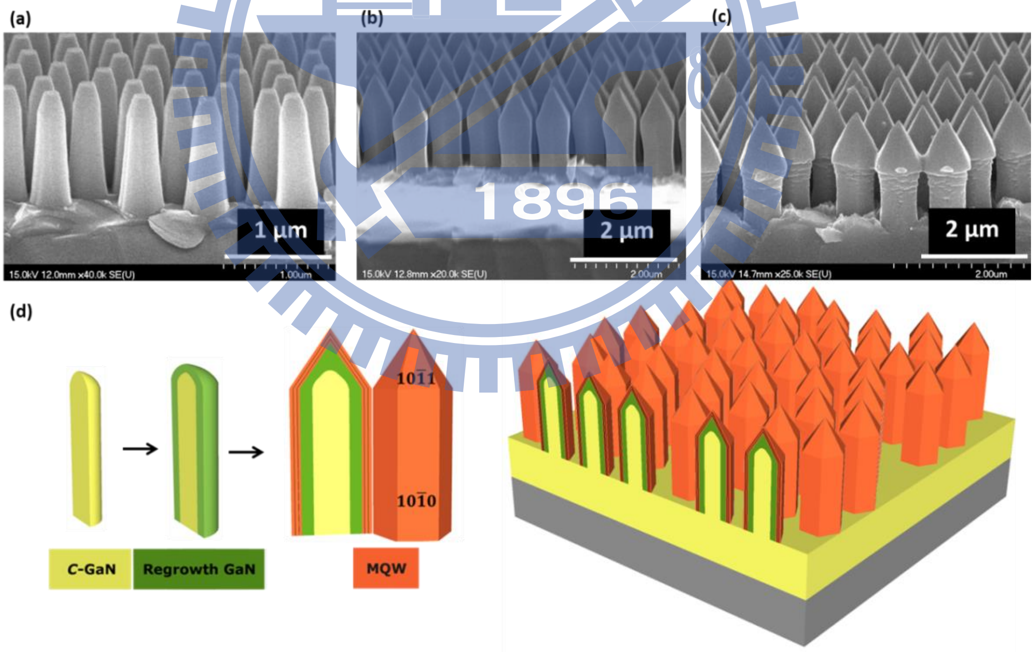

Figure 3-4. The SEM images viewed in 45°of (a) GaN nanorods, (b) the regrowth InGaN/GaN MQWs on GaN nanorods of sample HT and (c) sample LT, respectively. (d) The schematic representation of the regrowth process for core-shell nanorods.

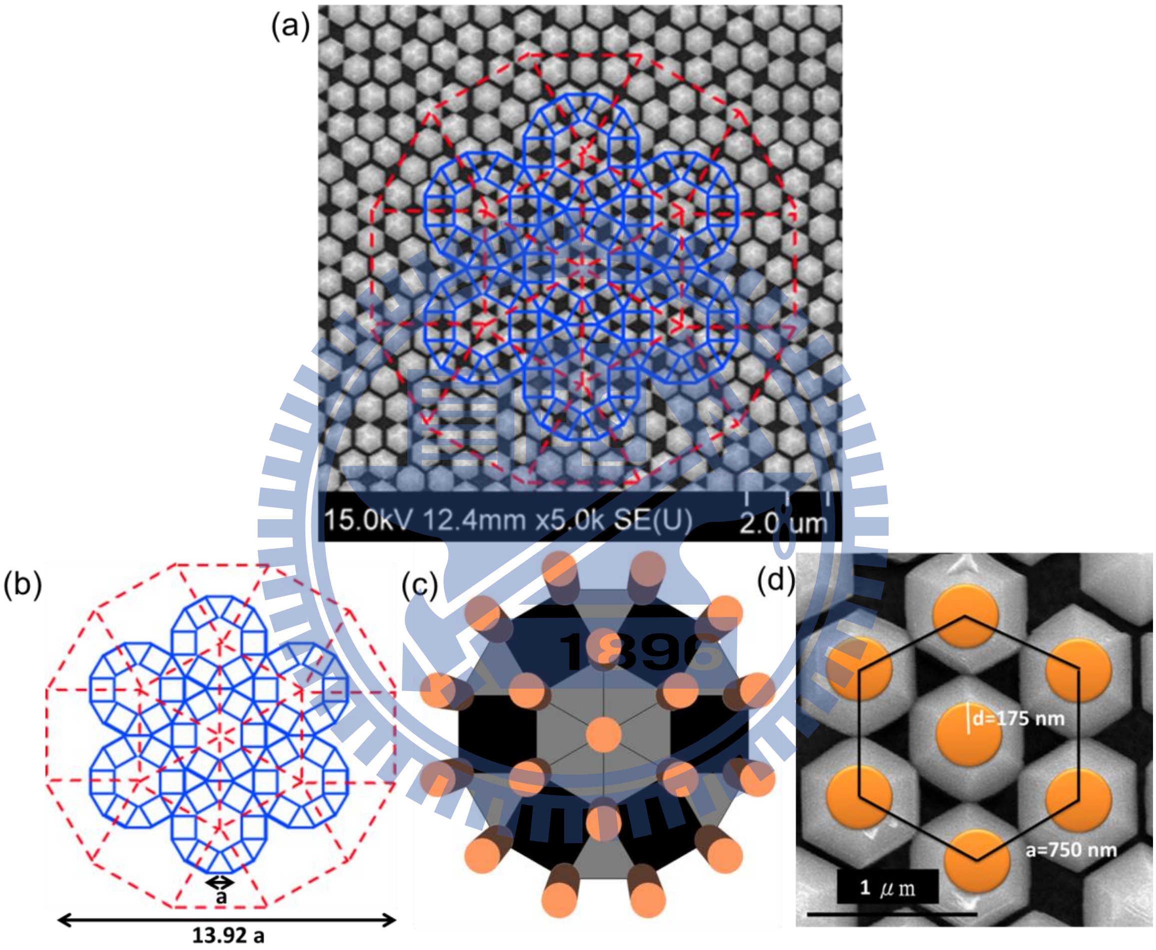

Figure 3-5. (a) Plane view SEM image of the fabricated nanorod arrays. (b) and (c) A 12-fold photonic quasicrystal pattern [3]. (d) The average radius and the pitch of nanorods are about 175nm and 750nm, respectively.

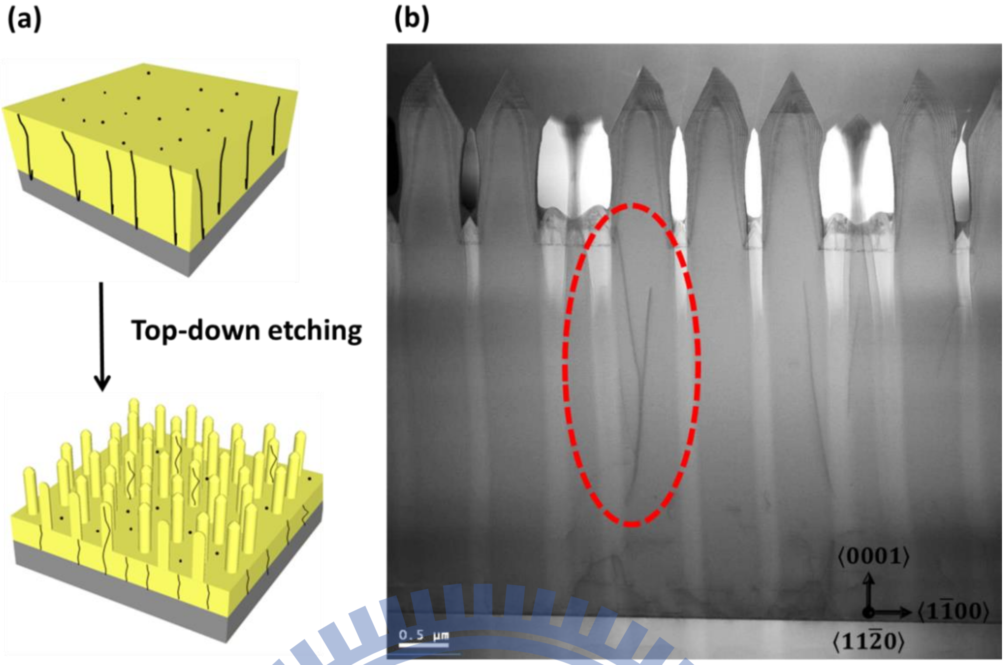

Figure 3-6. (a) The procedure illustration of defect reduced via NIL technology. (b) Cross-section STEM micrograph of sample HT. The red cicle indicate a TD which is buried in the underlying template.

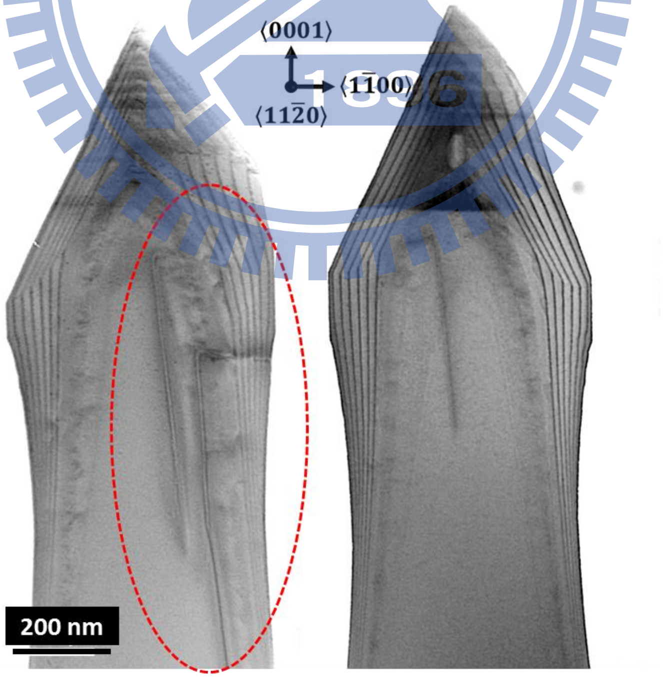

Figure 3-7. Cross-sectional STEM micrograph of core-shell nanorods with TDs were bended to side-wall surfaces and penetrate to the shell of MQWs, indicating by the red circle.

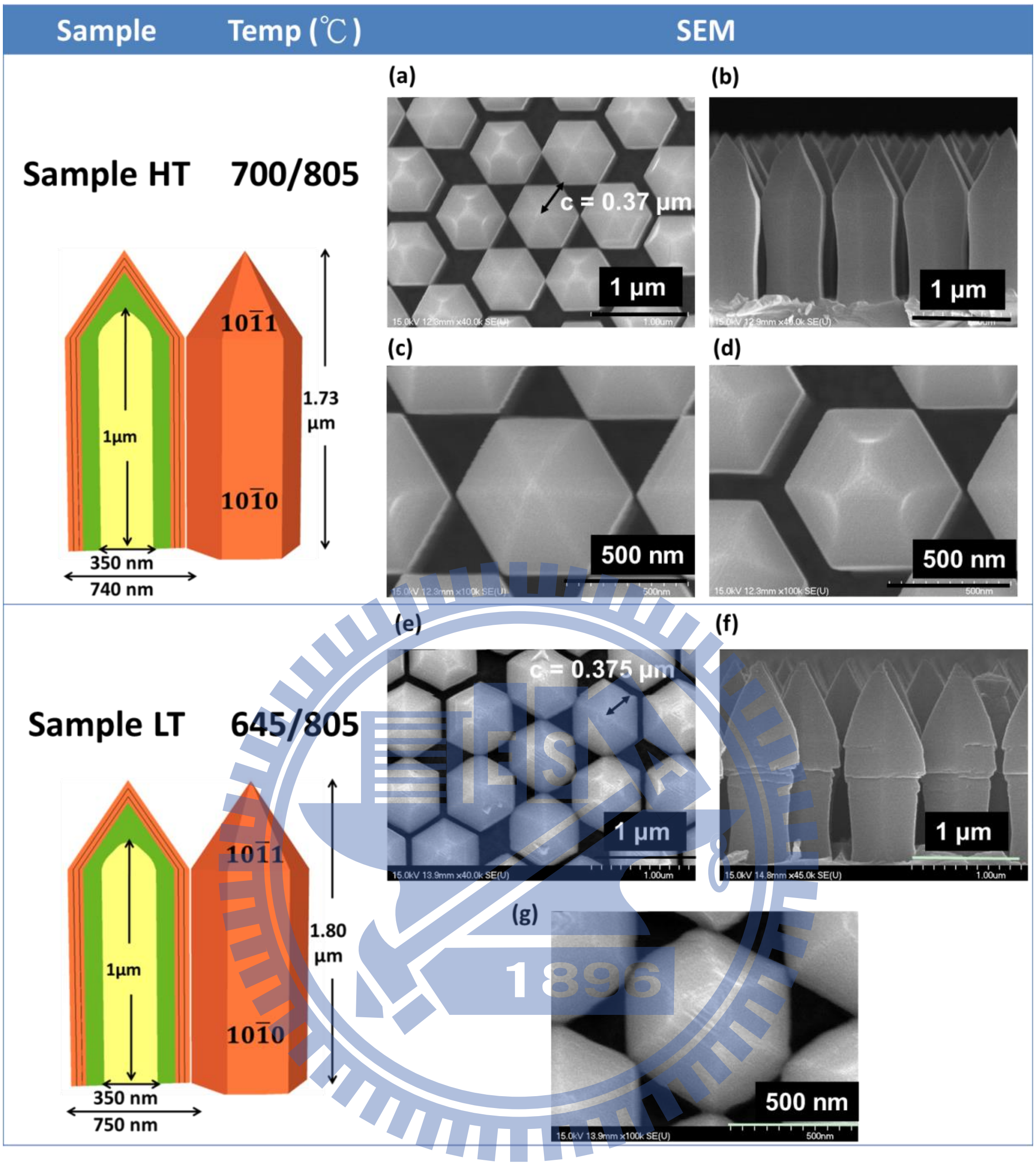

Figure 3-8. (a), (c), (d) and (b) are top-view and cross-section SEM images of sample HT, respectively. (e), (g) and (f) are top-view and cross-section SEM images of sample LT, respectively.

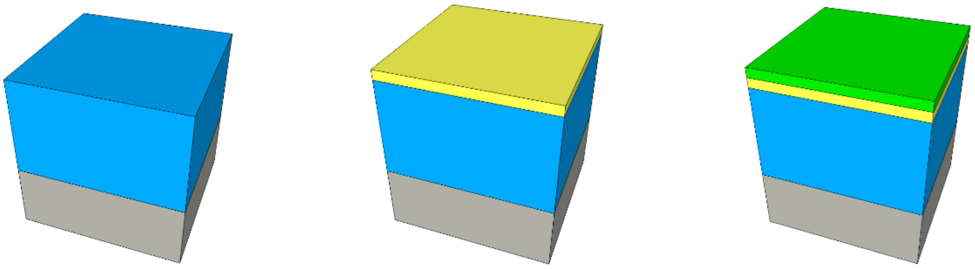

(a) MOCVD growth 3um n-GaN

(b) SiO_2 hard mask deposition by PECVD

(c) PMMA mask by spin coater

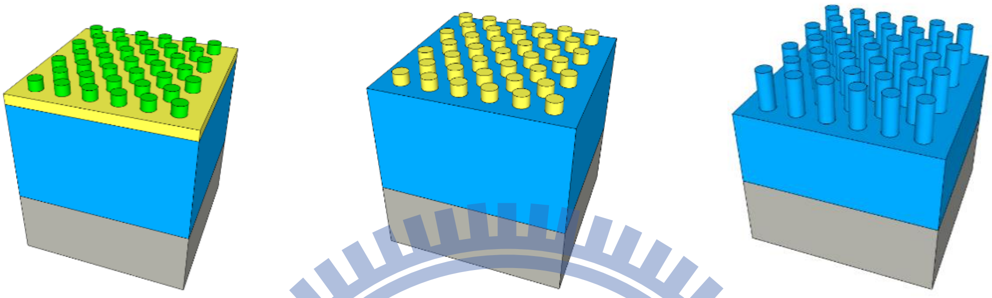

(d) nano imprint lithography

(e) hard mask transfer by ICP

(f) GaN nanorod formed by ICP

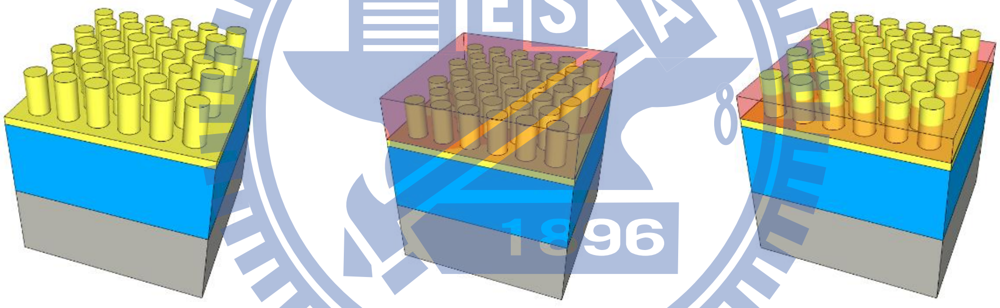

(g) passivation layer deposition by PECVD

(h) PMMA sacrificing layer by spin coater

(i) O_2 plasma descum

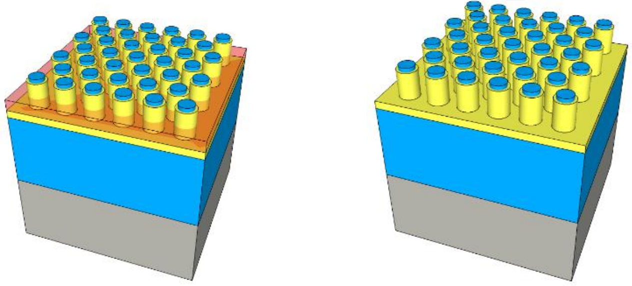

(j) top SiO2 remove by RIE

(k) PMMA remove by O_2 plasma

Figure 3-9. The evolution of sidewall passivation fabrication.

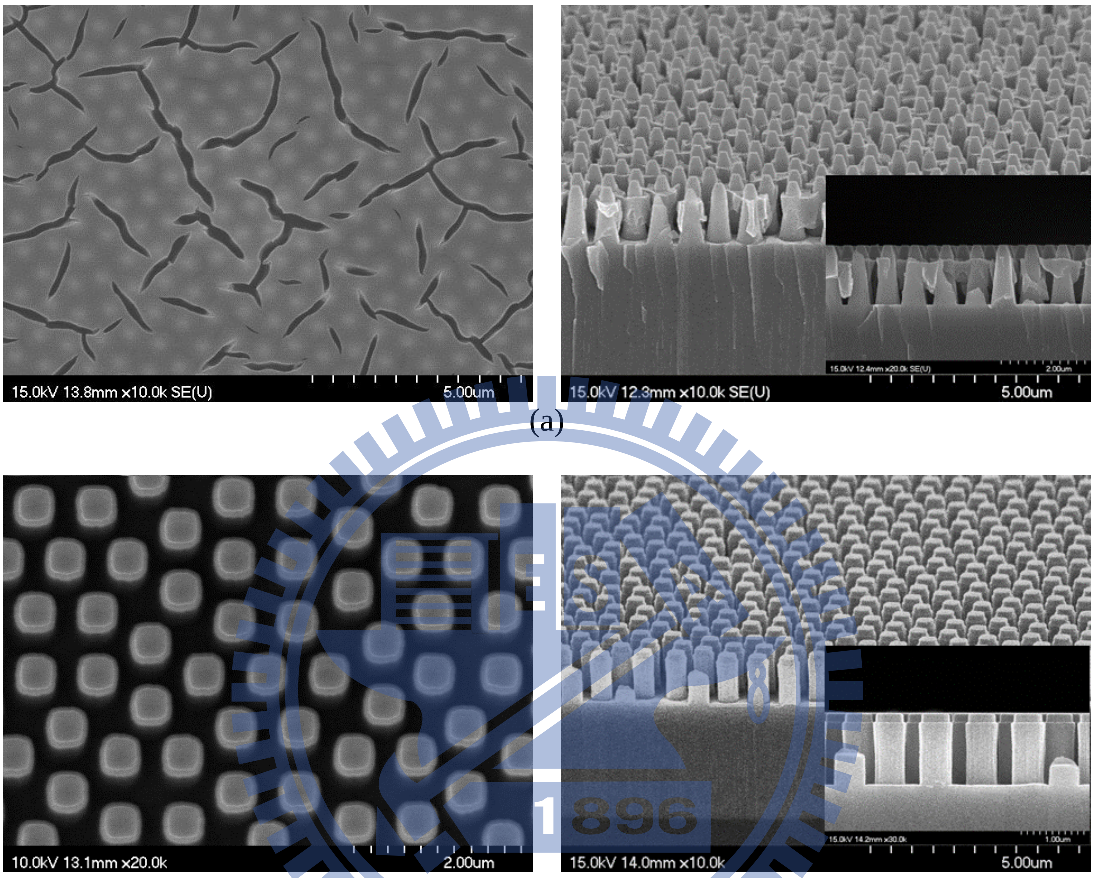

(a)

(b)

Figure 3-10. (a) side wall passivation using SOG and (b) PECVD.

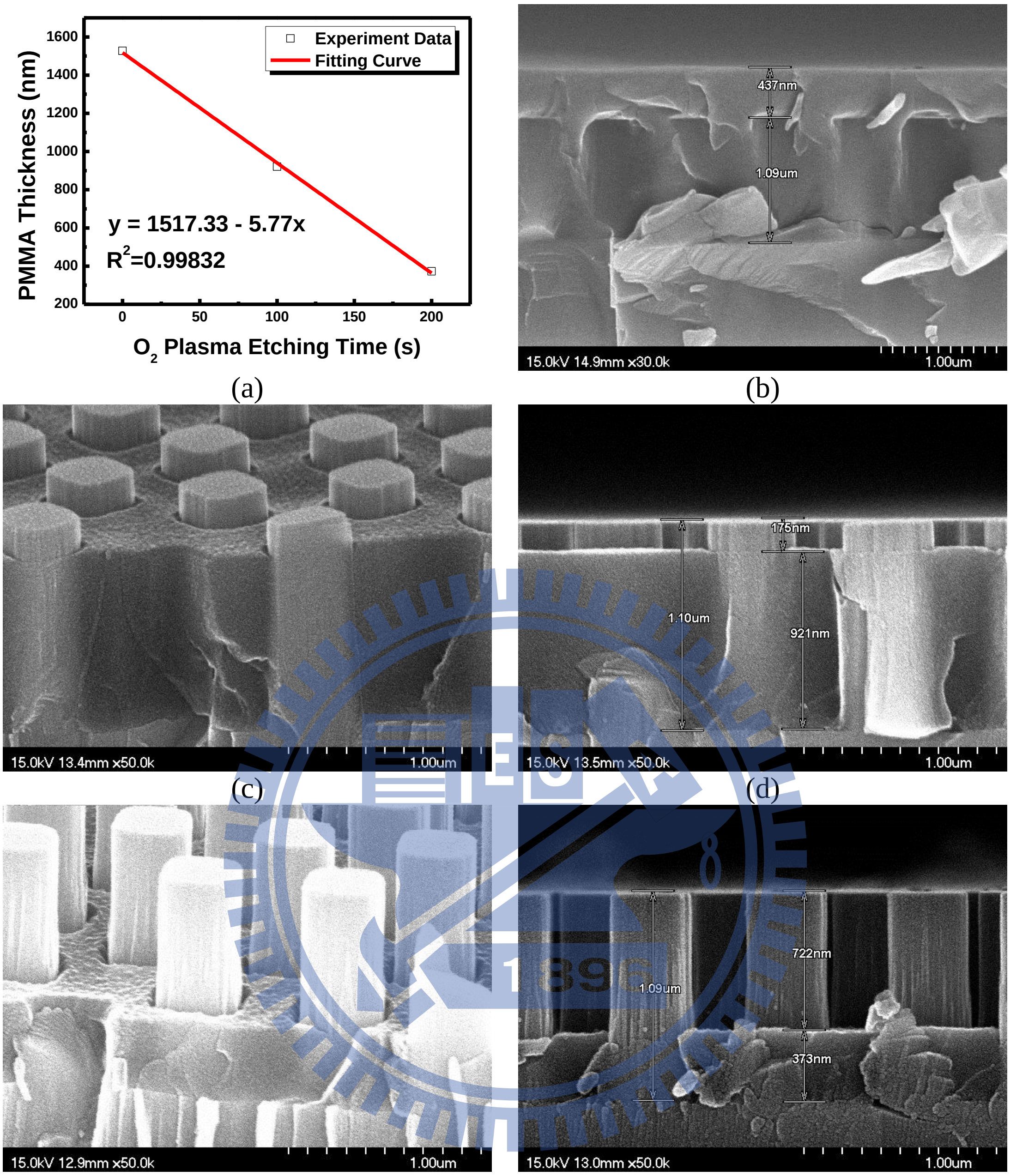

(a) (b) (c) (d) (e) (f)

Figure 3-11. (a) the fitting curve of the etching rate of PMMA in O_2 plasma; (b) cross section view of the nanorod template after PMMA coating; (c) bird's-eye view and (d) cross section view of 100s O_2 plasma etching; (e) bird's-eye view and (f) cross section view of 200s O_2 plasma etching.

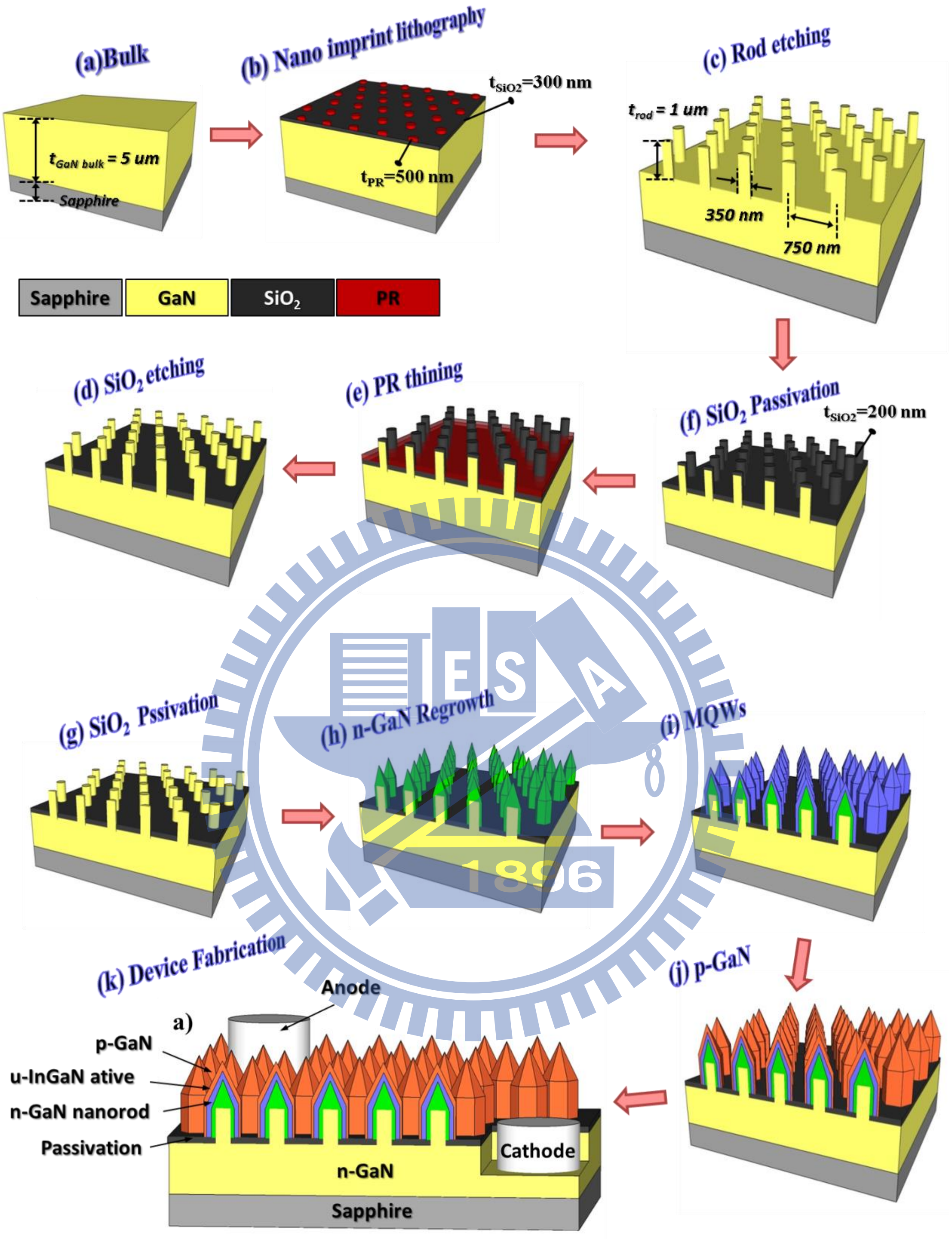

Figure 3-12. The fabrication flowchart of core-shell semipolar and nonpolar InGaN/GaN LEDs.

Chapter 4

Growth Mechanism of 3-D Core-shell InGaN/GaN Multi-Facet Qunatum Wells on Semipolar $\{10\bar{1}1\}$ and Nonpolar $\{10\bar{1}0\}$ plane

In recent years, significant interest has developed in the potential of using one dimensional GaN nano structures as an alternative design to improve the efficiency of the commonly-used planar structure GaN light emitting diodes. The nanopillar structure provides several advantages over the planar structure. The nanopillar exhibits a significantly reduced defect density because it has only a small area of contact with the growth template. This small footprint reduces strain from the lattice and thermal expansion coefficient mismatch between the GaN nanopillar and the growth template [1-3], thus reducing piezoelectric polarization and improving electron-hole recombination efficiency [4, 5]. The reduced strain also allows for higher In concentration in InGaN/GaN MQWs for green-red color emission applications [6-8]. These advantages have been demonstrated in MQWs grown in the nanopillar axial direction, which is often the c-axis crystal direction. The nanopillar offers an additional option to grow MQWs on the pillar surfaces in a core-shell geometry. These surfaces can be nonpolar or semipolar crystal planes with zero or low polarization fields. The MQWs grown on these planes have a lower carrier density dependent wavelength change and a higher radiative recombination efficiency [9-11]. This structure can also result in a much larger active surface area than found in MQWs grown on the nanopillar axial direction. Due to the nature of their three dimensional structure, the growth and emission properties of core-shell MQWs can vary with different crystal planes and require investigation.

In this chapter, the core-shell semipolar and nonpolar InGaN/GaN MQW nanopillar arrays were fabricated by top-down etching followed by epitaxial regrowth. The regrowth formed hexagonal sidewalls and pyramids on the nanopillars. Cathodoluminescence shows that QW emission blue shifts as the location moves from top to bottom on both the pillar sidewalls and pyramid facets, and the spectrum expands about 100 nm. The MQWs grown on the pillar sidewalls have a higher In concentration than those grown on the pyramid facets. The photoluminescent wavelength is stable over two orders of carrier density change due to the smaller quantum confined Stark effect of the nanopillar facets.

4.1 Crystalline Quality and Indium Distribution of 3-D Core-shell InGaN/GaN Multi-Facet Qunatum Wells on Semipolar $\{10\bar{1}1\}$ and Nonpolar $\{10\bar{1}0\}$ Plane

The core-shell nanorods with different crystalline orientation nano-facets were formed by NIL technology and controlled by the parameters in the regrowth process of MOCVD reactor. The further investigation for the structural specifics with the relation of the compositional incorporation efficiencies for InGaN/GaN MQWs was manipulated by TEM and EDS. Electron diffraction patterns were usually obtained from TEM analyses and used for characterizing the crystal structure of material. In this case, selected area electron diffraction (SAED) was brought to expolre the specifice region of the specimen, confirmed core-shell GaN nanorods with single-cyrstal nature and the different crystalline orientations of nano-facets. Using focused ion beam cutted a nanorod with the direction perpendicular to *m*-planes, the top-view SEM images were shown as in Figure 4-1 (a) and Figure 4-2 (a). The TEM image of Figure 4-1 (b) and Figure 4-2 (b) viewed in $\langle 11\bar{2}0\rangle$ zone axis revealed that the conformal InGaN/GaN MQWs were grown on GaN nanorods. Figure 4-1 (b) and Figure 4-2 (b) showed SAED pattern from the individual core-shell nanorod, the electron beam was incident perpendicular to the GaN $(11\bar{2}0)$ plane, pointing out the central intense and an array of diffraction spots from different atomic planes. The zone axis was the direction along the intersection of two or more planes passing through the central intense. Accordingly, it is recognized that four side planes of the nanorods are mainly to be two $\{1\bar{1}00\}$ of sidewalls and two $\{10\bar{1}1\}$ of a pyramidal top, as shown in Figure 4-1 (d).

In the following, the exploration aimed at each point for B-F on semipolar or nonpolar surfaces of sample HT, as shown in Figure 4-1 (b). Along the perpendicular direction to the surfaces, the indium incorporation efficiency, the well and the barrier growth rate on nano-facets as a function of the distance from the inner to outer MQWs are described in Figure 4-1 B-F.

First, the mass transport model [12] is introduced to describe the indium incorporation efficiency of core-shell nanorods. The higher indium content of $\{10\bar{1}1\}$ planes (16.40%, Figure 4-1 B) is compared to $\{1\bar{1}00\}$ planes (14.60%, Figure -1 E), The above phenomenon is attributed to different adatom reaction rates in the surface diffusion process, as the expression of continuity equation as follows:

$$\frac{\partial C_s}{\partial t} = D_s \frac{\partial^2 C_s}{\partial x^2} - \frac{C_s}{\tau} \tag{4.1}$$

where *Ds* is the diffusion constant and τ is the mean lifetime of the precursor concentration in diffusible status on the epitaxial surfaces, .

The surface diffusion constants of indium and gallium atoms on different orientation crystalline planes can be stated by the following equations [13]:

$$D_s = \left(\frac{k_B T}{25\tau_c \gamma}\right)\left(\frac{R}{a}\right)^4 \tag{4.2}$$

where k_B is the Boltzmann constant, τ_c is the coalescence time, T is the growth temeprature, R~250 nm is the domain radius and a~0.3 nm is the atomic dimension.

The adatom reaction rate is influenced by the density of atomic sites that are correlated with the surface energy. Therefore, the growth rate of the reactants on each facet was mainly influenced by the large surface energy with the large density of atomic sites [12]. The surface energies of GaN $\{10\bar{1}1\}$ planes and $\{1\bar{1}00\}$ planes are 181.2 meV/Å ^{2} and 137.7 meV/Å ^{2} [14], respectively. Therefore, the higher incorporation efficiency is predictable for semipolar planes than nonpolar planes.

In the other hand, the indium content from point A to point B on $\{10\bar{1}1\}$ plane is from 18.60% to 8.86% and from point D to point E on $\{1\bar{1}00\}$ planes is from 11.64% to 10.20%. The gradual indium content distribution on each facet is originated from the gas phase diffusion. The gas phase diffusion constant is given by [12]:

$$D = D_{ref}\left(\frac{P_{ref}}{P}\right)\left(\frac{T}{T_{ref}}\right)^{1.7} \tag{4.3}$$

where $T_{ref} = 300\ \mathrm{K}$, $P_{ref} = 760$ Torr and $D_{ref} = 0.29$ cm^2/s for TMGa and TMIn. As a result, under the same pressure at 300 Torr, the gas phase diffusion constant is 7.302 cm^2/s at 645 ℃ and 6.614 cm^2/s at 700 ℃.

The accumulation of indium atoms was observed at the intersection of growth facets, such as the apex of nanorods (19.8%), and the border region between $\{10\bar{1}1\}$ facets and $\{1\bar{1}00\}$ facets (25%, Figure 4-1 C). Here, the second growth model of surface modification [15] will be introduced to describe this phenomenon. The high accumulation at the intersection of facets can be ascribed to the chemical surface potential lowering by the nucleation process. Of note, asymmetrical thickness distribution for InGaN/GaN MQWs on the two $\{10\bar{1}1\}$ facets is observed in the TEM image. Due to $\{10\bar{1}1\}$ planes have an inclination angle of 62° relative to *c*-plane, the thick right-side inclination plane is the $\{10\bar{1}2\}$ facet. According to indium content of MQWs as a function of distance which is perpendicular to the central position of inclination planes on both sides, are described in Figure 4-1 B and F. The indium content increases from ~ 5.40% to ~16.40% on the left side and ~8.60% to ~31.20% on the right side. For the new-born $\{10\bar{1}2\}$ facets on $\{10\bar{1}1\}$ planes supposedly result in the tendency to minimize its total strain energy during growth process.

Under a reduced growth temperature of MQWs from 700℃ to 645℃, the discussion aimed at each point for A-D and F on semipolar or nonpolar surfaces of sample LT, as shown in Figure 4-2 (b). Along the perpendicular direction to the surfaces, the indium incorporation efficiency, the well and the barrier growth rates on nano-facets as a function of the distance from the inner to outer MQWs are described in Figure 4-2 A-D and F. The indium content of $\{1\bar{1}00\}$ planes (Figure 4-2 D) was observed higher than that of $\{10\bar{1}1\}$ planes (Figure 4-2 B). This phenomenon is not accordance with the surface diffusion process in the mass transport model. Because the indium clusters were observed in the nonpolar planes, the higher indium content could be expected, as shown in Figure 4-2 (d).

The second growth model of surface modification includes the accumulation of indium atoms, which was observed at the intersection of growth facets, such as the apex of nanorods (40.36%), and the border region between $\{10\bar{1}1\}$ facets and $\{1\bar{1}00\}$ facets (44.44%, Figure 4-2 C). Of note, asymmetrical thickness distribution for InGaN/GaN MQWs on the two $\{10\bar{1}1\}$ facets is observed in the TEM image. The thick right-side inclination plane is a $\{10\bar{1}2\}$ facet. According to indium content of MQWs as a function of distance which is perpendicular to the central position of inclination planes on both sides, is described in Figure 4-2 B and F. Indicating that the indium content increases from ~ 4.55% to ~20.31% on the left side and ~15.60% to ~36.80% on the right side. For the new-born $\{10\bar{1}2\}$ facets on $\{10\bar{1}1\}$ planes supposedly result in the tendency to minimize its total strain energy during growth process. In addition, the maximum indium incorporation efficiency usually occurs at the much low growth temperature, due to the thermodynamical stability and the weak In-N bond [16]. Therefore, the indium content for point A-F of sample HT was observed higher than that of sample LT, as shown in Table 4.1.

4.2 Spatial Cathodoluminescence Emission of 3-D Core-shell InGaN/GaN Multi-Facet Qunatum Wells on Semipolar $\{10\bar{1}1\}$ and Nonpolar $\{10\bar{1}0\}$ Plane

To evaluate indium incorporation of core-shell InGaN/GaN MQWs grown on GaN nanorods, the room temperature cathodeluminescence (CL) measurements were performed on both samples in a field-emission SEM using an acceleration voltage of 10 kV. A representative SEM image of sample HT with exposed top-view is shown in Figure 4-3 (a). The SEM scattering electron detection was switched to CL detection under the same magnification. The spatially integrated CL spectrum of the top-view image is shown in Figure 4-3 (b). The monochromatic intensity maps for the different emission energies distinguishable in the CL spectrum are shown in Figure 4-3 (c)-(k). Roughly speaking, the quantum well emission wavelength with red shift moves as the location from the edge to apex of a pyramid top on nanorods.

A further investigation of emission energies with location of nanorod is shown in cross-section SEM image (Figure 4-4 (a)) of sample HT. The spatially integrated CL spectrum of the cross section image is shown in Figure 4-4 (b). The first peak around 365 nm is the emission from *c*-plane GaN template. The large broad emission peak is from the shell of InGaN/GaN MQWs. To reveal the sources of the broad spectrum, the spectrally resolved CL images are shown in Figure 4-4 (c)-(i). The quantum well emission wavelength red shift as the location moves from the bottom to the top of nanorods. This red shifted emission may attribute to the decrease of indium diffusion into the bottom portion of nanorod during quantum well growth. As a result, the indium concentration in wells increases with nanorod heights, and emission red shifts accordingly.

Figure 4-5 (a) presents a cross section TEM image of this pillar taken through the pyramid center along the dashed line shown in Figure 4-6 (b). This cross section was chosen to show both the normal facet growth and the peculiar pyramid facet evolution mentioned above. From the electron diffraction pattern, the inclined pyramid facets and the pillar sidewalls are, respectively, identified as $\{10\bar{1}1\}$ and $\{10\bar{1}0\}$ planes, revealing the coreshell MQW structure. Figure 4-5 (a) also shows the QW and barrier thickness, and InN fractions at various locations. The InN fraction was measured by the energy dispersive x-ray spectroscopy. The six InGaN MQWs, showing a dark color in contrast to the GaN barriers, provide snap shots of the evolution. The first InGaN QW shows a pyramid contour on the top and slightly tapered pillar sidewalls. This indicates that the GaN regrowth has grown a pyramid on the top while the pillar still has a slightly tapered shape prior to the first QW growth. The first QW pyramid contour is rather symmetric. As the growth continues, the symmetry is broken. The QWs on the upper right portion gradually protrude because of the facet evolution among facets 1, 2, and 3, as shown in Figure 4-6 (c). A sharp turning corner is developed at the junction between the pyramid facets and pillar sidewalls as GaN grows from the first to second QW (dotted line circles in Figure 4-5 (b)), indicating the formation of crystalline facets. The growth rate of the upper part of pillar sidewall is faster than that of the lower part, producing a pillar that gradually narrows towards the base. The slower growth rate at the bottom is due to the limited available source diffused to the bottom. The 25% InN fraction at the upper sidewall is much greater than the 16% at the adjacent pyramid facet, indicating that the $\{10\bar{1}0\}$ plane can accommodate higher InN fraction in InGaN MQWs than the $\{10\bar{1}1\}$ plane. The percentage drops to 11.6% in the bottom portion of nanopillars, due to the less available In source diffused to the bottom. This large facet and geometry dependent InN fraction change produce a broad 100 nm overall emission bandwidth, which could be useful in white light LED applications.

4.3 Summary

In addition to the intrinsic low polarization field of these crystal planes, the small footprint of 3D nano structure on the substrate can also provide better strain relaxation, resulting in lower defect density and the further reduction of the piezoelectric field. Photoluminescent (PL) studies of MQWs grown on these nano-scale facets have demonstrated significant reduction in the polarization field and the increase of internal quantum efficiency [17, 18]. There have been strong interests in using these semipolar pyramids and nonpolar facets for LED applications, in particular high In content LEDs [19, 20]. The experiments were however mostly carried out by photo excitation. Reports on electrical performance are very limited [20, 21]. A thick layer of p-GaN was grown on top of the nanopyramids to planarize the surface for electrical contacts, which could compromise the electrical performance due to its high resistivity [20, 21]. Even though the core-shell structure shows promising advantages in optical emission properties, the 3D nano geometry often poses challenges for making electrical injection, which is an important issue for practical device realization.

In summary, we have fabricated core-shell MQW nanopillar arrays by patterned top-down etching and a subsequent epitaxial regrowth. The regrowth results in crystalline hexagonal pyramid nanopillars with $\{10\bar{1}0\}$ nonpolar sidewalls and $\{10\bar{1}1\}$ semipolar pyramid facets. The MQWs grown on these facets have large location dependent InN fraction variations. Furthermore, the top-down etching via the NIL process translated 12-fold PQC pattern and eliminated dislocations on the template. The defect density is reduced at the magnitude of one order. The active area of core-shell nanorods under the regrowth process of MQWs is enlarged by a factor of 5. Two models are introduced to explain the different indium incorporation efficiency on core-shell nano-facets nanorods: first, the mass transport model includes the surface diffusion process and the gas phase diffusion process. The higher indium incorporation efficiency of $\{10\bar{1}1\}$ planes is compared to $\{1\bar{1}00\}$ planes by the different surface energy in the surface diffusion process. The gradient indium content distribution on each facet is described by the gas phase diffusion process. Second, the surface modification model, including the chemical potential is lowered by the intersection of growth planes and the strain is relaxed by the new-born $\{10\bar{1}2\}$ facets. The high indium contents were observed in the new-born facets, the pyramid tip and in the border region between semipolar and nonpolar facets of core-shell nanorods. Core-shell nanorods with the higher indium content can be attained by a reduced regrowth temperature of MQWs. Under a reduced regrowth temperature, the degraded sidewall surfaces of core-shell nanorods were caused by the lower species mobility with the lower temperature.

4.4 References

[1] J. Chang, *et al.*, “Strong luminescence from strain relaxed InGaN/GaN nanotips for highly efficient light emitters, ” *Opt. Express,* vol. **15**, p. 9357, 2007.

[2] J. Renard, *et al.*, “Evidence for quantum-confined Stark effect in GaN/AlN quantum dots in nanowires, ” *Phys. Rev. B*, vol. **80**, p. 121305, 2009.

[3] Q. Li and G. Wang, “Strain influenced indium composition distribution in

GaN/InGaN core-shell nanowires," *Appl. Phys. Lett.*, vol. **97**, p. 181107, 2010.

[4] Y. L. Chang, *et al.*, "High efficiency green, yellow, and amber emission from InGaN/GaN dot-in-a-wire heterostructures on Si(111)," *Appl. Phys. Lett.*, vol. **96**, p. 013106, 2010.

[5] Y. J. Hong, *et al.*, "Visible-Color-Tunable Light-Emitting Diodes," *Adv. Mater.*, vol. **23**, p. 3284, 2011.

[6] H. Sekiguchi, *et al.*, "Emission color control from blue to red with nanocolumn diameter of InGaN/GaN nanocolumn arrays grown on same substrate," *Applied Physics Letters*, vol. **96**, p. 231104, 2010.

[7] H. P. T. Nguyen, *et al.*, "Controlling Electron Overflow in Phosphor-Free InGaN/GaN Nanowire White Light-Emitting Diodes," *Nano Lett.*, vol. **12**, p. 1317, 2012.

[8] H. W. Lin, *et al.*, "InGaN/GaN nanorod array white light-emitting diode," *Applied Physics Letters*, vol. **97**, p. 073101, 2010.

[9] R. Koester, *et al.*, "M-Plane Core–Shell InGaN/GaN Multiple-Quantum-Wells on GaN Wires for Electroluminescent Devices," *Nano Lett.*, vol. **11**, p. 4839, 2011.

[10] C. H. Lee, *et al.*, "GaN/In1−xGaxN/GaN/ZnO nanoarchitecture light emitting diode microarrays," *Appl. Phys. Lett.*, vol. **94**, p. 213101, 2009.

[11] T. W. Yeh, *et al.*, "Vertical nonpolar growth templates for light emitting diodes formed with GaN nanosheets," *Appl. Phys. Lett.*, vol. **100**, p. 033119, 2012.

[12] H. Fang, *et al.*, "Analysis of mass transport mechanism in InGaN epitaxy on ridge shaped selective area growth GaN by metal organic chemical vapor deposition," *Journal of Applied Physics*, vol. **103**, p. 014908, 2008.

[13] V. Lebedev, *et al.*, "Coalescence aspects of III-nitride epitaxy," *Journal of Applied Physics*, vol. **101**, pp. 054906-054906-12, 2007.

[14] V. Jindal and F. Shahedipour-Sandvik, "Theoretical prediction of GaN nanostructure equilibrium and nonequilibrium shapes," *Journal of Applied Physics*, vol. **106**, pp. 083115-083115-7, 2009.

[15] W. Goh, *et al.*, "Structural and optical properties of nanodots, nanowires and multi quantum wells of III-nitride Grown by MOVPE nano selective area growth," *J. Cryst. Growth*, vol. **315**, pp. 160–163, 2010.

[16] G. Stringfellow, "Microstructures produced during the epitaxial growth of InGaN alloys," *Journal of crystal growth*, vol. **312**, p. 735-749, 2010.

[17] T. Kim, *et al.*, "Highly efficient yellow photoluminescence from {11–22} InGaN multiquantum-well grown on nanoscale pyramid structure," *Appl. Phys. Lett.*, vol. **97**, p. 241111, 2010.

[18] H. Yu, *et al.*, "Photoluminescence study of semipolar {10-11} InGaN／ GaN

multiple quantum wells grown by selective area epitaxy," *Appl. Phys. Lett.*, vol. **90**, p. 141906, 2007.

[19] C. Liu, *et al.*, "Light Emission from InGaN Quantum Wells Grown on the Facets of Closely Spaced GaN Nano-Pyramids Formed by Nano-Imprinting," *Appl. Phys. Express*, vol. **2**, p. 121002, 2009.

[20] I. H. Wildeson, *et al.*, "GaN nanostructure design for optimal dislocation filtering," *J. Appl. Phys.*, vol. **108**, p. 044303, 2010.

[21] Y. H. Ko, *et al.*, "Electrically Driven Quantum Dot/Wire/Well Hybrid Light-Emitting Diodes," *Adv. Mater.*, vol. **23**, p. 5364, 2011.

Table 4-1. The indium content distribution of point A-F for sample HT and sample LT.

Sample HT	**In%**	**Sample LT**	**In%**
A	**19.80**	**A**	**40.36**
B	**16.40**	**B**	**14.27**
C	**25/00**	**C**	**44.44**
D	**14.60**	**D**	**40.61**
E	**11.60**	**E**	**22.27**
F	**30.00**	**F**	**31.79**

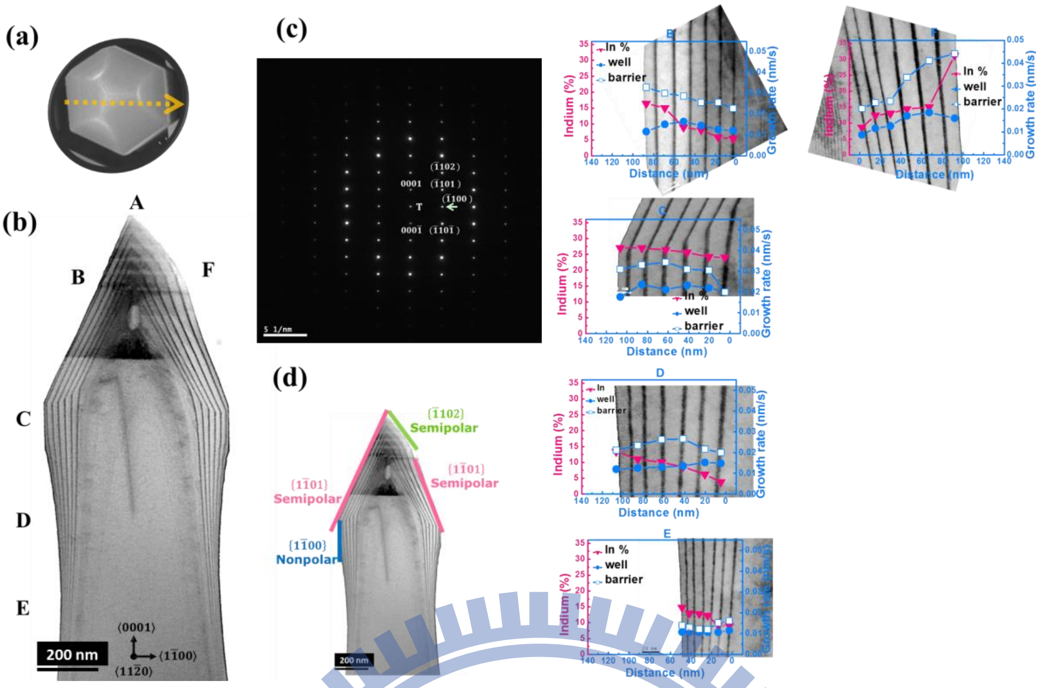

Figure 4-1. (a) A top-view SEM image of a GaN nanorod for sample HT. (b) A TEM micrograph of a core-shell nanorod view in the ⟨11$\bar{2}$0⟩ zone axis. (c) Electron diffraction pattern confirmed core-shell nanorods with single-cyrstal nature of zone axis. (d) The different crystalline orientation nano-facets on core-shell nanorods. B-F, the indium content distribution and the growth rate of InGaN/GaN wells and barriers versus distance with the normal direction at each point from the first to sixth pairs of MQWs.

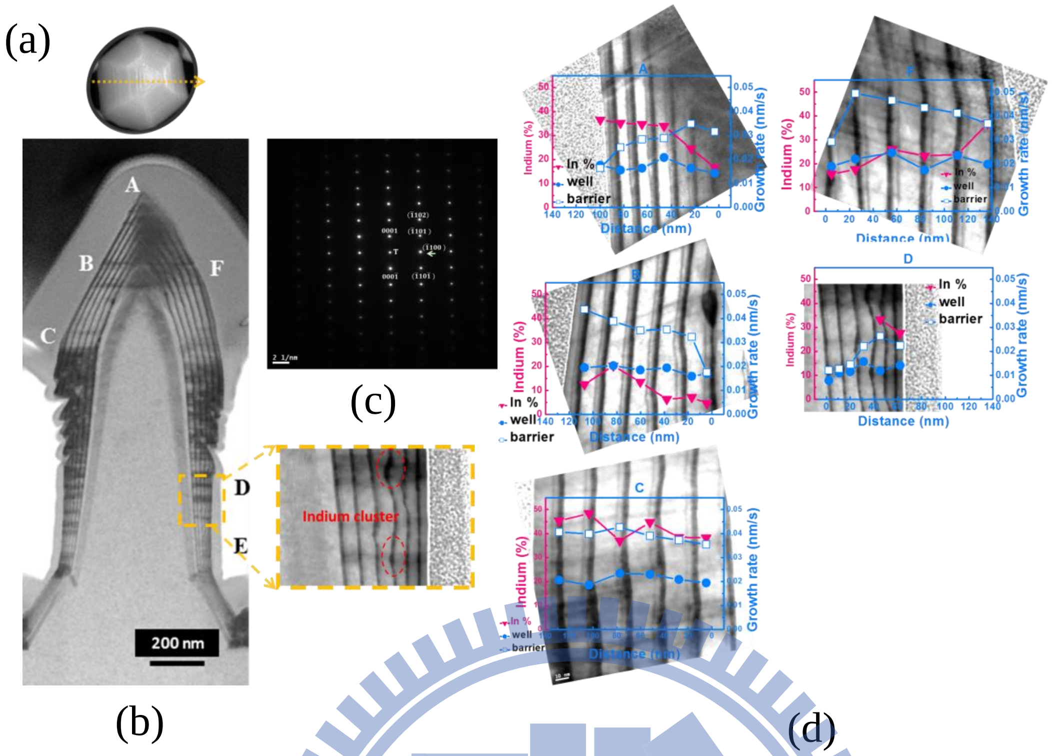

Figure 4-2. (a) A top-view SEM image of a GaN nanorod for sample LT. (b) A TEM micrograph of a core-shell nanorod view in the $\langle 11\bar{2}0 \rangle$ zone axis. (c) Electron diffraction pattern confirmed core-shell nanorods with single-cyrstal nature of zone axis. (d) Red circles show the indium clusters on nonpolar planes. A-D and F, the indium content distribution and the growth rate of InGaN/GaN wells and barriers versus distance with the normal direction at each point from the first to sixth pairs of MQWs.

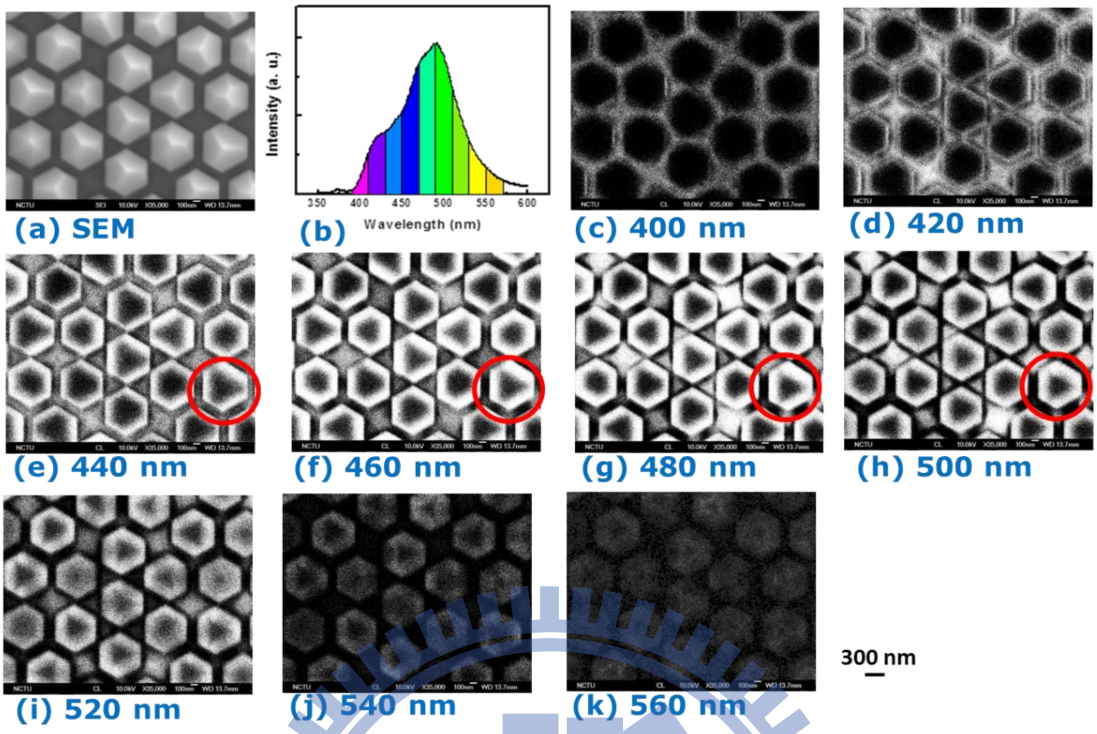

(a) SEM
(b)
(c) 400 nm
(d) 420 nm
(e) 440 nm
(f) 460 nm
(g) 480 nm
(h) 500 nm
(i) 520 nm
(j) 540 nm
(k) 560 nm

Figure 4-3. (a) SEM top-view image of sample HT. (b) Spatially integrated CL spectrum of (a). (c)-(i) Spectrally resolved CL images showing the location dependent emission wavelength of quantum wells.

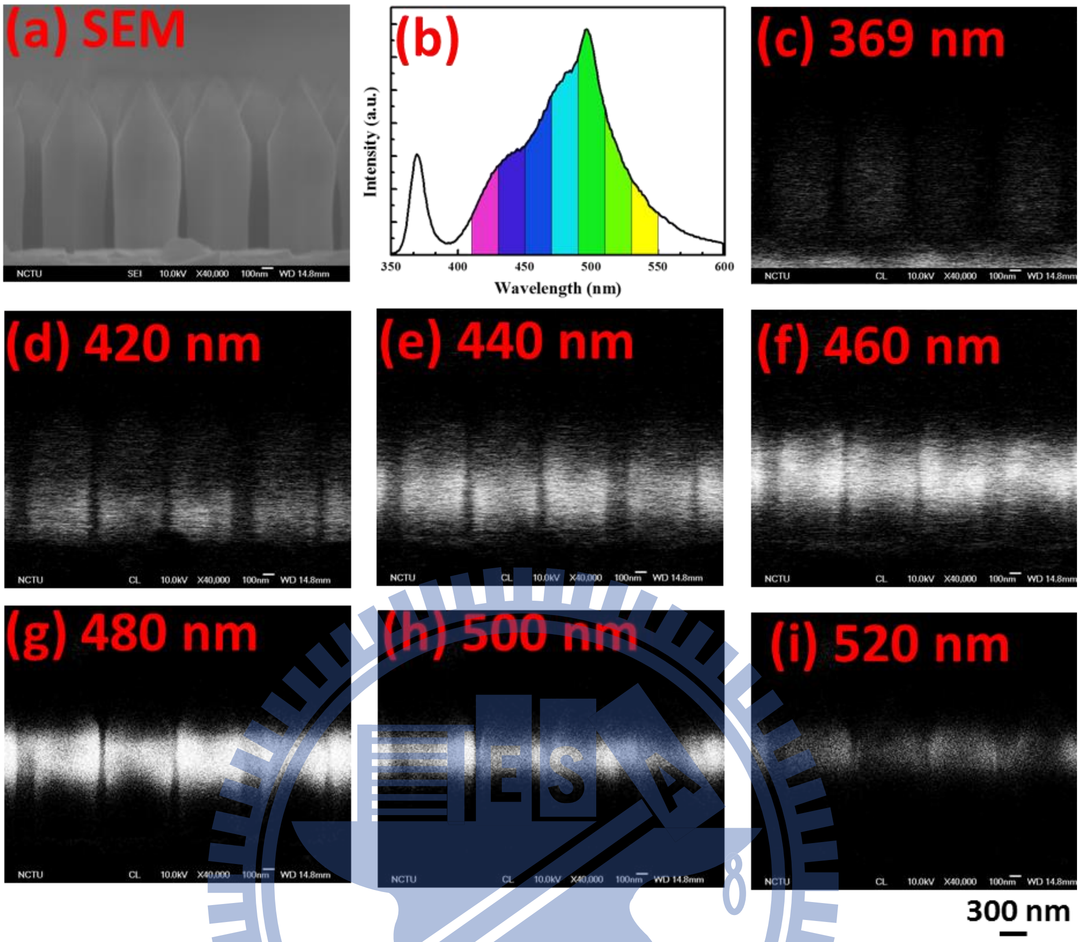

Figure 4-4. (a) SEM cross-section image of sample HT. (b) Spatially integrated CL spectrum of (a). (c)-(i) Spectrally resolved CL images showing the location dependent emission wavelength of quantusm wells.

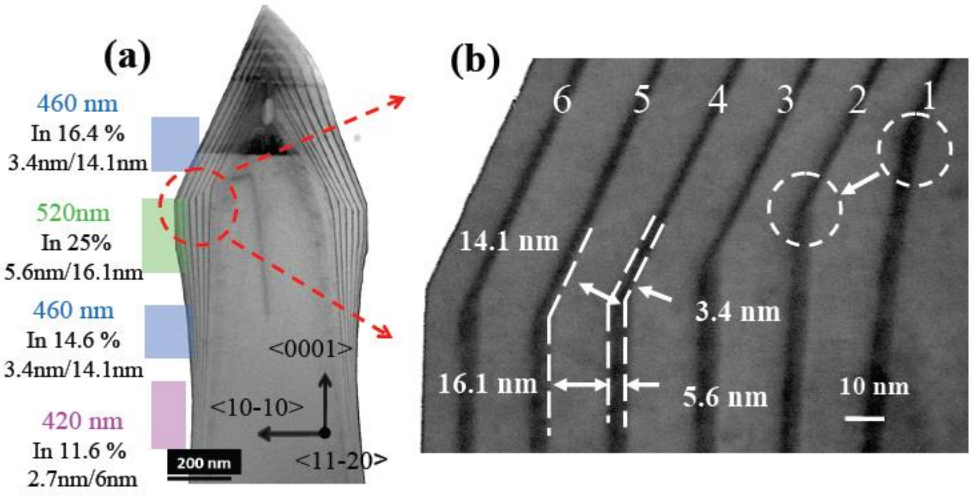

Figure 4-5. (a) TEM cross section view of a nanopillar, showing the growth of six QWs (dark colored lines), the InN fraction, and well/barrier thickness.(b) Close view at the pyramid facet and pillar sidewall junction.

Figure 4-6. (a) SEM top view of nanopillars showing two different pyramid geometries (labeled as H and T). (b) Close view of the pyramid T. (c) Schematic showing the facet evolution of pyramid T, transforming from hexagonal to triangular pyramid facets from bottom to top.

Chapter 5

Optical Properties of 3-D Core-shell InGaN/GaN Multi-Facet Qunatum Wells on Semipolar $\{10\bar{1}1\}$ and Nonpolar $\{10\bar{1}0\}$ Plane

InGaN alloys have been attracting much attention as potential materials for the fabrication of high brightness light emitting diodes (LEDs) and continuous wave (cw) blue laser diodes because of the advantage of tuning ability of the alloy bandgap. Understanding the emission mechanism in InGaN multiple quantum well (MQW) structures is a key issue for further developing such optoelectronics devices [1–3]. The widely accepted viewpoint is that the inhomogeneous distribution of indium facilitates high quantum efficiency of nitride-based LEDs in spite of the tremendous density of dislocations of InGaN/GaN MQWs grown on the lattice-mismatched substrates [4]. The localized excitons within indium-rich regions resulting from partial phase segregation in InGaN alloys are considered to prevent them from reaching nonradiative recombination sites and play an important role for spontaneous emission. However, to our knowledge, the character of carrier motion, and the relevant process of establishing their distribution over the localized states in InGaN remain to be further explored [5, 6].

Excitation power and temperature dependences of the photoluminescence (PL) spectra are studied in InGaN/GaN multiple quantum wells (MQWs). The excitation power dependences of the PL peak energy and linewidth indicate that the emission process of the MQWs is dominated first by the Coulomb screening effect and then by the localized states filling at low temperature, and that the nonradiative centers are thermally activated in low excitation range at room temperature. The anomalous temperature dependences of the peak energy and linewidth are well explained by the localized carrier hopping and thermalization process, and by the exponentially increased density of states with energy in the band tail. Moreover, it is also found that internal quantum efficiency is related to the mechanism conversion from nonradiative to radiative mechanism, and up to the carriers escaping from localized states.

The excitation power dependence of the emission intensity, together with that of the emission energy and linewidth, shows that the emission process of the MQWs is dominated by the radiative recombination at low temperature, and by nonradiative recombination at room temperature within low excitation range. The conclusion is also manifested in the excitation power dependence of the IQE. It is improved due to the pronounced enhancement of the radiative recombination mechanism at room temperature with increasing excitation power, and then tends to a constant with further increasing excitation power, this is because when band-filling effect dominates, the injected carriers escape more easily from localized states, especially at room temperature. Accordingly, we can conclude that to achieve a high-quantum efficiency of InGaN-based LED, it would be essential to overcome the nonradiative recombination, weaken the internal electric field in the QW, and increase the depth of localized states to suppress carriers escaping to extended states. The experimental results will provide a useful guidance to fabricate a high-performance LED with high-quantum efficiency.

5.1 Properties of Spatial Luminescence and Internal Electric Field

The commercial InGaN/GaN LEDs in blue emission usually built on *c*-plane GaN. Nevertheless, the strained quantum well structures were grown on polar *c*-axis, and polarization charges exist at the interface of InGaN/GaN layers. The induce electric fields can tilt the quantum well energy band and spatially separate electron and hole wavefunctions in quantum wells. These electric fields caused by both piezoelectric and spontaneous polarizations, resulting in large shifts of energy and intensity in optical and electrical measurements, known as quantum confined Stark effect (QCSE). To study the QCSE, the power-dependent photoluminescence (PL) spectrum of core-shell nanorods was measured at room temperature. The MQWs were excited by a 325 nm He-Cd laser, and the excitation power was varied by using neutral density filters. As shown in Figure 5-1 (a), the multiple peaks were fitting from the PL spectrum with the pumping power ranging between 0.1 to 12 mW, indicating that the emission wavelengths of the separated peaks were around 418 nm, 468 nm, 512 nm and 526 nm, respectively, as shown in Figure 5-1 (b). The peak energy of the emission line was observed small shift in emission peak wavelength with increasing the pumping power, as shown in Figure 5-1 (c). This phenomenon is attributed to the suppression of QCSE which is achieved by growing semipolar and nonpolar nano-facets of GaN nanorods. The same condition was observed in sample LT, a small spectral blue shift in emission peak wavelength with the pumping power ranging from 0.1 mW to 11 mW, as shown in Figure 5-1 (d) and (f). The multiple peaks were fitting from the PL spectrum with the pumping power, indicating that the emission wavelengths of the separated peaks were around 457 nm and 547 nm, respectively, as shown in Figure 5-1 (e).

Computed wavelengths of sample HT with the parameters of the indium content, the thickness for wells and barriers on the different crystalline nano-facets of core-shell nanorods were modeled by Advanced Physical Models of Semiconductor Devices (APSYS). As shown in Figure 5-2 (a), the computed wavelengths emitted from the bottom portion of $\{1\bar{1}00\}$ *m*-plane at 415 nm, the middle portion of $\{1\bar{1}00\}$ *m*-plane and $\{10\bar{1}1\}$ *s*-plane at 460 nm, the border region between $\{1\bar{1}00\}$ *m*-plane and $\{10\bar{1}1\}$ *s*-plane, and the nanorod tip at 507 nm. The above results are corresponds to location of nanorod for the spectrally resolved CL images at (iv) 420 nm, (i)&(iii) 460 nm and (ii) 520 nm, respectively, as shown in Figure 5-2 (b). The computed wavelengths also can be found in the multiple peaks fitting from the PL spectrum with the excitation power at 10 mW.

From the PL spectrum of the multiple peaks as the function of the pumping power, as shown in Figure 5-3 (a), the emission wavelengths of center 1, center 2, ceneter3 and center 4 are about 418 nm, 468 nm, 512 nm and 528 nm, respectively. According to Figure 5-2, different emission wavelengths can be assigned to different locations of a core-shell nanorod. Therefore, the emission wavelengths of center 1, center 2, ceneter3 and center 4 are emitting from nonpolar planes, both semipolar and nonpolar planes, semipolar planes, and nonpolar planes, respectively.

The internal electric field (IEF) of $In_{0.2}Ga_{0.8}N$ for (0001) MQWs is usually about 1.7MV/cm. The IEF of nonpolar and semipolar planes can be also determined by power dependent PL spectrum (Figure 5-3 (a)).

First, the magnitude of the surface electric field can be determined as given below [7]:

$$F_s = \left(\frac{-2V_s\rho}{\varepsilon\varepsilon_0}\right)^{\frac{1}{2}} \qquad (5.1),$$

where Fs is the surface electric field, Vs is the equilibrium surface voltage, ρ is the net charge density, ε is the low-frequency dielectric constant and ε_0 is the permittivity of free space.

When the p-n junction with ideal diode *I-V* characteristics is under illumination, the source I_L results from the excitation of excess carriers by the exciting light. The equivalent circuit is shown in Figure 5-4, where a constant-current source of photocurrent is in parallel with the junction. The total *I-V* characteristics of such devices are given by [8] :

$$I = I_s\left(exp^{eV/kT} - 1\right) - I_L \qquad (5.2),$$

where I_s is the diode saturation current, e is the electronic charge, V is the applied voltage, K is the Boltzmann constant and T is the absolute temperature.

Therefore, the equilibrium surface voltage Vs is obtained from the photoinduced current under the steady-state conditions [9] :

$$V_s = V_{so} \pm \frac{kT}{e} ln(bN + 1) \qquad (5.3),$$

where V_{s0} is the surface potential, b is an intensity-independent constant given by:

$$b = ex\,p\left(\frac{eV_{so}}{kT}\right)\left(\frac{e}{AT^2}\right) \qquad ,$$

where A is the modified Richardson constant. The surface potential Vso, has been measured by a number of research groups and its value as a function of temperature [10]. The excitation rate N of free carriers per unit area is determined by the excitation intensity P from the PL measurement:

$$N \approx \frac{Pg(1-R)}{h\upsilon} \tag{5.4}$$

where g is the quantum efficiency (on the order of unity), R is the reflectivity of material (R_{GaN}=0.15), hv is the photon energy of the exciting light (hv=3.81 eV).

The internal electric field F_s as a function of the incident illumination P is calculated from Equation 5.1-5.5, as following:

$$F_s = \left(F_{so}^2 - \frac{F_{so}^2 kT\ln\{[bPg(1-R)/h\upsilon]+1\}}{eV_{so}}\right)^{1/2} \tag{5.5}$$

where F_{s0} is the built-in field under zero illumination intensity. The electric field is assumed to be a constant over the undoped quantum well region. The electric field of the PL emission is originating from quantum wells and modified by the QCSE.

The induced-internal field caused peak shifts in PL spectrum and may calculate by Hamiltonian of perturbation. Let us consider a particle, with charge e and effective mass m^*, in an infinite quantum well of width L in the presence of an electric field F along the direction of the well, z. (In semiconductor heterostructures, this direction is perpendicular to the material layers.) The origins of distance and of electrostatic potential are chosen at the center of the well. The Hamiltonian of the problem is therefore [11] :

$$H = H_0 + |e|F_s z \tag{5.6}$$

where H_o is the zero-field quantum-well Hamiltonian. The spectrum of H_o is discrete and given by:

$$E_n^{(0)} = \frac{\hbar^2\pi^2}{2m^*L^2}n^2 \quad n = 1,2,\ldots. \tag{5.7}$$

For weak fields, such that:

$$|e|FL \ll \frac{\hbar^2\pi^2}{2m^*L^2} \tag{5.8}$$

a second-order perturbation calculation gives for the energy shift of the ground state:

$$\Delta E^{(2)} = -C'\frac{m^*e^2{F_s}^2L^4}{\hbar^2} = -C{F_s}^2 \tag{5.9}$$

with

$$C' = \frac{2^9}{\pi^6}\sum_{p=1}^{\infty}\frac{p^2}{(4p^2-1)^5} = \frac{1}{24\pi^2}\left(\frac{15}{\pi^2}-1\right) \tag{5.10),}$$

Therefore, we can obtain:

$$C = \frac{1}{24\pi^2}\left(\frac{15}{\pi^2}-1\right)\frac{m^*e^2L^4}{\hbar^2} \tag{5.11).}$$

Using Equation 5.7-5.10:

$$E_{PL} = E_0 - C\left(F_{so}^2 - \frac{F_{so}^2 kT ln\{[bPg(1-R)/h\nu]+1\}}{eV_{so}}\right) \tag{5.12}$$

where E_{PL} is the PL emission energy from the QW under illumination, E_0 is the energy of the PL peak assuming zero internal electric field, and F_{s0} is the built in field under zero illumination intensity.

As comparing with (0001) MQWs, the IEF of $\{10\bar{1}1\}$ MQWs is remarkably reduced from 1.7 MV/cm to 0.4 MV/cm which is corresponding to center 3 (512 nm) and the apex of nanorod, as shown in Figure 5-3 (b) and (e). For the bottom of nanorod, the IEF of $\{1\bar{1}00\}$ MQWs is 0.05 MV/cm (Figure 5-3 (c)) which is corresponding to center 1 (418 nm). Whereas for the middle portion of nanorod, the IEF of $\{1\bar{1}00\}$ MQWs is 0.02 MV/cm (Figure 5-3 (d)) which is corresponding to center 4 (528 nm). Center 2 (468 nm) is neglected because of the emission wavelength both from the nonpolar and semipolar planes. These results indicate that the QCSE in $\{10\bar{1}1\}$ and $\{1\bar{1}00\}$ MQWs are suppressed. The integration of sample HT with the indium content, the thickness of wells and barriers, the IEF (F_0), and the multiple peaks fitting wavelength from the PL spectrum for points of A-F on core-shell nanorod is shown in Table 5.1.

5.2 Tunable Color Temperature of White Light Emission by Nano-facets InGaN/GaN MQWs

Colorimetry is the science of the human perception of color, human eyes are hard to distinguish a mixture of two pure colors. A color mixture system of three primary lights with red, green and blue could be quantified by color matching functions that were established by the Commission Internationale de l'Eclairage (CIE) in 1931. Color matching functions of the *RGB* color system were obtained from a series match of the reference tristimulus. Then, a mathematical conversion transformed the *RGB* color system into the *XYZ* color system with dimensionless quantities, known as the CIE 2° Colorimetric System or the CIE 1931 Standard Colorimetric System. Accordingly, the tristimulus *X*, *Y* and *Z* in the CIE 1931 color space were obtained directly from color matching functions $\bar{x}(\lambda)$, $\bar{y}(\lambda)$, and $\bar{z}(\lambda)$, as given in Figure 5-5 and Equation 5.14-5.16:

$$X = \int_{\lambda} \bar{x}(\lambda)\, P(\lambda)\, d\lambda \tag{5.13}$$

$$Y = \int_{\lambda} \bar{y}(\lambda)\, P(\lambda)\, d\lambda \tag{5.14}$$

$$Z = \int_{\lambda} \bar{z}(\lambda)\, P(\lambda)\, d\lambda \tag{5.15}$$

where, X, Y and Z were referring to red, green and blue colors, $P(\lambda)$ was the power intensity of the illuminating light spectrum.

The chromaticity coordinates x, y and z is acquired from the tristimulus in the following Equation 5.17-5.19:

$$x = X/(X+Y+Z) \qquad (5.16),$$

$$y = Y/(X+Y+Z) \qquad (5.17),$$

$$z = Z/(X+Y+Z) = 1 - x - y \qquad (5.18).$$

Because the complementary relation of $x + \mathrm{y} + \mathrm{z} = 1$, the visible spectrum can be described in two dimension x and y coordinates.

As shown in Figure 5-6, the monochromatic lights or the pure colors with dominant wavelengths stand on the periphery of chromaticity diagram. The large values of x and y are red and green color with wavelength at 520 nm and 770 nm, respectively. The large value of z, but the small value of x and y is violet-blue color with wavelength at 380 nm. The discontinuity in purple region has no dominant wavelengths on the lower straight line. White light in the location (x, y) = (1/3, 1/3) is the equal-energy locus at the center of chromaticity diagram.

Sunlight represents white light which has a broad emission spectrum in the visible range. The standardization of white light is quantified by the path of black body locus or the Planckian locus on chromaticity diagram. The Planckian locus is described by absolute temperature (Kelvin), so-called color temperatures (T_c). Along the path, a color changes from red at low temperature through orange, yellow, white to bluish white at high temperature. Supposing that the white light is not under the Planckian locus, correlated color temperature (CCT) is used to describe the narrow distance to T_c [8, 9]. To evaluate the CCT value from the chromaticity coordinates x and y, a mathematical method is used, as given in Equation 5.20 and Table 5-2 [12-14] :

$$CCT = -A_0 + A_1 exp(-n/t_1) - A_2 exp(-n/t_2) + A_3 exp(-n/t_3) \tag{5.19}$$

where,

$$n = (x - x_e)/(y - y_e) \tag{5.20}$$

Given in the above equations, we calculated the CCT, x and y coordinates of the core-shell nanorod samples from the PL spectrum as shown in Figure 5-7 which are listed in Table 5-3. In previous, the polychromatic emission had been realized by an inhomogeneous distribution of indium content and thickness on the different nano-facets InGaN/GaN MQWs of nanorods. As shown in Figure 5-7, the CCT value is about 60,000 K of sample HT which is located on a blue region of the chromaticity diagram. A natural white emission around 6,000 K of sample LT is achievable by a high indium incorporation efficiency at low regrowth temperature of MQWs nano-factets. To sum up, the location of coordinates (x, y) and the CCT value can be tuned by a different regrowth temperature of MQWs nano-facets on nanorods.

5.3 Photoluminescence of 3-D Core-shell InGaN/GaN Multi-Facet Qunatum Wells on Semipolar $\{10\bar{1}1\}$ and Nonpolar $\{10\bar{1}0\}$ Plane

In order to confirm the efficiency, the PL internal quantum efficiency (IQE) measurement was performed. We performed the temperature dependent PL measurement at low temperature and room temperature and define it by observing the tendency of the curves [15]. This could be expressed as the following :

$$\eta_{int} = \frac{\text{number of photons emitted from active region per second}}{\text{number of electrons injected into LED per second}} = C\frac{I_{PL}/E_{PL}}{I_{EX}/E_{EX}} \qquad (5.22)$$

Where I_{PL} and I_{EX} are PL intensity and excitation intensity, respectively. E_{PL} and E_{EX} are PL photo energy and excitation photon energy, respectively. C is a constant affected by mostly carrier injection efficiency by laser, light extraction and correction efficiency of PL, and does not depend on either excitation power density or measurement temperature.

From the theoretical of carrier dynamics, we can assume that the IQE is 100% at low temperature (LT) (about 15K in our experiment). In order to cancel the constant C, we divide the IQE at every temperature by the IQE at LT, consequently, the IQE of the LED at every temperature (T) can be rewrite as:

$$\eta_{int}(T) = \frac{\left(C\frac{I_{PL}/E_{PL}}{I_{EX}/E_{EX}}\right)_T}{\left(C\frac{I_{PL}/E_{PL}}{I_{EX}/E_{EX}}\right)_{LT}} = \frac{I_{PL}(T)}{I_{PL}(LT)} \tag{5.23}$$

The Table 5.4 showed the measurement of the IQE and the activation energy, and binding energy of HT- and LT-sample. For the HT-sample, the IQE of core-shell semipolar $\{10\bar{1}1\}$ Green and nonpolar $\{10\bar{1}0\}$ Blue InGaN/GaN MQWS structure were about 23.92% and 18.86%, respectively. It was found that there is a great enhancement for the suppressing the QCSE and reducing localize state in 3-D core-shell structure. In addition, the IQE of core-shell semipolar $\{10\bar{1}1\}$ Yellow and nonpolar $\{10\bar{1}0\}$ Green InGaN/GaN MQWS structure were 11.12% and 19.86% for LT-sample, respectively. The lower IQE in LT-sample resulted from the lower growth temperature, indicating the poor crystalline quality of InGaN well layer.

And the temperature dependent IQE curve could be fitted by the following equation to get the activation energy:

$$I(T) = \frac{I(0)}{1 + A\, e^{\frac{-E_a}{kT}} + B\, e^{\frac{-E_b}{kT}}} \tag{5.24}$$

Where I(T), I(0) are the integrated PL intensity for T and 0K (the temperature of 15K was used in our experiment), A and B are constants, k is the Boltzmann constant, T is the temperature, E_a is the activation energy for PL quenching, and E_b is generally associated to the free exciton binding energy [16]. 錯誤！找不到參照來源。9 shows the Arrhenius plot for (a) HT-sample and (b) LT-sample, and the fitting curves of activation energy were included. In Table 5.4, the activation energy of core-shell semipolar (10-11) Green and nonpolar $\{10\bar{1}0\}$ Blue InGaN/GaN MQWS structure were 65 meV and 50 meV for HT-sample. In general, the quenching of the luminescence with temperature can be explained by thermal emission of the carriers out of a confining potential with an activation energy correlated with the depth of the confining potential [17]. One could understand it through the schematic of activation energy in 錯誤! 找不到參照來源。8. It is suggested that the localization of carriers operates as excellent radiative recombination centers. In other words, high localization energies of excitions can provide deep potential wells that suppress the diffusion of electrical carriers toward versus non-radiative defects. The carrier localization in the active layer also has a significant effect on the performance of LEDs, resulting in an increase in radiative recombination efficiencies [18]. And the activation energy of core-shell semipolar $\{10\bar{1}1\}$ Yellow and nonpolar $\{10\bar{1}0\}$ Green InGaN/GaN MQWS structure were 45 meV and 68 meV for LT-sample, respectively. The lower activation energy in semipolar $\{10\bar{1}1\}$ facet was attributed to more non-radiative center in higher In layer, resulting in poor confinement in this MQW structure.

In order to further check the degree of carrier localization effect in all samples, we analyzed the peak shift of the InGaN MQWs emission over the investigation temperature range. The TDPL was measured at P = 10 mW (carrier density about 1E16 cm^{-3}). In general, the wavelength redshifts until a temperature of ~100 K corresponding to a maximum of the localization energy, then, it blueshifts up to the full-delocalization temperature of ~200 K, where it starts red shifting again. The anomalous temperature behavior of the peak energy is S-shaped (decrease-increase-decrease) [17, 19-22]. In

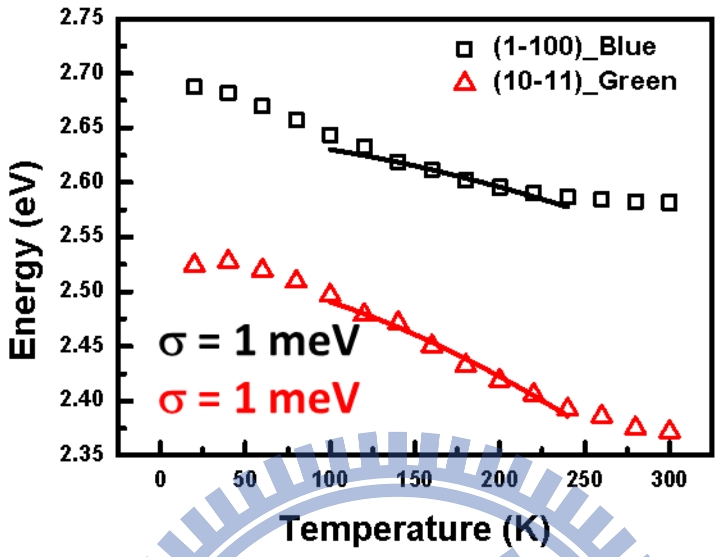

5-10, the anomalous temperature behaviors of two different growth facets, semipolar $\{10\bar{1}1\}$ pyramid and nonpolar $\{10\bar{1}0\}$ sidewall, were clearly observed. For both of the semipolar $\{10\bar{1}1\}$ and nonpolar $\{10\bar{1}0\}$ MQWs, the peak energy monotonically decreases with increasing temperature. It is different from the general red-blue-red shift (S-curve) behavior in the c-plane MQWs, which is caused by the localized tail states as well as the fluctuations in In distribution in InGaN MQWs [17, 23]. The absence of S-curve indicates the significant reduction of localized potentials in the 3-D core-shell MQWs. This could be due to the better strain relaxation provided by the nanostructure and/or the growth property of the pyramidal semipolar facets and vertical nonpolar sidewall [24, 25].

Therefore, the band-tail model should be suitable for discussion of this exciton localization effect. Based on the band-tail model, if Gaussian-like distribution of the density of states for the conduction and valence band is assumed, the temperature-dependent emission energy could be described by the following expression:

$$E(T) = E(0) - \frac{\alpha T^2}{\beta + T} - \frac{\sigma^2}{kT} \tag{5.25}$$

where E(T) is the emission energy at T, E(0) the energy gap at 0 K, and α and β are Varshni's fitting parameters. The third term comes from the localization effect, in which σ indicates the degree of localization effect, i.e., the large value of σ means a strong localization effect, and k is the Boltzmann constant. The fitting is made based on Equation 5.25 in each case, and the fitting experimental data in the temperature range of 120-240 K. The fitting curve are included in the

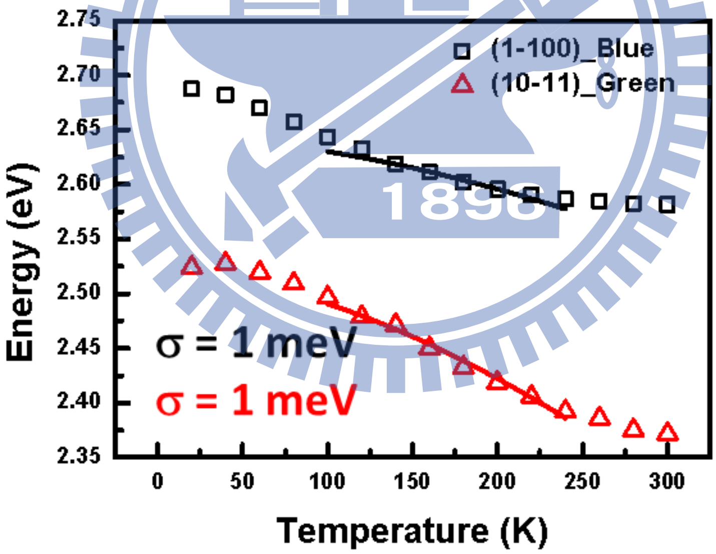

5-10, and fitting parameter σ is 1 meV of semipolar (10-11) green MQWs and 1 meV for the nonpolar $\{10\bar{1}0\}$ MQWs. It is revealed that almost zero localization in 3-D core-shell MQWS structure.

On the other hand, once the wave-function overlap between electron and hole is enhanced, the transition probability of carriers in quantum well, which is associated with radiative recombination lifetime, is expected to be increased. In this section, the radiative recombination lifetime is qualitatively determined by time-resolved photoluminescence (TRPL). TRPL is indispensable technique to study the dynamical process of photoexcited carriers such as relaxation, radiative, nonradiative, and localization processes.The transient luminescence intensity obtained by the data of TRPL is generally fitted by a combined exponential and stretched exponential line shape [26-28]:

$$I(t) = I_1 e^{-\frac{t}{\tau_1}} + I_2 e^{-\left(\frac{t}{\tau_2}\right)^{\beta}} \tag{5.26}$$

where I(t) is the PL intensity a time t, β is the dimensionality of the localized centers [29-31], and τ_1 and τ_2 represent the initial lifetimes of the carriers. Normally, the fast decay term τ_1 is used represent τ_{PL} since the PL intensity is limited by the fast decay component [27].

Moreover, the effective carrier lifetime can be expressed as following equation:

$$\frac{1}{\tau_{PL}} = \frac{1}{\tau_r} + \frac{1}{\tau_{nr}} + \frac{1}{\tau_{trans}} \tag{5.27}$$

Where τ_r, τ_{nr} and τ_{trans} are the radiative recombination lifetime, nonradiative reocombination lifetime, and transfer time toward lower-lying energy levels. If radiative recombination occurs at the bottom of energy levels, the term of the transfer time can be neglected so that the equation is simplified as shown below and as illustrated in 錯誤! 找不到參照來源。5-11:

$$\frac{1}{\tau_{PL}(T)} = \frac{1}{\tau_r(T)} + \frac{1}{\tau_{nr}(T)} \tag{5.28}$$

The relative probability of radiative recombination is given by the radiative probability over the total probability of recombination. Therefore, the internal quantum efficiency (IQE) can be expressed in terms of the radiative and nonradiative lifetimes [21, 22]:

$$\eta_{int}(T) = \frac{\tau_r^{-1}}{\tau_{PL}^{-1}} = \frac{\tau_r^{-1}}{\tau_r^{-1}+\tau_{nr}^{-1}} \tag{5.29}$$

The IQE gives the ratio of the number of light quanta emitted inside the semiconductor to the number of charge quanta undergoing recombination. Note that not all photons emitted internally may escape from the semiconductor due to critical angle and reabsorption mechanisms. By using the above equation, the internal quantum efficiency is determined by the competition between radiative and nonradiative recombination processes. In this material system, the radiative recombination rate is affected by the QCSE and exciton localization effects.

At low temperature (regard as absolute 0K, and it is 15K in our experiment), the carriers have no kinetic energy that the nonradiative probability is equal zero. The Equation 5.28 can be rewrite as:

$$\tau_{PL} = \tau_r \tag{5.30}$$

However, as the temperature increases to higher temperature, both of radiative and nonradiative process have to be taken into account. To separate the τ_{PL} into τ_r and τ_{nr}, using Equation 5.23 and Equation 5.24, we can get the equation like this:

$$\tau_r(T) = \frac{I_{PL}(LT)}{I_{PL}(T)}\tau_{PL}(T) \tag{5.31}$$

And the $\tau_{nr}(T)$ can be calculate from Equation 5.24.

錯誤! 找不到參照來源。5-12 shows the TRPL measurement of the nonpolar $\{10\bar{1}0\}$ blue emission at (a) 15 K, (b) 300K and the semipolar $\{10\bar{1}1\}$ green emission at (c) 15 K, (d) 300K. The faster recombination lifetime of blue emission nonpolar $\{10\bar{1}0\}$ on lifetime is due to the suppressing internal electric field. Two possible mechanisms may respond for the faster recombination rate in nonpolar $\{10\bar{1}0\}$ surface, including the lower In content and no spontaneous polarization filed.

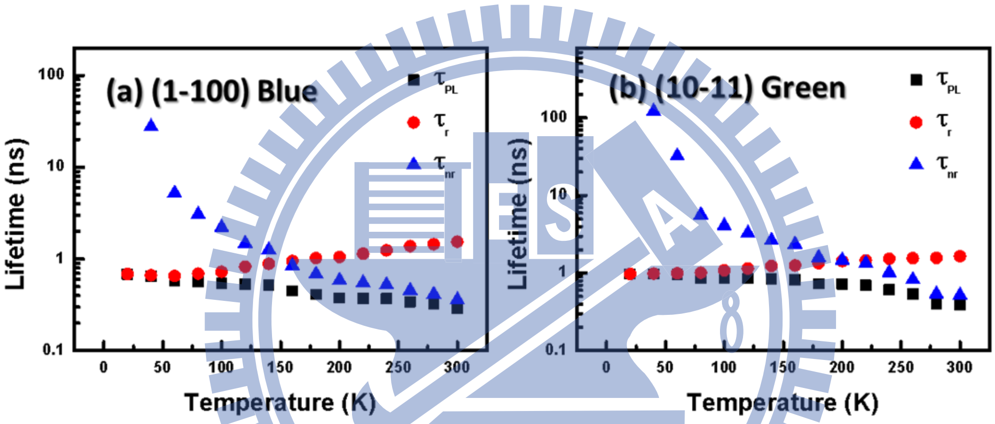

shows the calculated value of PL lifetime (τ_{PL}), radiative lifetime (τ_r) and non-radiative lifetime (τ_{nr}) of each temperature by using the Equation 5.31. Furthermore,

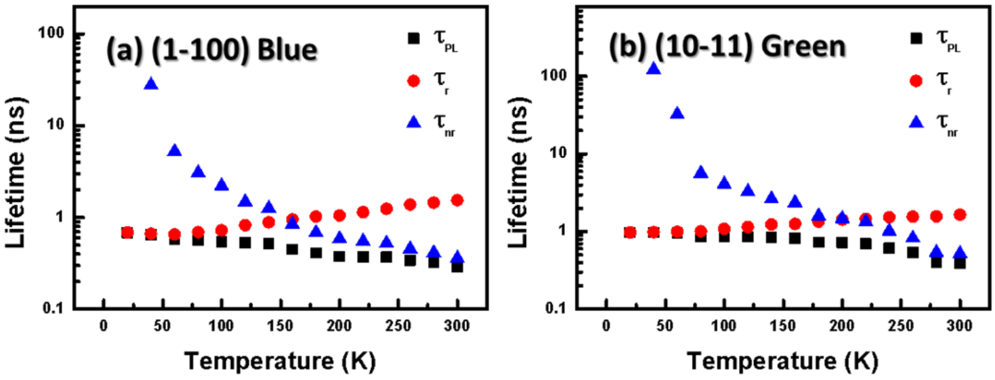

4 revealed that radiative lifetime (τ_r) of both nonpolar $\{10\bar{1}0\}$ blue emission and semipolar $\{10\bar{1}1\}$ green emission, and the fitting curve were included. In the

experiment, the excition radiative lifetime is dependent on the temperature. Meanwhile, it is described from following equation:

$$\tau_r \propto DOS \propto T^{0.0}\ (0D) \tag{5.32}$$

$$\tau_r \propto DOS \propto T^{0.5}\ (1D) \tag{5.33}$$

$$\tau_r \propto DOS \propto T^{1.0}\ (2D) \tag{5.34}$$

$$\tau_r \propto DOS \propto T^{1.5}\ (3D) \tag{5.35}$$

The τ_r remains constant at low temperature below ~50 K as shown in Equation 5.32. This is explained that the radiative lifetime is nearly constant for a localized exciton below 50 K. On the other hand, the τ_r increases linearly above 180 K. This is related to 2D confined exciton [32]. It indicates that, at low temperature, the excitons are trapped in localized potentials due to inhomogeneous In composition in MQWs. As temperature increases, excitons are excited out of the traps and become free excitons in the 2D MQWs, resulting in approximately linearly increasing radiative lifetime. The measured radiative lifetime at room temperature for nonpolar $\{10\bar{1}0\}$ Blue MQWs and semipolar $\{10\bar{1}1\}$ green MQWs are 1.47 ns and 1.79 ns, respectively. These τ_r values are about two orders of magnitude smaller than the typical τ_r on c-plane (0001) MQWs [33]. The faster radiative recombination is the strong evidence to the suppression of polarization field in InGaN/GaN MQWs. However, it is worth noting that the faster τ_r is not directly related to the enhancement of IQE. It is known that τ_{nr} also plays an equally important role in the IQE. The measured τ_{nr} is also significantly shortened as well in the experiment. It is attributed to samller potential localization for MQWs grown on the semipolar facets. The localized potential has been considered as one of the important factors in preventing the capture of excitons by the threading dislocation defects [34, 35]. The suppression of localized potentials will result in the increase of the probability of the capture of excitons by the defects and therefore shorten τ_{nr}. As a result, even though τ_r is shortened by two orders of magnitude, the IQE is not enhanced in a similar magnitude.

5.4 Lasing Action in Gallium Nitride Photonic Quasicrystal Nanorods Arrays

There have been great research interests in gallium nitride material due to its promising applications in UV to blue optoelectronic devices. Conventionally, the devices are built in two-dimensional thin film structure, where emission sources are from the planar quantum wells. Recently, devices with one-dimensional nanostructure have gained substantial attention for their interesting properties and potential applications [36-38]. The one-dimensional structure can be fabricated by top-down patterned etching or bottom-up self assembled growth. The fabricated nanostructures have shown quantum confinement effect and interesting light emission properties [39-41]. Stimulated emission from single free standing lying nano wire and 2-D periodic nanorod arrays have been observed [42,43], where lasing modes are the Fabry-Perot modes of the wire end surfaces or photonic crystal band edge modes. Recently, lasing action due to the feedback from the multiple scatterings of optically pumped disordered nanorods was also reported [44]. This phenomenon is called random lasing [45], which is often analyzed in terms of statistics.

The statistical nature of random lasing is interesting. However, it puts a limitation to device applications due to the lack of control on the lasing modes and frequency locations from sample to sample. Recently, there are great interests in studying photonic quasicrystals, which may look random at first glance yet have well defined patterns. Their optical properties are fascinating and lie somewhere between those of periodic and random structures [46-49]. It therefore may provide a way to design a pseudo random laser with deterministic properties, which could be important for practical applications. Here we report the observation of lasing action from room temperature optically pumped GaN quasicrystal nanorod arrays.

The lasing phenomenon resembles that of a random laser. The quasicrystal nanorod array sample was fabricated from a GaN epitaxial wafer by nano-imprint patterned etch, followed by epitaxial regrowth. The imprint was a 12-fold symmetric quasicrystal pattern [46-49]. The regrowth formed hexagonal facets on the nanorod sidewalls and hexagonal pyramids on the top. The regrowth also grew InGaN/GaN MQWs on the sidewalls and pyramid facets. The use of MQWs allows us to investigate the optical properties of QPC at a designed wavelength. Under optical pumping, multiple lasing peaks were excited. The lasing was identified to be from the MQWs on the nanorod sidewalls. The peak distribution did not show obvious regularity and behaved like a random lasing action. The linewidth of laser peaks was in the range of 0.2-0.3 nm, indicating a strong resonant feedback oscillation. The lasing threshold pump intensity decreases with increasing pump area. The lasing mechanism is attributed to the feedback of close loop multiple scatterings among nanorods.

Here we report the observation of lasing action form room temperature optically pumped GaN nanorod arrays in a quasicrystal pattern. The imprint patterned etching created nanorod arrays in a 12-fold symmetric quasicrystal pattern. The epitaxial regrowth formed $\{10\bar{1}0\}$ *m*-plane facets on nanorod sidewalls and $\{10\bar{1}1\}$ *s*-plane hexagonal pyramid on the top. Sample HT with the smooth sidewall surfaces was optically excited by a 355 nm tripled Nd:YAG pulse laser at room temperature. The pulse width was 0.5 ns and the pulse repetition rate was 1 KHz. The laser beam was focused on the sample surface in normal incident by a 15X UV microscope objective. The pump spot at sample surface had a Gaussian intensity profile with $1/e^2$ diameter of 37 μm, verified by a knife edge measurement. The photoluminescent (PL) spectrum was collected by the same UV objective and coupled into an optical fiber connected to the input of a spectrometer with nitrogen cooled CCD array. The PL spectra of sample HT at various pump power intensities are shown in the inset of Figure 5-15 (a), where the legends are pump intensity levels. As pump intensity increases, narrow emission peaks with linewidth in the range of 0.2-0.3 nm emerge from the broad emission background. The integrated power within the spectral range of these emission peaks versus pump intensity is shown in Figure 5-15 (a), which indicates an onset of lasing action at threshold pump intensity of ~5 MW/cm^2. These emission peaks span from 450 to 470 nm, which corresponds to emission from the quantum wells located from middle to upper part of the nanorod columns as shown by CL images Figure 5.2 (b). The spacings among these lasing peaks do not show obvious regularity. It implies that the lasing modes are unlikely due to whispering gallery modes of individual nanorod. Not all lasing peaks always increase with the increase of pump power. Some of the peaks can decrease due to the increase of other emerging peaks, which indicates that there are lasing mode competitions. Given the rather irregular lasing peaks, what we have observed here is likely a random lasing action. In addition, no lasing action is observed in sample LT because the degraded sidewall surfaces with the low regrowth temperature of MQWs [45, 50].

A random laser is a lasing action in a disordered active media due the existence of scattering loops where the round trip losses are compensated by gain. The scattering loop serves as the function of optical feedback as the conventional laser cavity. There could also be multiple scattering loops returning to one starting point or overlapping, which can be viewed as randomly distributed feedback. The nanorods in our sample play the roles of scattering sites and providing gain. The lack of short range order of the quasicrystal pattern and the hexagonal nanorod facets together make the sample HT pseudodisordered media. One of the random laser characteristic is the lasing threshold pump intensity decreases with increasing pump spot area in a power law relation [45, 50, 51]. The reason in a simplified picture is because there are more multiple recurrent scattering loops that can create tighter confined modes in a larger gain area, which leads to a lower threshold pump intensity. We have measured the threshold pump intensity versus pump spot size. The experimental data points are shown in Figure 5-15 (b), along with a power law fitting function. The power law function fits well to the experimental data and gives a threshold pump intensity $I_{th} \sim 1/A^{0.27}$ dependence.

We investigated the resonant modes of this pseudo random lasing by performing twodimensional (2D) finite difference time domain (FDTD) simulation. The 2D model was chosen for simplicity and believed to be a reasonable approximation because the gain was predominantly distributed in 2D direction perpendicular to nanorod axis. The lasing mode field would therefore mainly follow the gain in the 2D direction. The finite nanorod length in the vertical direction will certainly modify the mode frequency and profile, but we consider it as a secondary effect. The simplified model is meant to explain qualitatively the observed lasing behavior. Figure 5-16 (a) shows the quasicrystal model used for simulation. The nanorod and quasicrystal pattern dimensions measured from SEM image were used to construct the model. The overall pattern size is about 16 μm across. The finite pattern size was used due to the limit of computation power and time. An optical pulse with a center wavelength at 470 nm and a linewidth of 30 nm was launched at a randomly chosen location near nanorod sidewall to simulate the emission from MQWs. The pulse spectral width was chosen according to the observed lasing spectral range. Both transverse electric and magnetic field were calculated. After a long enough propagation time, the shape of spectrum became steady. The spectrum contained distinct resonant peaks, which were the resonant modes excited by the broad-band pulse. The same calculation was repeated for different pulse launching locations. The quality factors of these modes are in the range of 500. The spectrum varied from location to location and had many or just a few resonant peaks. All these resonant peaks can be regarded as the potential lasing modes. For illustration purpose, three spectra were shown in Figure 5-16 (b)-(d). The corresponding launching locations are the points labeled (b), (c), and (d) in Figure 5-16 (a). Points (b) and (c) are deliberately at locations away from center. Point (d) is at the center rod.

The calculated resonant spectra show irregular peak locations, similar to what was observed in the experiment. The calculated resonant peaks do not match to the observed spectrum in peak to peak locations. This can be attributed to the fact that the model used in simulation is an overly simplified approximation. The lasing peaks should be ideally deterministic and can be engineered by design since the QPC pattern is deterministic. This could be important in practical applications. We then calculated the resonant mode profiles. It was calculated by choosing one of the peaks in the resonant spectrum and launching it at the same location. After propagating for a reasonable long time, a distinctive pattern was developed. We regarded it as the mode profile of the specific peak. Ideally, one can repeat the calculation for all the peaks to obtain all the mode profiles. We have calculated a few of them. The mode profiles could be rather irregular or have certain distinctive feature. For illustration purpose, the mode profiles of the resonant peaks labeled Figure 5-17 (a) and (b) in Figure 5-16 (b), and (c). Figure 5-16 (c) are shown in Figure 5-17 (a)-(c), respectively. The mode field in Figure 5-17 (a) shows that certain part of nanorods can couple together to provide guiding effect and form various propagation loops. Figure 5-17 (b) on the other hand shows a more scattering like coupling pattern. Figure 5-17 (c) is the field pattern for a source launched at the center rod. The mode field propagates outward and forms triangular shape resonant loops. These patterns show that the intricate property of quasicrystal structure has varieties of mode field patterns, which require a further investigation.

5.5 Summary

We have successfully fabricated core-shell MQW nanopillar arrays by patterned top-down etching and a subsequent epitaxial regrowth. The regrowth results in crystalline hexagonal pyramid nanopillars with $\{10\bar{1}0\}$ nonpolar sidewalls and $\{10\bar{1}1\}$ semipolar pyramid facets. The MQWs grown on these facets have large location dependent InN fraction variations. The emission has a broad spectrum covering from 420 to 520nm. The PL spectrum remains fairly stable over two orders of carrier density change due to the low polarization field of nonpolar and semipolar facets. The broad emission linewidth and low polarization field make the coreshell MQW pillar structure an attractive design for LED lighting applications.

In short, we have observed a red shift as the location moves from the bottom to top portion of nanorods from the spatially resolved CL images. According to the APSYS modeling wavelength, CL images, the multiple peaks fitting from the PL spectrum, the internal electron field and its related indium content can be assigned to the location of core-shell nanorods. Furthermore, the IEF is found to be remarkably reduced by changing the growth planes from (0001) plane to $\{10\bar{1}1\}$ and $\{1\bar{1}00\}$ plane. Color temperature ~60,000 of sample HT is situated on the blue region of the CIE 1931 chromaticity diagram, whereas color temperature ~6,000 (a natural white light) of sample LT is situated on the white region. The tunable color temeprature is attainable by core-shell nanorods grew under a different regrowth temperature of MQWs.

From investigation of TDPL result, the IQEs of the green and blue color MQWs of HT-sample are 23.92% and 18.86%, respectively. The increasing of IQE due to the reducing the degree of localization, strain relax and suppressing the QCSE. In addition, the IQEs of the yellow and Green color MQWs of LT-sample are 11.12% and 19.86%, respectively. In addition, the time-resolved photoluminescence (TRPL) measurement shows a much faster radiative recombination rate in 3-D core-shell semipolar (1-101) green and nonpolar (10-10) blue MQWs, indicating a lower polarization field. The peak emission energies of these samples monotonically decrease with increasing temperature without the typical red-blue-red shift observed in c-plane MQWs. This implies that there is no significant localized potentials due to inhomogeneous In distribution in MQWs grown on the 3-D core-shell MQWs facets [15-19]. The τ_r of remains constant at low temperature below ~50 K, indicating the excitons are trapped in localized potentials due to inhomogeneous In composition in MQWs at low temperature. Above 180 K, τ_r increases linearly as rising temperature. It is implied that thermal activated excitons are excited out of the traps and become free excitons in the 2D MQWs, resulting in approximately linearly increasing radiative lifetime with temperature.

Further, the lasing action is observed in optically pump crystalline Core-shell InGaN/GaN MQWs nanorod arrays arranged in a 12-fold symmetric quasicrystal pattern. Under optical pumping, multiple lasing peaks emerged from broad emission background. The sample was fabricated from a GaN epitaxial substrate by nano patterned etching and epitaxial regrowth. The regrowth grew core-shell MQWs and crystalline facets on nanorods. Under optical pumping, multiple lasing peaks emerged from broad emission background. The irregular multiple lasing wavelengths and the inverse dependence of threshold pump intensity on pump spot area resembles the characteristics of random lasing. The irregularity of resonant peaks is qualitatively explained by a simplified FDTD simulation.

5.6 References

[1] S. Nakamura, *et al.*, The Blue Laser Diode: Springer, Berlin, 2000.

[2] S. Nakamura, *et al.*, "InGaN-based multi-quantum-well-structure laser diodes," *Jpn. J. Appl. Phys.*, vol. **35**, pp. L74–L76, 1996.

[3] T. Mukai, *et al.*, "Amber InGaN-based light-emitting diodes operable at high ambient temperatures," *Jpn. J. Appl. Phys.*, vol. **37**, pp. L479–L481, 1998.

[4] S. Chichibu, *et al.*, "Exciton localization in InGaN quantum well devices," *J. Vac. Sci. Technol. B*, vol. **16**, pp. 2204–2214, 1998.

[5] G. Sun, *et al.*, "Investigation of fast and slow decays in InGaN/GaN quantum wells," *Appl. Phys. Lett.*, vol. **99**, p. 081104, 2011.

[6] Y. Yamane,, *et al.*, "Largely variable electroluminescence efficiency with current and temperature in a blue InGaN multiple-quantum-well diode," *Appl. Phys. Lett.* vol. **91**, p. 073501, 2007.

[7] T. Kanata-Kito, *et al.*, "Photoreflectance characterization of built-in potential in MBE-produced As-grown GaAs surface," *Proc SPIE*, vol. **56**, p. 1286, 1990.

[8] S. M. Sze and K. K. Ng, Physics of semiconductor devices, 3rd Edition:

Wiley-Blackwell, p. 722 ,2007.

[9] A. Chtanov, *et al.*, "Excitation-intensity-dependent photoluminescence in semiconductor quantum wells due to internal electric fields," *Physical Review B*, vol. **53**, p. 4704, 1996.

[10] X. Yin, *et al.*, "Photoreflectance study of the surface Fermi level at (001) n and p type GaAs surfaces," *Journal of Vacuum Science & Technology A*: Vacuum, Surfaces, and Films, vol. **10**, pp. 131-136, 1992.

[11] G. Bastard, *et al.*, "Variational calculations on a quantum well in an electric field," *Physical Review B*, vol. **28**, p. 3241, 1983.

[12] E. F. Schubert, *Light-emitting diodes*: Cambridge Univ Pr, 2006.

[13] N. Ohta, *et al.*, *Colorimetry: fundamentals and applications*: Wiley, 2005.

[14] J. Hernandez-Andres, *et al.*, "Calculating correlated color temperatures across the entire gamut of daylight and skylight chromaticities," *Applied optics*, vol. **38**, pp. 5703-5709, 1999.

[15] S. Watanabe, *et al.*, "Internal quantum efficiency of highly-efficient InxGa1-xN-based near-ultraviolet light-emitting diodes," *Appl. Phys. Lett.*, vol. **83**, p. 4906, 2003.

[16] C. C. Yu, *et al.*, "Electrical and optical properties of beryllium-implanted Mg-doped GaN," *J. Appl. Phys.*, vol. **92**, p. 1881, 2002.

[17] Y. H. Cho, *et al.*, "S-shaped" temperature-dependent emission shift and carrier dynamics in InGaN/GaN multiple quantum wells," *App. phys. lett.*, vol. **73**, pp. 1370–1372, 1998.

[18] C. A. Tran, *et al.*, "Phase separation in InGaN/GaN multiple quantum wells and its relation to brightness of blue and green LEDs," *Journal of crystal growth*, vol. **195**, p. 397, 1998.

[19] H. P. D. Schenk, *et al.*, "Luminescence and absorption in InGaN epitaxial layers and the van Roosbroeck–Shockley relation," *J. Appl. Phys.*, vol. **88**, p. 1525, 2000.

[20] A. Bell, S. Srinivasan, *et al.*, "Exciton freeze-out and thermally activated relaxation at local potential fluctuations in thick AlxGa1-xN layers," *J. Appl. Phys.*, vol. **95**, p. 4670, 2004.

[21] Y. Narukawa, *et al.*, "Radiative and nonradiative recombination processes in ultraviolet light-emitting diode composed of an In0.02Ga0.98N active layer," *Appl. Phys. Lett.*, vol. **74**, p. 558, 1999.

[22] T. Li, *et al.*, "Carrier localization and nonradiative recombination in yellow emitting InGaN quantum wells," *Appl. Phys. Lett.*, vol. 96, p. 013906, 2010.

[23] P. G. Eliseev, *et al.*, "Blue temperature-induced shift and band-tail emission in InGaN-based light sources," *Appl. Phys. Lett.*, vol. **71**, p. 569, 1997.

[24] T. Kim, *et al.*, "Highly efficient yellow photoluminescence from {11–22} InGaN multiquantum-well grown on nanoscale pyramid structure," *Appl. Phys. Lett.*, vol. **97**, p. 241111, 2010.

[25] H. Yu, *et al.*, "Photoluminescence study of semipolar {10-11} InGaN/GaN multiple quantum wells grown by selective area epitaxy," *Applied Physics Letters*, vol. **90**, p. 141906, 2007.

[26] S. F. Chichibu, *et al.*, “Recombination dynamics of localized excitons in cubic InxGa1-xN/GaN multiple quantum wells grown by radio frequency molecular beam epitaxy on 3C–SiC substrate,” *J. Vac. Sci. Technol. B*, vol. **21**, pp. 1856-1862, 2003.

[27] R. Metzler and J. Klafter, “From stretched exponential to inverse power-law: fractional dynamics, Cole–Cole relaxation processes, and beyond,” *Journal of Non-Crystalline Solids*, vol. **305**, pp. 81-87, 2002.

[28] T. Wunderer, *et al.*, “Time-and locally resolved photoluminescence of semipolar GaInN/GaN facet light emitting diodes,” *Appl. Phys. Lett.*, vol. **90**, p. 171123, 2007.

[29] M. Zhang, *et al.*, “Polarization effects in self-organized InGaN/GaN quantum dots grown by RF-plasma-assisted molecular beam epitaxy,” *J. Cryst. Growth*, vol. **311**, pp. 2069–2072, 2009.

[30] Y. J. Sun, *et al.*, “Nonpolar InxGa1-xN/GaN(11¯00) multiple quantum wells grown on γ-LiAlO2(100) by plasma-assisted molecular-beam epitaxy,” *Phys. Rev.* B, vol. **67**, p. 041306R, 2003.

[31] T. Onuma, *et al.*, “Localized exciton dynamics in nonpolar (11math0) InxGa1−xN multiple quantum wells grown on GaN templates prepared by lateral epitaxial overgrowth,” *Appl. Phys. Lett.*, vol. **86**, p. 151918, 2005.

[32] Y. Narukawa, *et al.*, “Dimensionality of excitons in laser-diode structures composed of InxGa1-xN multiple quantum wells,” *Phys. Rev. B*, vol. **59**, p. 10283, 1999.

[33] S.-P. Chang, *et al.*, “Electrically driven nanopyramid green light emitting diode,” *Appl. Phys. Lett.*, vol. **100**, p. 061106, 2012.

[34] N. K. van der Laak, *et al.*, “Role of gross well-width fluctuations in bright, green-emitting single InGaN/GaN quantum well structures,” *Appl. Phys. Lett.*, vol. **90**, p. 121911, 2007.

[35] A. Hangleiter, *et al.*, “Suppression of nonradiative recombination by V-shaped pits in GaInN/GaN quantum wells produces a large increase in the light emission efficiency,” *Phys. Rev. Lett.*, vol. **95**, p. 127402, 2005.

[36] F. Qian, *et al.*, “Core/Multishell nanowire heterostructures as multicolor, high-efficiency light-emitting diodes,” *Nano Lett.*, vol. **5**, pp. 2287–2291, 2005.

[37] R. Chen, *et al.*, “Optically pumped ultraviolet lasing from nitride nanopillars at room temperature,” *Appl. Phys. Lett.*, vol. **96**, p. 241101, 2010.

[38] H. Sekiguchi, *et al.*, "Emission color control from blue to red with nanocolumn diameter of InGaN/GaN nanocolumn arrays grown on same substrate," *Applied Physics Letters*, vol. **96**, p. 231104, 2010.

[39] H. Sekiguchi, *et al.*, “Structural and optical properties of GaN nanocolumns grown on (0001) sapphire substrates by rf-plasma-assisted molecular-beam epitaxy,” *J. Cryst. Growth*, vol. **300**, pp. 259–262, 2007.

[40] Y. Sun, *et al.*, “High efficiency and brightness of blue light emission from dislocation-free InGaN/GaN quantum well nanorod arrays,” *Appl. Phys. Lett.*, vol. **87**, p. 093115, 2005.

[41] Y. Kawakami, *et al.*, “Origin of high oscillator strength in green-emitting InGaN/GaN nanocolumns,” *Appl. Phys. Lett.*, vol. 89, p. 163124, 2006.

[42] S. Gradečak, *et al.*, “GaN nanowire lasers with low lasing thresholds,” *Appl. Phys. Lett.*, vol. **87**, p. 173111, 2005.

[43] T. Kouno, *et al.*, “Two-dimensional light confinement in periodic InGaN/GaN nanocolumn arrays and optically pumped blue stimulated emission,” *Opt. Express*, vol. **17**, pp. 20440–20447, 2009.

[44] M. Sakai, *et al.*, “Random laser action in GaN nanocolumns,” *Appl. Phys. Lett.*, vol. **97**, p. 151109, 2010.

[45] H. Cao, “Review on latest developments in random lasers with coherent feedback,” *J. Phys. A*, vol. **38**, pp. 10497–10535, 2005.

[46] Y. Lai, *et al.*, “Anomalous properties of the band-edge states in large twodimensional photonic quasicrystals,” *Phys. Rev. B*, vol. **76**, p. 165132, 2007.

[47] M. E. Zoorob, *et al.*, “Complete photonic bandgaps in 12-fold symmetric quasicrystals,” *Nature*, vol. **404**, pp. 740–743, 2000.

[48] L. Mahler, *et al.*, “Quasi-periodic distributed feedback laser,” *Nat. Photonics*, vol. **4**, pp. 165–169, 2010.

[49] K. Nozaki and T. Baba, “Lasing Characteristics of 12-Fold Symmetric Quasi-periodic Photonic Crystal Slab Nanolasers,” *Jpn. J. Appl. Phys.*, vol. **45**, pp. 6087–6090, 2006.

[50] A. L. Burin, *et al.*, “Understanding and control of random lasing,” *Physica B*, vol. **338**, pp. 212–214, 2003.

[51] Y. Ling, *et al.*, “Investigation of random lasers with resonant feedback,” *Phys. Rev. A*, vol. **64**, pp. 063808–063815, 2001.

Table 5-1. The integration of sample HT with the indium content, the thickness of wells and barriers, the IEF (F_0), and the multiple peaks fitting wavelength from the PL spectrum.

	In (%)	Well/Barrier (nm)	F_0 (MV/cm)	PL (nm)	CL (nm)	APSYS (nm)
A	**19.8**	**5.5/14.4**	**0.4**	**511**	**N/A**	**507**
B	**16.4**	**3.4/14.1**	**N/A**	**468**	**460**	**460**
C	**25**	**3.5/16.5**	**0.02**	**527**	**520**	**520**
D	**14.6**	**2.7/6.0**	**0.05**	**418**	**420**	**460**
E	**11.6**	**2.7/6.0**	**0.05**	**418**	**420**	**415**
F	**30**	**5.3/15.0**	**N/A**	**N/A**	**N/A**	**N/A**

Table 5-2. CIE 1931 Colorimetric Epicenters x_e, y_e and Constants for Equation 5.20.

Constants	Valid CCT Range (K)	
	3000–50,000	50,000–8 x 10^5
x_e	0.3366	0.3356
y_e	0.1735	0.1691
A_0	2949.86315	36284.48953
A_1	6253.80338	0.00228
t_1	0.92159	0.07861
A_2	28.70599	5.4535 x 10^{36}
t_2	0.20039	0.01543
A_3	0.00004	**N/A**
t_3	0.07125	**N/A**

Table 5-3. The x, y, z, n and CCT of sample HT and sample LT were obtained from Equation 5.17-5.21.

	x	y	z	n	CCT (K)
Sample HT	0.149213	0.206843	0.643944	-8.686	625050.97
Sample LT	0.297198	0.412882	0.28992	-0.1533	6650.45367

Table 5-4. IQE, activation energy and binding energy for HT- sample.

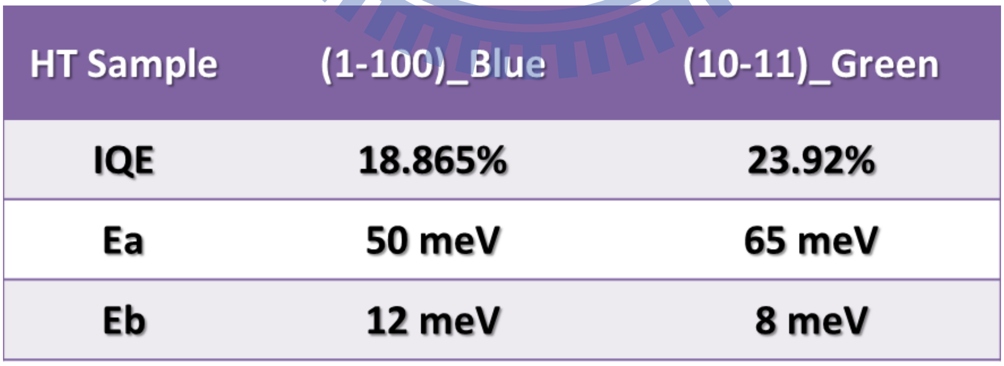

HT Sample	(1-100)_Blue	(10-11)_Green
IQE	18.865%	23.92%
Ea	50 meV	65 meV
Eb	12 meV	8 meV

Table 5-5. IQE, activation energy and binding energy for LT-sample.

LT Sample	(1-100)_Green	(10-11)_Yellow
IQE	19.86%	11.12%
Ea	68 meV	45 meV
Eb	7.36 meV	7.62 meV

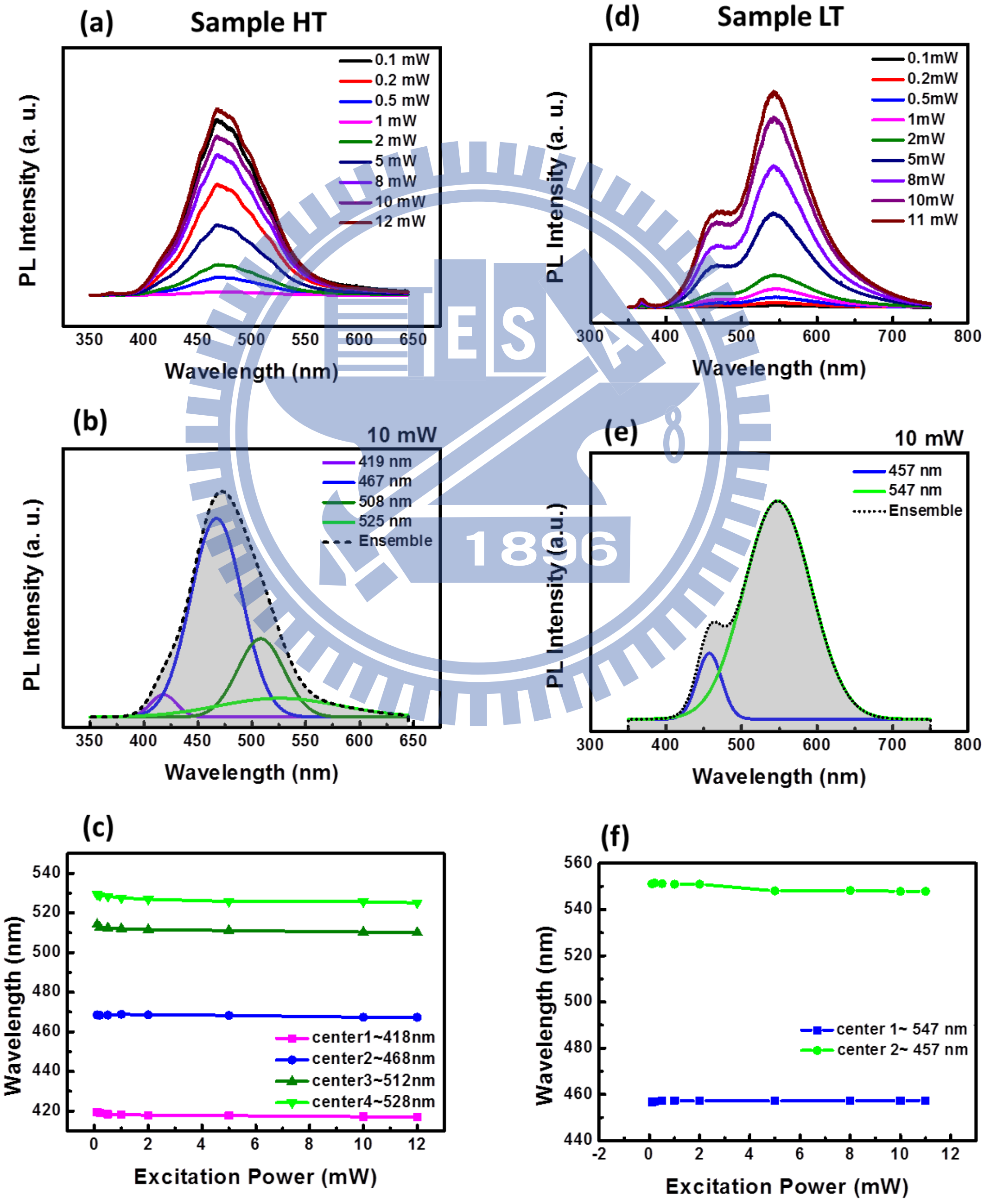

Figure 5-1. The PL spectra as a function of the excitation power for (a) sample HT and (d) sample LT. Multiple peaks fitting of MQWs emission ranging from blue to green with the ensemble PL spectrum of (b) sample HT and (e) sample LT. The emission wavelength as the function of the pumping power of (c) sample HT and (f) sample LT.

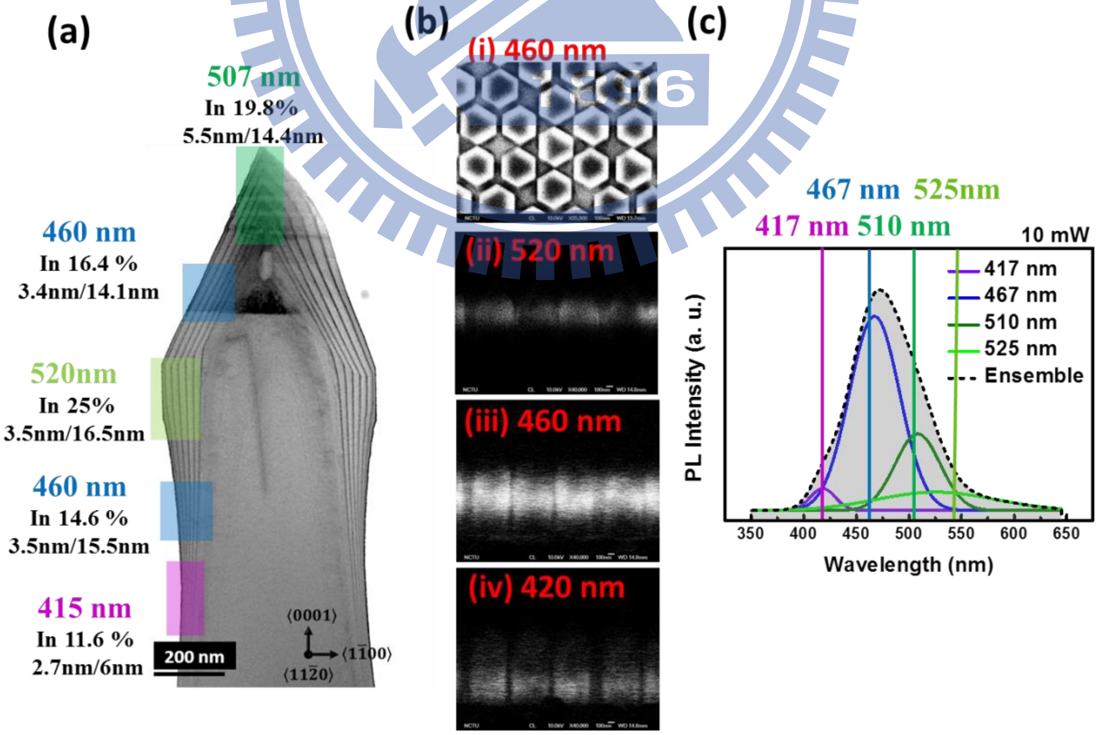

Figure 5-2. (a) Computed wavelength of sample HT by APSYS. (b) The corresponding

position and wavelength of the spatially resolved CL image. (c) Multiple peaks fitting of MQWs emission from the ensemble PL spectrum of the excitation power at 10 mW.

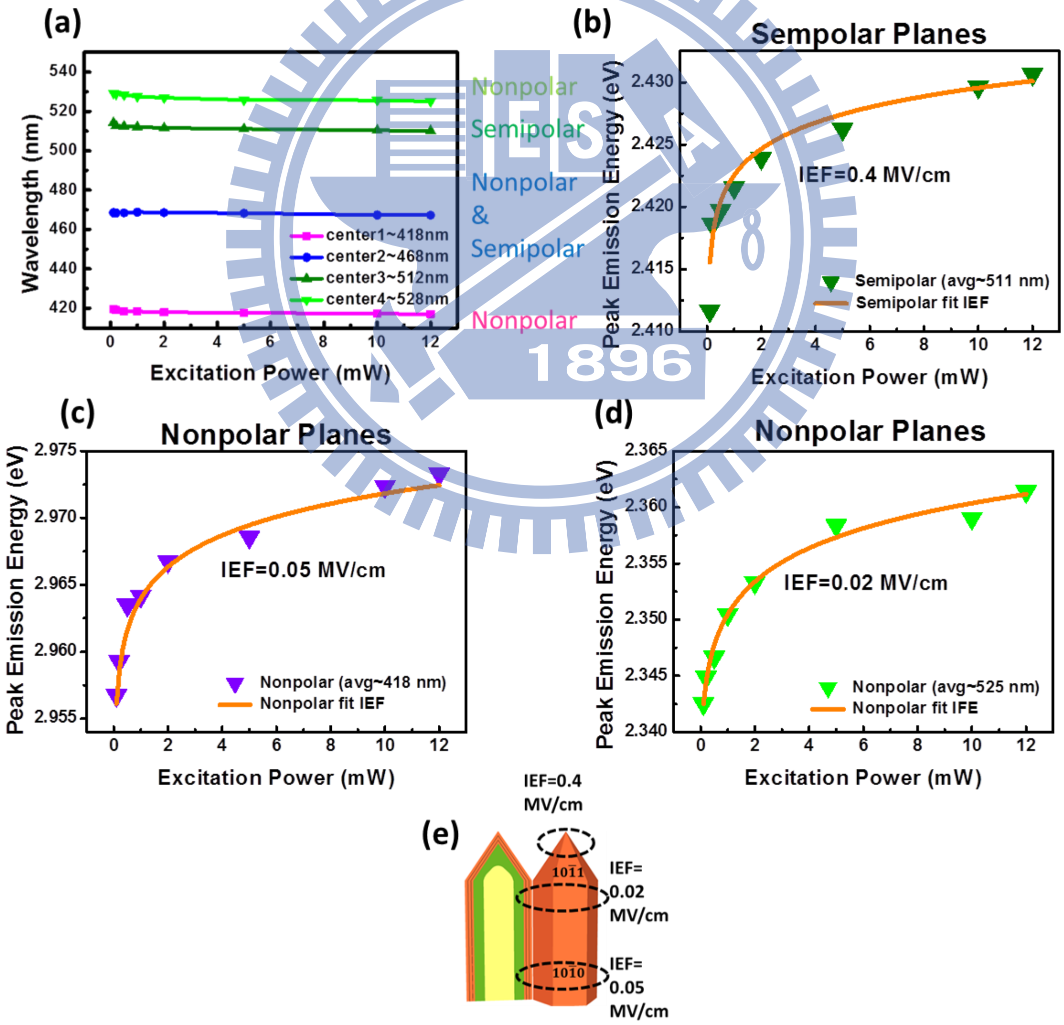

Figure 5-3. (a) The emission wavelength as the function of the pumping power of

sample HT. The PL peak emission energy as the function of the excitation power for with different excitation power for (b) semipolar planes and (c)-(d) nonpolar planes at room temperature. The dots are the experimental value from the PL measurement at room temperature, whereas the solid lines are the fitting results for the IEF. (e) The IEF corresponds to the position of core-shell nanorod.

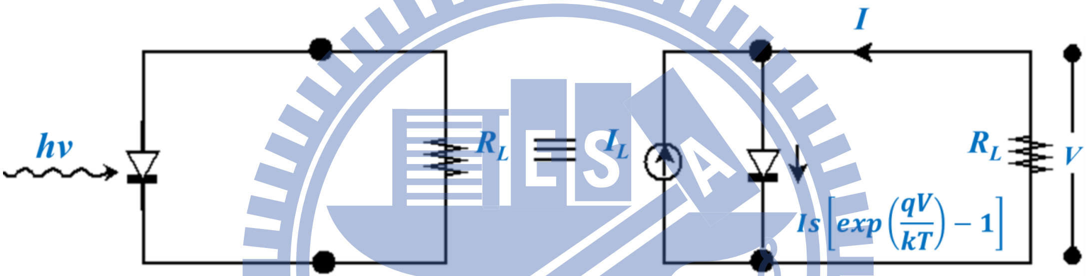

Figure 5-4. The idealized equivalent circuit of p-n junction under illumination [3].

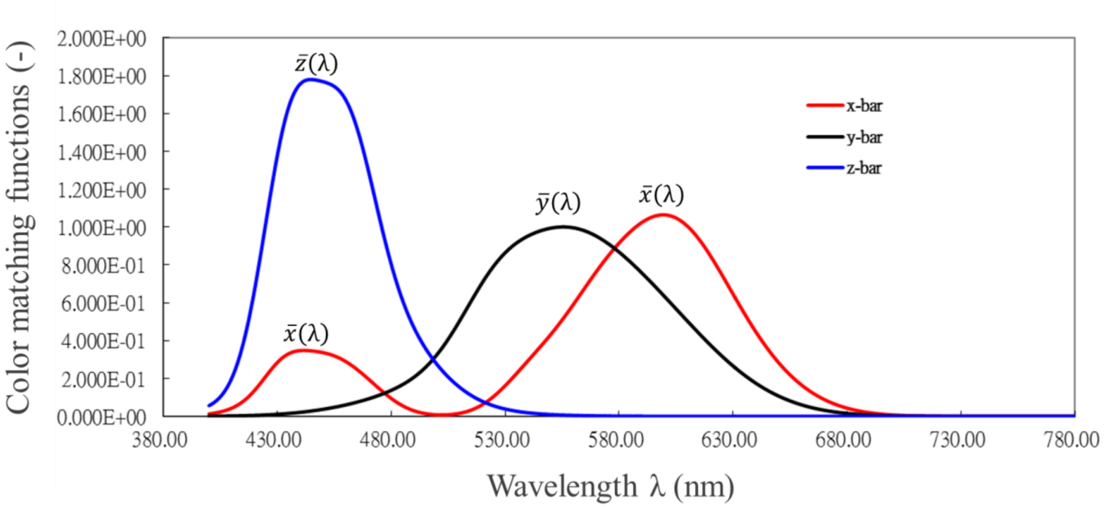

Figure 5-5. Color matching functions were established by CIE in 1931.

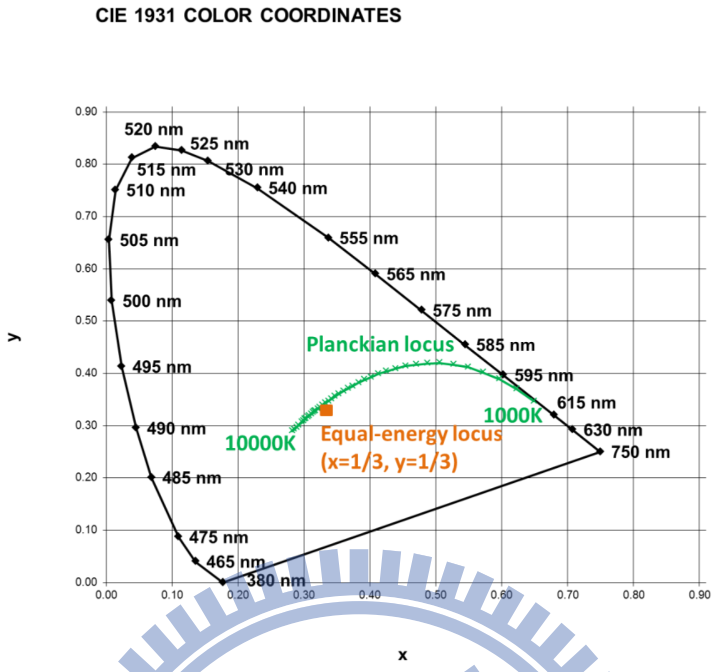

Figure 5-6. CIE 1931 chromaticity diagram with coordinates (x, y).

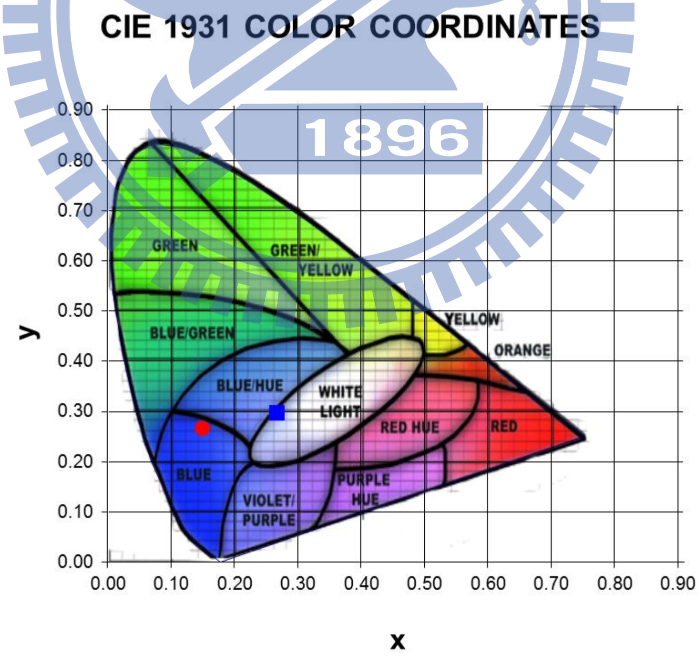

Figure 5-7. Red circle and blue square represent HT and LT sample on CIE 1931 chromaticity diagram, respectively..

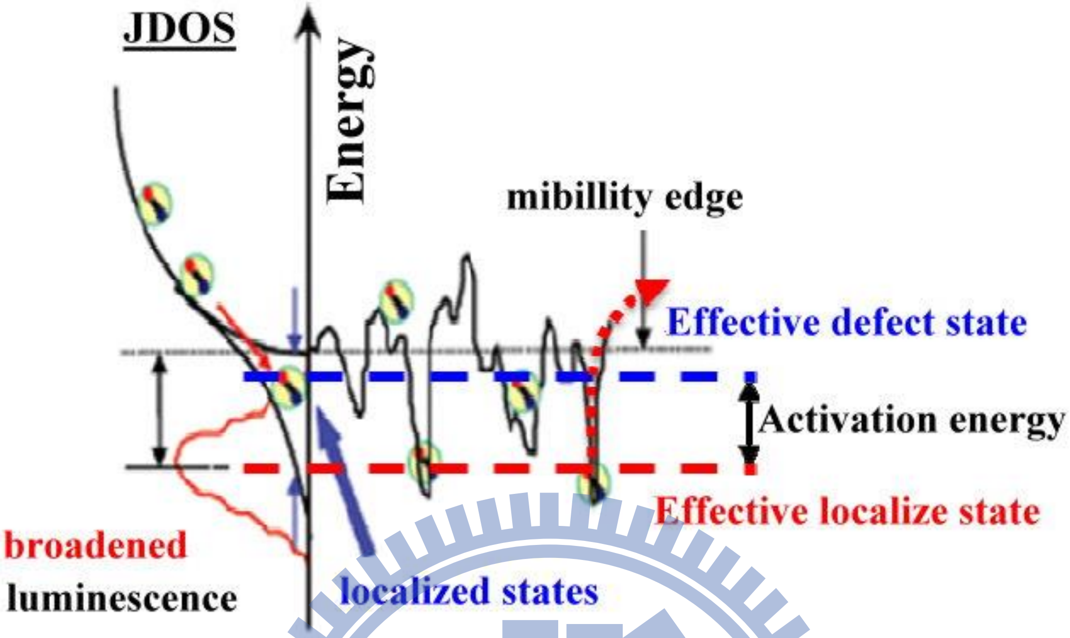

Figure 5-8. Schematic of effective localized states, defect states and activation energy.

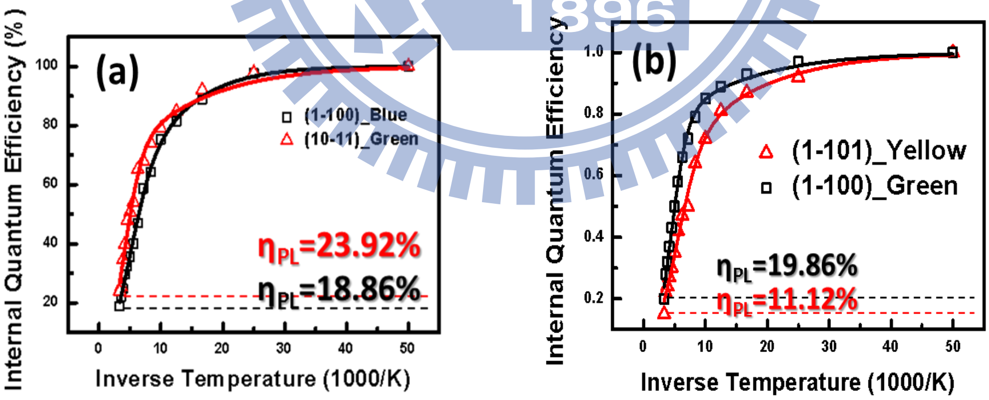

Figure 5-9. Activation energy fitting for (a) HT-sample and (b) LT-sample.

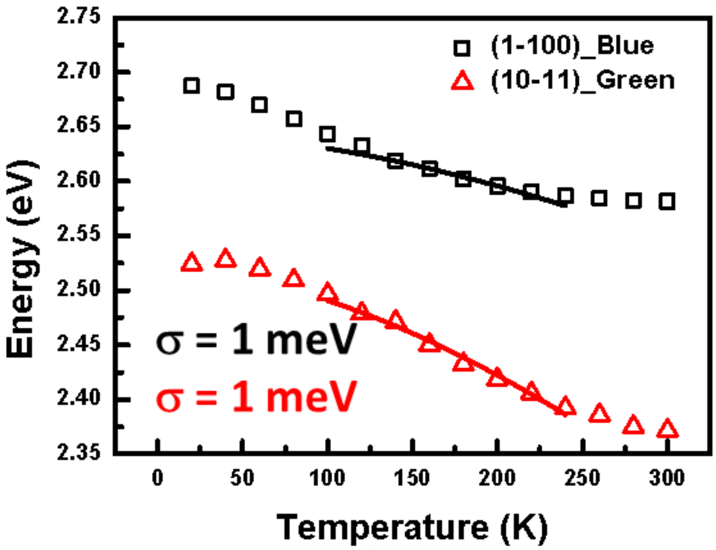

Figure 5-10. Emission energy versus temperature and the fitting of Varshni’s equation for HT-sample.

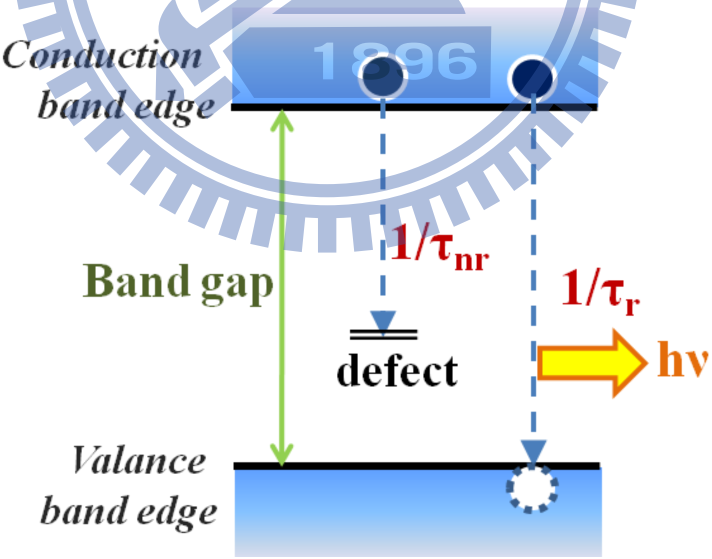

Figure 5-11. Illustration of radiative and nonradiative transition in a semiconductor.

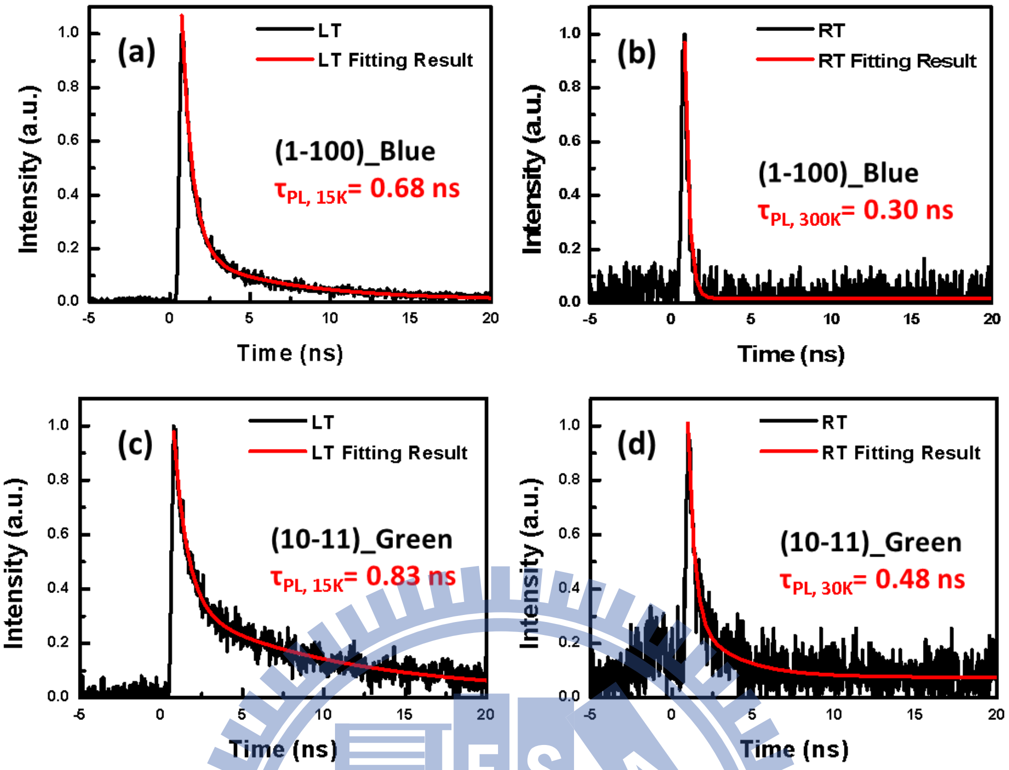

Figure 5-12. TRPL measurement of the nonpolar (10-10) blue emission at (a) 15 K, (b) 300K and the semipolar (10-11) green emission at (c) 15 K, (d) 300K.

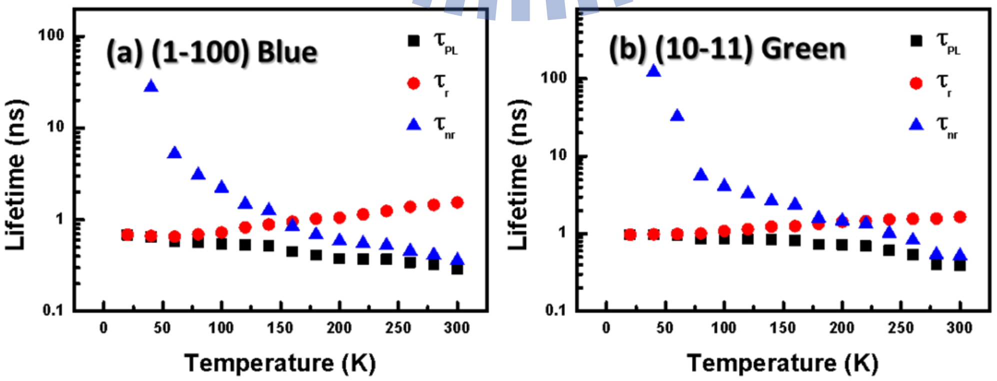

Figure 5-13. τ_{PL}, τ_r and τ_{nr} versus temperature of (a) the nonpolar (10-10) blue emission and (b) the semipolar (10-11) green emission

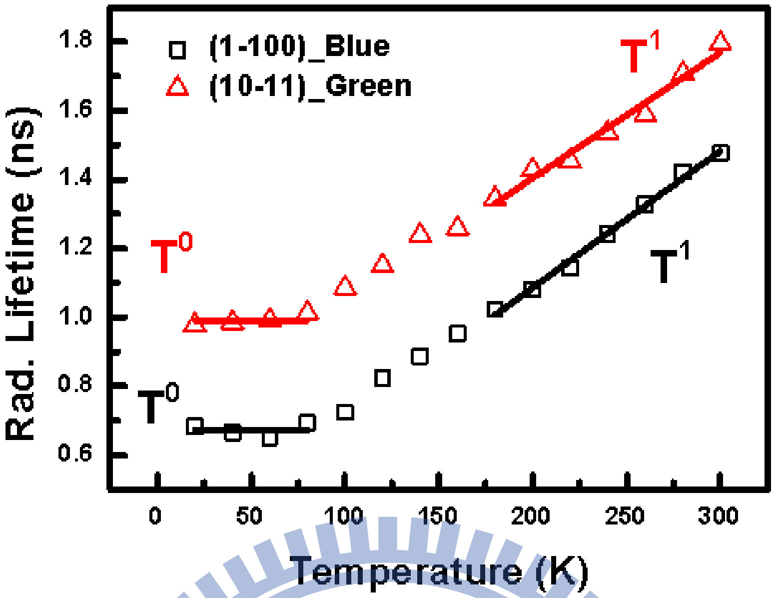

Figure 5-14. Radiative lifetime (τ_r) and the fitting curve for dimensional of excition of both nonpolar (10-10) blue emission and semipolar (10-11) green emission.

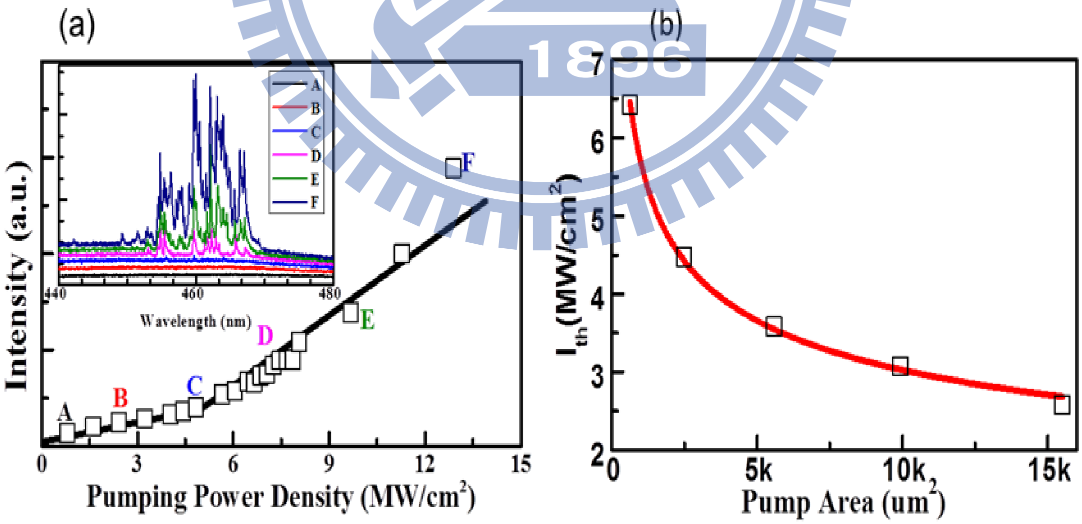

Figure 5-15. (a) Integrated emission power versus pump intensity, showing the onset of lasing action. Inset graph shows the emission spectrum versus pump intensity. (b) Threshold pump intensity versus pump spot area and the power law fitting curve showing a threshold pump intensity $P_{th} \sim 1/A^{0.27}$ dependence.

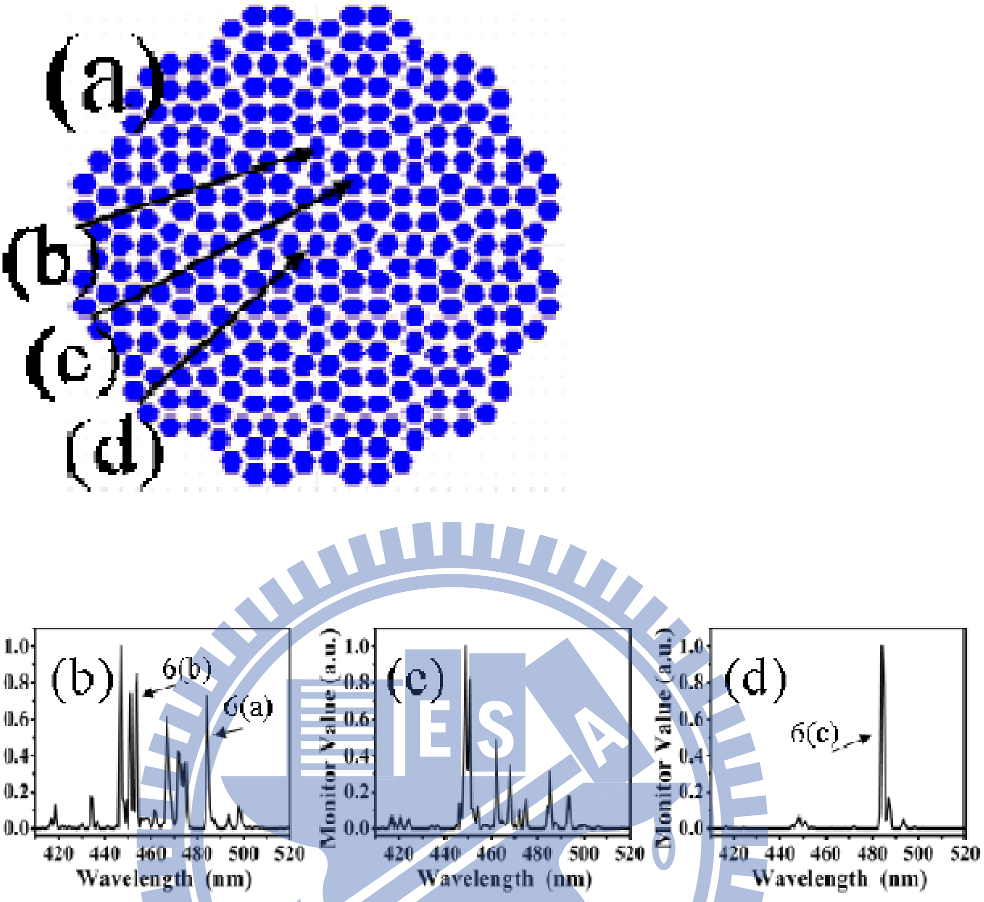

Figure 5-16. (a) The quasicrystal model used in FDTD simulation. (b)-(d) The resonant spectra obtained by launching broad band pulses at locations labeled correspondingly in Figure 5-16 (a).

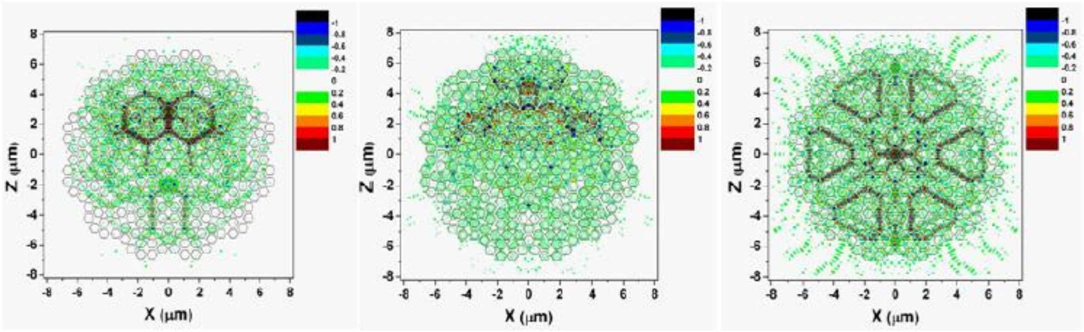

Figure 5-17. (a)-(c) Mode field patterns correspond to the resonant peaks labeled as 6(a), 6(b), and 6(c) in Figure 5-16.

Chapter 6

Electroluminescence Characteristics of 3-D Semipolar $\{10\bar{1}1\}$ Plane and Nonpolar $\{10\bar{1}0\}$ Plane Core-shell InGaN/GaN Multi-Facet Qunatum Wells Optoelectronic Devices

In GaN material system, compressively-strained active regions in InGaN LEDs exhibit both spontaneous and piezoelectric polarization charges, it is due to the hexagonal symmetry of GaN materials. The polarization charge induce a magnitude of MV/cm internal electric field (IEF) in the active region, and have the result of the efficiency droop at high injection current density and the decrease of radiative efficiency with an increasing emission wavelength (In content increasing). It can separate electrons and holes wave-function and increase electron leakage, the result are the low internal quantum efficiency (IQE) and efficiency droop [1]. The suppression of the IEF can increase IQE and the current density at which efficiency droop occurs, can be achieved by reducing the lattice mismatch in hetero-structures or growing them on semi-polar and non-polar surface. It is more advantageous to achieve long-wavelength green-amber LED on semipolar planes to suppress the IEF, it is because the indium incorporation is more difficult on non-polar than on semi-polar planes.

There are three approches to fabricating semi-polar or non-poalr InGaN LEDs have been reported. These include the growth of a GaN epilayer on spinel substrates [2], on bulk GaN substrates [3-11], and on the sidewalls of pyramidal or ridge GaN structures created on planar polar GaN surfaces using SAG [12-19]. There are exhibited a high density of threading dislocations and stacking faults of GaN grown on spinel substrates, thereby compromising the potential improvement of efficiency from the lowering of IEF. there are advantage of a lower IEF for the enhanced efficiency of green and yellow those using the bulk semi-polar GaN substrates [9,10]. But the high wafer cost and small substate size need to be resolved before this approcach can becore more pratical. On the other hand, the SAG technique can create semi-polar facet on polar GaN facet. The white-emission LED needs many basic components for solid-state lighting (SSL). It can be achieved by mixing various color components as shown in 錯誤！找不到參照來源。6-1, the visible color can generated either from the direct output of individual LEDs or from the phosphor. Nowadays, the general available white light LEDs usually consist of a blue LEDs and a yellow phosphor plate. It has been shown that InGaN-based blue LEDs could achieve external quantum efficiency in excess of 70% or higher [20, 21]. However, this di-chromatic configuration typically has a poor color rendering index (CRI) due to the lack of the green and the red components. The energy loss during down-conversion is the key limit of the luminous efficiency through the phosphor conversion process. The general illumination is require must achieve luminous efficiency in excess of 200 lm/W and a CRI in excess of 90, a further improvement in the blue LED efficiency and the use of tetra-chromatic configuration (blue + green + yellow +red) is necessary [22]. Unfortunately, the efficiency of both InGaN and AlInGaP LED decreases significantly in the green-yellow (500 – 800 nm) range. The efficiency gap is also known as “green gap” (錯誤！找不到參照來源。1). because the AlInGaP meterials have indirect bandgaps in the wavelength, it is crucial to significantly improve the luminous efficiency of green and yellow InGaN LED to achieve high-efficiency SSL.

6.1 The Light Extraction Efficiency Enhancement of 3-D Core-shell InGaN/GaN Multi-Facet Qunatum Wells on Semipolar $\{10\bar{1}1\}$ and Nonpolar $\{10\bar{1}0\}$ Plane

The photons are generated from the active region in LEDs, and the photons need to escape the device in order to be useful. When light travels from a medium with a higher refractive index to a medium with a lower refractive index, the total internal reflection (TIR) occurs at the interface. In InGaN LEDs, the TIR at LED surfaces can be re-absorbed by the active region or trapped in the device due to a wave-guiding effect. Only a few percent of photons generated from the active region can escape from the device surface for InGaN LED. It has been shown that surface textures on LED surfaces can reduce TIR and improve photon extraction efficiency as illustrated in **錯誤! 找不到參照來源。**6-2. There are many surface texturing techniques such as photonic crystal structures [23] and photo-electrochemical etching of GaN surface [24] have been introduced. And the photo-electrochemical etching of nitrogen-terminated GaN surface has been successfully implemented into commercial blue LEDs [25]. In this section, we used the FDTD method to calculate the far field for the Core-shell semipolar and nonpolar InGaN/GaN MQWs on GaN Nanorod LEDs.

First of all, Finite-Difference Time-Domain (FDTD) Method is introduced as following. **錯誤! 找不到參照來源。**6-3 shows the main steps taken in a 3D FDTD simulation. Initially, a 3D model is made to represent the physical structure, including conductors, dielectric and boundaries. Next an applied pulse, normally either a sine-wave or a Gaussian pulse, acts as the input stimulus at all the sources. Then at increments of time the E and H fields are calculated. After each increment the input electric field amplitude is calculated and the E and H fields are again recalculated. This continues until the E and H fields within the system decay to zero. After completing the simulation an FFT program extracts frequency information from the transient response. The location of the transient data depends on the required system response. For example to determine the reflection coefficient, the input and reflected waves at the sources are monitored. For a radiation pattern, points are taken in free-space around the structure. The FDTD method uses Maxwell's equations which define the propagation of an electromagnetic wave and the relationship between the electric and magnetic fields, these are:

$$\mu\frac{\delta \boldsymbol{H}}{\delta t} = -\nabla \times \boldsymbol{E} \tag{6.01}$$

$$\varepsilon\frac{\delta \boldsymbol{E}}{\delta t} + \boldsymbol{J} = \nabla \times \boldsymbol{H} \tag{6.02}$$

$$\nabla \cdot \boldsymbol{E} = \frac{\rho}{\varepsilon} \tag{6.03}$$

$$\nabla \cdot \boldsymbol{H} = 0 \tag{6.04}$$

For a uniform, isotropic and homogeneous media with no conduction current Maxwell's curl equations then become:

$$\mu\frac{\delta \boldsymbol{H}}{\delta t} = -\nabla \times \boldsymbol{E} \tag{6.05}$$

$$\varepsilon\frac{\delta \boldsymbol{E}}{\delta t} = \nabla \times \boldsymbol{H} \tag{6.06}$$

By applying appropriate boundary conditions on sources, conductors and mesh walls an approximate solution of these equations can be found over a finite three-dimensional domain. Taking an example of the first equation in the i direction gives:

$$\mu\frac{\Delta H_x}{\Delta t} = \frac{\Delta E_y}{\Delta z} - \frac{\Delta E_z}{\Delta y} \tag{6.07}$$

The central difference approximation is then used on both the time and space first-order partial differentiations to obtain discrete approximations. This gives:

$$\mu\frac{H^{n+1/2}_{x\,i,j,k} - H^{n-1/2}_{x\,i,j,k}}{\Delta T} = \frac{E^{n}_{y\,i,j,k} - E^{n}_{y\,i,j,k-1}}{\Delta z} - \frac{E^{n}_{z\,i,j,k} - E^{n}_{z\,i,j-1,k}}{\Delta y} \tag{6.08}$$

Rearranging gives:

$$H^{n+1/2}_{x\,i,j,k} = H^{n-1/2}_{x\,i,j,k} + \frac{\Delta t}{\mu\Delta z}\left[E^{n}_{y\,i,j,k} - E^{n}_{y\,i,j,k-1}\right] - \frac{\Delta t}{\mu\Delta y}\left[E^{n}_{z\,i,j,k} - E^{n}_{z\,i-1,j,k}\right] \tag{6.09}$$

The half time-steps indicate that E and H are calculated alternately to obtain central differences for the time derivatives. In total there are six equations similar to Equation (6.09). These define the E and H fields in the x, y and z directions and are given in Equations (6.10) and (6.11). The permittivity (ε) and the permeability (μ) values in these equations are set to approximate values depending on the location of each of the field component:

$$H^{n+1/2}_{x\,i,j,k} = H^{n-1/2}_{x\,i,j,k} + \frac{\Delta t}{\mu\Delta z}\left[E^{n}_{y\,i,j,k} - E^{n}_{y\,i,j,k-1}\right] - \frac{\Delta t}{\mu\Delta y}\left[E^{n}_{z\,i,j,k} - E^{n}_{z\,i-1,j,k}\right] \tag{6.10a}$$

$$H^{n+1/2}_{y\,i,j,k} = H^{n-1/2}_{y\,i,j,k} + \frac{\Delta t}{\mu\Delta x}\left[E^{n}_{z\,i,j,k} - E^{n}_{z\,i,j,k-1}\right] - \frac{\Delta t}{\mu\Delta z}\left[E^{n}_{x\,i,j,k} - E^{n}_{x\,i-1,j,k}\right] \tag{6.10b}$$

$$H^{n+1/2}_{z\,i,j,k} = H^{n-1/2}_{z\,i,j,k} + \frac{\Delta t}{\mu\Delta z}\left[E^{n}_{x\,i,j,k} - E^{n}_{x\,i,j,k-1}\right] - \frac{\Delta t}{\mu\Delta x}\left[E^{n}_{y\,i,j,k} - E^{n}_{y\,i-1,j,k}\right] \tag{6.10c}$$

$$E^{n+1/2}_{x\,i,j,k} = E^{n-1/2}_{x\,i,j,k} + \frac{\Delta t}{\varepsilon\Delta y}\left[H^{n+1/2}_{z\,i,j+1,k} - H^{n+1/2}_{y\,i,j,k}\right] - \frac{\Delta t}{\varepsilon\Delta z}\left[H^{n+1/2}_{y\,i,j,k} - H^{n+1/2}_{y\,i-1,j,k}\right] \tag{6.11a}$$

$$\boldsymbol{E}_{y\,i,j,k}^{n+1/2} = \boldsymbol{E}_{y\,i,j,k}^{n} + \frac{\Delta t}{\varepsilon \Delta z}\left[\boldsymbol{H}_{z\,i,j,k+1}^{n+1/2} - \boldsymbol{H}_{y\,i,j,k}^{n+1/2}\right] - \frac{\Delta t}{\varepsilon \Delta x}\left[\boldsymbol{H}_{y\,i,j,k+1}^{n+1/2} - \boldsymbol{H}_{y\,i,j,k}^{n+1/2}\right] \qquad (6.11b)$$

$$\boldsymbol{E}_{z\,i,j,k}^{n+1/2} = \boldsymbol{E}_{z\,i,j,k}^{n} + \frac{\Delta t}{\varepsilon \Delta x}\left[\boldsymbol{H}_{z\,i+1,j,k}^{n+1/2} - \boldsymbol{H}_{y\,i,j,k}^{n+1/2}\right] - \frac{\Delta t}{\varepsilon \Delta y}\left[\boldsymbol{H}_{y\,i,j+1,k}^{n+1/2} - \boldsymbol{H}_{x\,i,j,k}^{n+1/2}\right] \qquad (6.11c)$$

The input signal can be of any shape, but, it is normally a Gaussian pulse. This type of pulse has a frequency spectrum that is also Gaussian and thus has the advantage of providing frequency information from DC up to a desired cut-off frequency. The form of the input signal in a continuous form is expressed as:

$$f(t) = e^{-\frac{(t-t_0)}{T}} \qquad (6.12)$$

where t_0 is the pulse delay and T relates to the pulse width. Written in a discrete form gives:

$$f(nT_s) = e^{-\frac{(nT_S-mT_S)^2}{xT_S}} = e^{-\frac{(n-m)^2}{x}} \qquad (6.13)$$

where n is the current time-step, m the pulse delay time-step and x the width of the pulse in time-steps. Initially in the simulation, all the electric and magnetic fields are set to zero.

The maximum time step that may be used is limited by the stability restriction of the finite difference equations (6.02). This is given by:

$$\Delta t \leq \frac{1}{c}\left[\frac{1}{\Delta x^2} + \frac{1}{\Delta y^2} + \frac{1}{\Delta z^2}\right]^{-\frac{1}{2}} \qquad (6.14)$$

where c is the speed of light (3E8 m/s) and Δx, Δy and Δz are the dimensions of the unit element.

In the study, we used the FDTD method to calculate the far field for the Core-shell semipolar and nonpolar InGaN/GaN MQWs on GaN Nanorod LEDs. We used five types of different LED structures: First, the conversional LED is planar structure, which is a 5-μm thick GaN on flat sapphire. The simulation region is a 27-μm thick lateral length with period boundary condition, and a 8.5-μm thick vertical width with perfect match layer (PML) boundary condition. The position of the bottom boundary is 0.5-um thick from the sapphire/GaN interface, and the detector (time monitor) is covered over the GaN/air interface, the source is the dipole source with wavelength span from 400 to 700 nm, and is put away from the GaN/air interface 200 nm. The LED structure with pattern sapphire substrate (PSS) is the same as planar one, the pattern is about 2-μm, with 1-μm pitch and 1-μm height. The p-side rough is about 200-nm height of equilateral triangle at the interface of GaN/air, and the source is put with 150 nm from the concave. The pyramid LED is the same as our sample, and the pyramid-like rough LED is the same as the p-side rough, but replacing the height by the height of pyramid. The reflective index of GaN is 2.443 [26, 27] and sapphire is 1.78 [26].

The far-field intensity and angle were calculated by FDTD. The results of far-field were obtained those of near field (time monitor), as show in 錯誤! 找不到參照來源。. If we know E(x,y,z=0) and H(x,y,z=0), or E(x_s,y_s,z_s) and H(x_s,y_s,z_s) at the surface of the box, we can calculate E(x,y,z) and H(x,y,z), at any position (x,y,z>0), if the propagation material is homogeneous. The 錯誤! 找不到參照來源。 (a)-(e) are our diagram of simulation structure, and 錯誤! 找不到參照來源。 (a) is the output intensity versus wavelength, the oscillation of the planar is due to the fabry perot (FP) interference between the interface of GaN/sapphire and GaN/air. And the output intensity will compare with planar LED, the enhancement is calculus by the following equation:

$$\text{Enhancement} = \left(\frac{I_x}{I_{planar}} - 1\right) \times 100\% \tag{6-15}$$

As the result, the enhancement of PSS, p-side rough, pyramid-like rough and pyramid are about 45%, 37%, 142% and 147%, respectively. 錯誤! 找不到參照來源。 shows the distribution of far-field angle for each structure.

6.2 Electrical Properties of 3-D Core-shell InGaN/GaN Multi-Facet Qunatum Wells LEDs on Semipolar $\{10\bar{1}1\}$ and Nonpolar $\{10\bar{1}0\}$ Plane

Phosphor-free white-light-emitting diodes (LEDs), that can be fabricated on low-cost, large area substrates and can display high luminous flux, hold immense promise for the emerging solid-state lighting. Such devices can be realized monolithically by stacking blue, green, and red emitters in a single epitaxial step. They can exhibit much higher quantum efficiency, better color rendering capability, and significantly reduced manufacturing cost and improved reliability, compared to the commercial phosphor-based white LEDs [28]. Although tremendous progress has been made for InGaN/GaN quantum well LEDs, the performance of such devices in the green, yellow, and red wavelength ranges has been plagued by the very low efficiency and “efficiency droop”, i.e., the decrease of the external quantum efficiency with increasing current [29]. The underlying mechanism has been extensively investigated. Defects and carrier delocalization [30], polarization field [31, 32], Auger recombination [33], carrier leakage [34], and poor hole transport [35, 36] have been identified as some of the most probable causes. To this end, intensive studies have been performed with the use of various nanostructures, including quantum dots and nanowires [37, 38], which can exhibit drastically reduced dislocation densities and polarization field and can provide a greater degree of flexibility for sophisticated device engineering, compared to conventional planar heterostructures. Multicolor emission has been realized by using InGaN/GaN core-multi-shell and well/disk-in-a-wire structures and by exploring various hybrid nanowire heterostructures [39-42]. More recently, white light emission has been demonstrated in LEDs consisting of compositionally graded InGaN nanowires [43], InGaN/GaN nanodisks [44], and etched InGaN quantum wells [45].

However, a significant roadblock for the development of nanowire LEDs is the very low quantum efficiency. To date, there has been no report on the internal quantum efficiency of GaN-based nanowire LEDs under electrical injection. Due to the lack of three-dimensional carrier confinement, the radiative electron_hole recombination in the commonly reported GaN nanowire LED heterostructures has been severely limited by the presence of unoccupied Ga dangling bond and/or large densities of surface defects along the nonpolar GaN $\{10\bar{1}0\}$ surface (m-plane), which can lead to a Fermi-level pinning on the nanowire lateral surfaces. Additionally, the device performance is adversely affected by the poor hole injection and transport processes in InGaN/GaN nanoscale heterostructures, caused by the heavy effective mass, small mobility, and low concentration of holes. While electrons can exhibit a relatively uniform distribution across the entire active region, injected holes largely reside in the small region close to the p-doped GaN layer. The highly nonuniform carrier distribution also led to significantly enhanced Auger recombination and increased electron overflow, further limiting the optical emission efficiency at high injection levels. In this regard, special techniques, including p-doped active region, electron blocking layer, and thin InGaN barrier, have been implemented to improve the performance of conventional InGaN/GaN quantum well LEDs. However, such phenomena have not been recognized and addressed in the emerging nanowire LEDs by and large.

In addition to the planar blue Raf-LED, 3-D core-shell InGaN/GaN MQW LED structures were also demonstrated via heteroepitaxial growth on the top pyramids and sidewalls of n-type GaN nanorods fabricated by our top-down method. In Figure 6-8, the SiO_2 sidewall passivation coating was to prevent GaN from growing on the side walls in the epitaxial regrowth. Then, we reloaded our nanorod structure into MOCVD for the regrowth. It was worth noting in the beginning of regrowth process new semi-polar $\{10\bar{1}1\}$ facets and nonpolar $\{10\bar{1}0\}$ facets of n-GaN were formed at the tip and sidewall of the nanorods. Following growth of a six-period InGaN/GaN pre-strain stack on the nanorod sidewalls, a six-period InGaN/GaN MQW was formed at the tip and sidewall of the nanorods. Subsequently, a p-type GaN layer was grown following the MQW stack. As a result, the n-GaN nanorod was surrounded by the p-GaN and the MQW stack, leading to a 3-D core-shell radical InGaN/GaN LED structure, as shown in Figure 3a. We deposited continuous ITO layer on p-GaN layer. Then, standard device processing could be performed on this structure, leading to vertically-integrated, electrically-injected nanorod-based LEDs. In this context, we have investigated the epitaxial growth, fabrication, and characterization of 3-D self-organized Core-shell InGaN/GaN MQWs LED heterostructures can break the efficiency bottleneck of nanowire devices. Enlarging upon the results, a method to suppress the leakage path of nano-LED was introduced as depicted in Figure 6-8. With the use of SiO_2 sidewall passivation, we have successfully demonstrated phosphor-free white LEDs with a

CCT of 4000-8000k, which is attributed to the superior carrier confinement provided by the pyramidal semipolar $\{10\bar{1}1\}$ facet and hexagonal nonpolar $\{10\bar{1}0\}$ facet in Figure 6-9. The core-shell LED and conventional blue LED were fabricated into 300 μm x 300 μm LED chips by using standard fabrication. And we used Keithley 2601A as continuous wave current source. Figure 6-10 shows electroluminescence measurements from this electrically-inject nanorod-based core-shell LED. That exhibits red emission at lower drive currents and blue-shifts to green wavelengths at higher currents, indicating relatively high In incorporation in the MQWs. A smaller peak near 475 nm peak is also observed whose position is insensitive to drive current. The two different emission peaks may possibly be due to the MQWs on the non-polar vs. semi-polar facets. Spectacularly, the position of dominating peak is altered from red to green as increasing current in core-shell LED. It is investigated that optical characteristics of core-shell LED as a function of forward bias voltage in the visible range.

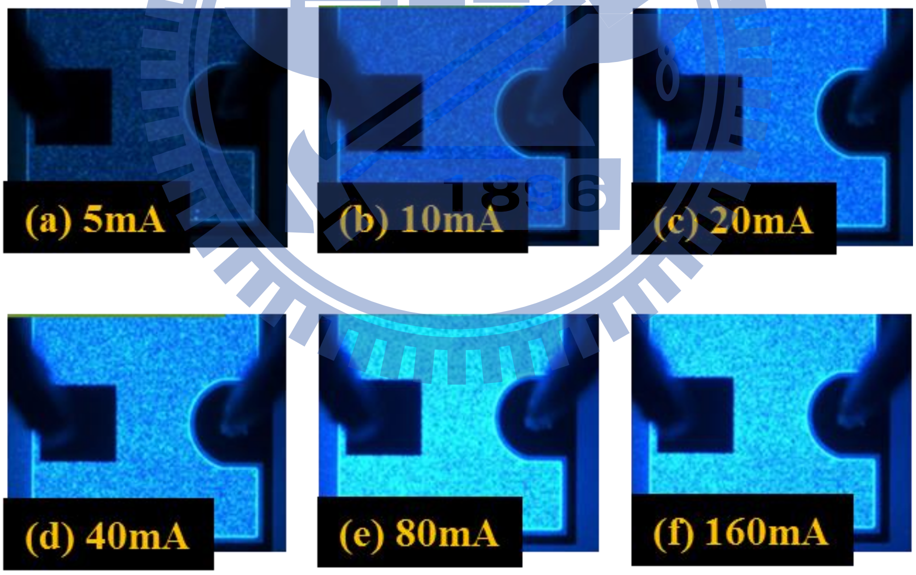

6-10 (a) depicted out the Vf = 2.65V at 20 mA with serial resistance (Rs) = 9.41Ω. It is attributed to the imperfection in the current spreading ITO layer on the corrugated 3-D pencil-like surface, which requires further optimization. The L-I curves show typical increasing output power as current increases. However, there is a slow turn on of light. It is considered that three possible mechanisms are dominant, including the narrowing of bandgap, the filling effect of localize state and current spreading of geometric electrical field. We believed that smaller turn-on voltage resulted from smaller emission energy and some extent of leakage current.

Along with an optical image of the emission, **錯誤！找不到參照來源。**11 depicted out the optical microscope of core-shell LED at a forward current of (a) 5mA, (b) 10mA, (c) 20mA, (d) 40mA, (e) 80mA, and (f) 160mA, respectively. Figure 6-12 shows a series of EL images taken at various bias voltage levels for the LED with a p - electrode area of 300 × 300 μ m ^{2}, exhibiting the gradual change in the emission color from red to green with increasing bias voltage. The light emission of the LED was further investigated by measuring the EL spectra at various bias voltages. Figure 6-12 shows that under an applied bias voltage of 2.2 V, the dominant EL emission was observed at 690 nm, corresponding to a red color, labeled (i). The EL color changed to orange, yellow, gold, amber, and green at 2.4, 2.6, 2.8, 3.0 and 3.2–3.6 V, respectively, consistent with the EL spectra. As the applied voltage increased up to 5.0 V, the EL peak position changed gradually from 690 to 500 nm, with another peak centered at 475 nm. The blue emission peak at 475 nm appeared as a shoulder at a bias voltage of 3.25 V, indicated as in Figure 6-10 (b). This visible-colortunable characteristic of the ocre-shell LEDs was quite distinct from that of thin-film LEDs grown in the same batch, which exhibited only a Blue EL of ≈ 460 nm with no considerable EL peak shift at various bias voltage levels (Figure 6-13). Furthermore, electrically pumped luminescence did not show any significant shift by changing the driving current in the range of 5–200 mA as shown in Figure 6-14, implying that the observed EL peak shift in the wide range may not result from the quantum-confinement Stark effect, which typically occurs in thin-film LEDs.

Based on the observations of the formation of anisotropic $In_xGa_{1-x}N$/GaN MQWs on the nanorods and current density dependent EL color, we suggested that the change of EL color can be qualitatively explained by the field distribution model presented in Figure 6-15. In order to know the reason of huge blue-shift, we proposed a current injection model of the 3-D geometric effect. Here, we used finite element method (FEM) to simulate the geometric effect. It is assumed that the p-type GaN is isoelectric for core-shell LED, and the electric field can be simulated as shown in 錯誤! 找不到參照來源。6-15. The 錯誤! 找不到參照來源。 (a) is the simulation region and structure, and (b) is the result of the electric field when we apply 0.5 V. 錯誤! 找不到參照來源。6-15 (c)-(g) are the simulation results under the forward bias of 1 V, 1.5 V, 2.0 V, 2.5 V, and 3.0 V. The result is a good fitting with our experiment in EL and CL, it is due to the geometric of the pencil-like structure. Due to the high resistivity of p-GaN (a few hundred times higher than that of n-GaN), at a low electric field near the turn-on voltage in Figure 6-15 (b), the current path forms preferentially through the p-GaN overlayer on the nanorod tips due to the locally enhanced potential drop around the nanorod tips. Accordingly, hole carriers in p-GaN converge primarily onto the topmost high In incooperation InGaN/GaN MQWs, emitting a red color. With increasing applied bias voltage, the equipotential plane shapes change into a curved surface along the tips (Figure 6-15 (c)-(f)), resulting in the gradual change of EL from red to cyan with a tail due to a buried long-wavelength EL ensemble. We noted that increasing forward bias caused a gradual broadening of FWHM values of EL peaks, supporting the field distribution model. A further increase in the electric field deforms the equipotential planes more significantly, as depicted in Figure 6-15 (b)-(f); higher current can flow into the gap space between the nanorods, contributing to the new blue EL from the $In_{0.15}Ga_{0.85}N$ MQWs formed on nanorod sidewalls. Similar to the field-emission diode, the field distribution may be tuned by adjusting the applied voltage, which defines the light-emitting region and color in the core-shell MQWs. Future work will be focused on optimizing the performance of core-shell LEDs.

6.3 Summary

From the FDTD simulation calculus, the pyramid structure have a great enhancement of 147% in comparison with the conversional structure (such as planar sapphire or PSS). And core-shell LEDs were fabricated using a conventional top-light emitting structure and measured using standard characterizations. The way to explain the phenomenon of large blue shift was to understand the mechanism of current spreading in this 3-D pencil-like structure. We proposed a new model to describe variation of electric field by FEM simulation. With increasing applied bias voltage, the equipotential plane shapes change into a curved surface along the tips (Figure 6-15 (c)-(f)), resulting in the gradual change of EL from red to green. As for the high current injection, higher current can flow into the gap space between the nanorod-based LEDs, contributing to the new blue EL from the nonpolar $In_{0.15}Ga_{0.85}N$ MQWs formed on core-shell sidewalls.

In summary, visible-color-tunable LEDs were fabricated using InxGa1-xN/GaN MQWs anisotropically formed on GaN nanostructures. The EL color of core-shell LEDs was simply controlled by adjusting the forward bias, which spanned almost the full visible-color range. Furthermore, we demonstrated monolithically integrated red, orange, yellow, gold, amber, and green LEDs that operated at a fixed drive current. The color tunable LEDs will enable significant advances for LED displays and many integrated optoelectronic devices.

6.4 References

[1] M. H. Kim, *et al.*, “Origin of efficiency droop in GaN-based light-emitting diodes,” *Appl. Phys. Lett.*, vol. **91**, p. 233504, 2007.

[2] T. J. Baker, *et al.*, “Characterization of planar semipolar gallium nitride films on spinel substrates,” *Jpn. J. Appl. Phys.*, vol. **44**, pp. L920-L922, 2005.

[3] M. Funato, *et al.*, “Blue, green, and amber InGaN/GaN light-emitting diodes on semipolar {11-22} GaN bulk substrates,” *Jpn. J. Appl. Phys.*, vol. **45**, pp. L659-L662, 2006.

[4] H. Zhong, *et al.*, “High power and high efficiency blue light emitting diode on freestanding semipolar (10-11) bulk GaN substrate,” *Appl. Phys. Lett.*, vol. **90**, p. 233504, 2007.

[5] H. Zhong, *et al.*, “Demonstration of high power blue-green light emitting diode on semipolar (11-22) bulk GaN substrate,” *Electronics Letters*, vol. 43, **pp**. 825-827, 2007.

[6] M. Ueda, *et al.*, “Epitaxial growth and optical properties of semipolar (11-22) GaN and InGaN/GaN quantum wells on GaN bulk substrates,” *Appl. Phys. Lett.*, vol. **89**, p. 211907, 2006.

[7] A. Tyagi, *et al.*, “High brightness violet InGaN/GaN light emitting diodes on semipolar (10-1-1) bulk GaN substrates,” *Jpn. J. Appl. Phys.*, vol. **46**, pp. L129-L131, 2007.

[8] R. Sharma, *et al.*, “Demonstration of a semipolar (10-1-3) InGaN/GaN green light emitting diode,” *Appl. Phys. Lett.*, vol. **87**, p. 231110, 2005.

[9] H. Sato, *et al.*, “Optical properties of yellow light-emitting diodes grown on semipolar (11-22) bulk GaN substrates,” *Appl. Phys. Lett.*, vol. **92**, p. 221110, 2008.

[10] H. Sato, *et al.*, “High power and high efficiency green light emitting diode on freestanding semipolar (11-22) bulk GaN substrate, *Physica Status Solidi-Rapid Research Letters*, vol. **1**, pp. 162-164, 2007.

[11] A. Chakraborty, *et al.*, “Growth and characterization of semipolar InGaN/GaN multiple quantum wells and light-emitting diodes on (10-1-1) GaN templates,” *GaN, AIN, InN and Related Materials*, vol. **892**, pp. 143-148, 2006..

[12] T. Wunderer, *et al.*, “Bright semipolar GaInN/GaN blue light emitting diode on side facets of selectively grown GaN stripes,” *Appl. Phys. Lett.*, vol. **89**, p.

041121, 2006.

[13] Y. Kawakami, *et al.*, “Light-emitting devices based on semipolar-oriented InGaN/GaN quantum wells,” *Proceedings of the 14th International Display Workshops*, vol. **1**, pp. 2345-2348, 2007.

[14] Y. Kawakami, *et al.*, “Efficient green emission from (11-22) InGaN/GaN quantum wells on GaN microfacets probed by scanning near field optical microscopy,” *Appl. Phys. Lett.*, vol. **90**, p. 261912, 2007.

[15] H. B. Yu, *et al.*, “Photoluminescence study of semipolar {10-11} InGaN/GaN multiple quantum wells grown by selective area Epitaxy,” *Appl. Phys. Lett.*, vol. **90**, p. 141906, 2007.

[16] T. Wunderer, *et al.*, “Blue-green semipolar GaInN/GaN light emitting diodes on {1-101} GaN side facets,” *Physica Status Solidi C*, vol **5**, pp. 2059-2062, 2008.

[17] T. Wunderer, *et al.*, “Time- and locally resolved photoluminescence of semipolar GaInN/GaN facet light emitting diodes,” *Appl. Phys. Lett.*, vol. **90**, p. 171123, 2007.

[18] K. Nishizuka, *et al.*, “Efficient radiative recombination from < 11-22 >-oriented InxGa1-xN multiple quantum wells fabricated by the regrowth technique,” *Appl. Phys. Lett.*, vol. **85**, pp. 3122-3124, 2004.

[19] M. Feneberg, *et al.*, “Polarized light emission from semipolar GaInN quantum wells on {1-101} GaN facets,” *J. Appl. Phys.*, vol. **101**, p. 053530, 2007.

[20] M. R. Krames, *et al.*, “Status and future of high-power light-emitting diodes for solid-state lighting,” J. Disp. Technol., vol. **3**, pp. 160-175, 2007.

[21] J. M. Phillips, *et al.*, “Research challenges to ultra-efficient inorganic solid-state lighting,” *Laser & Photonics Reviews*, vol. **1**, pp. 307-333, 2007.

[22] A. Bergh, *et al.*, “The promise and challenge of solid-state lighting,” *Physics Today*, vol. **54**, pp. 42-47, 2001.

[23] K. J. Byeon, *et al.*, “Fabrication of two-dimensional photonic crystal patterns on GaN-based light-emitting diodes using thermally curable monomer-based nanoimprint lithography,” *Appl. Phys. Lett.*, vol. **91**, p. 091106, 2007.

[24] T. Fujii, *et al.*, “Increase in the extraction efficiency of GaN-based light-emitting diodes via surface roughening,” *Appl. Phys. Lett.*, vol. **84**, pp. 855-857, 2004.

[25] J. M. Phillips, *et al.*, ‘Research challenges to ultra-efficient inorganic solid-state lighting,” *Laser & Photonics Reviews*, vol. **1**, pp. 307-333, 2007.

[26] M. Bass, *et al.*, Handbook of Optics, 3rd edition, Vol. 4. McGraw-Hill 2009

[27] A. S. Barker and M. Ilegems, “Infrared Lattice Vibrations and Free-Electron Dispersion in GaN,” *Phys. Rev. B*, vol. **7**, pp. 743–750, 1973.

[28] M. Shur, *et al.*, “Solid-state lighting: Toward superior illumination,” *Proc. IEEE*, vol. **93**, p. 1691, 2005.

[29] C. H. Wang, *et al.*, “Hole injection and efficiency droop improvement in InGaN/GaN light-emitting diodes by band-engineered electron blocking layer,” *Appl. Phys. Lett.*, vol. **97**, p. 261103, 2010.

[30] B. Monemar and B. E. Sernelius, “Defect related issues in the “current roll-off” in InGaN based light emitting diodes,” *Appl. Phys. Lett.*, vol. **91**, p. 181103, 2007.

[31] M. H. Kim, *et al.*, “Origin of efficiency droop in GaN-based light-emitting diodes,” *Appl. Phys. Lett.*, vol. **91**, p. 183507, 2007.

[32] M. F. Schubert, *et al.*, “Polarization-matched GaInN/AlGaInN multi-quantum-well light-emitting diodes with reduced efficiency droop,” *Appl. Phys. Lett.*, vol. **93**, p. 041102, 2008.

[33] Y. C. Shen, *et al.*, “Auger recombination in InGaN measured by photoluminescence,” *Appl. Phys. Lett.*, vol. **91**, p. 141101, 2007.

[34] K. J. Vampola, *et al.*, “Measurement of electron overflow in 450 nm InGaN light-emitting diode structures,” *Appl. Phys. Lett.*, vol. **94**, p. 061116, 2009.

[35] J. Q. Xie, *et al.*, “Origin of efficiency droop in GaN-based light-emitting diodes,” *Appl. Phys. Lett.*, vol. **93**, p. 121107, 2008.

[36] I. V. Rozhansky and D. A. Zakheim, “Analysis of the causes of the decrease in the electroluminescence efficiency of AlGaInN light-emitting-diode heterostructures at high pumping density,” *Semiconductors*, vol. **40**, p. 839, 2006.

[37] F. Qian, *et al.*, “Core/multishell nanowire heterostructures as multicolor, high-efficiency light-emitting diodes,” *Nano Lett.*, vol. **4**, p. 1975, 2004.

[38] A. Pan, *et al.*, “Spatial composition grading of quaternary ZnCdSSe alloy nanowires with tunable light emission between 350 and 710 nm on a single substrate,” *ACS Nano*, vol. **4**, p. 671, 2010.

[39] H. Kim, *et al.*, “Gallium nitride-based nanowire radial heterostructures for nanophotonics,” *Nano Lett.*, vol. **4**, p. 1059, 2004.

[40] K. Kishino, *et al.*, “InGaN/GaN multiple quantum disk nanocolumn light-emitting diodes grown on (111) Si substrate,” *Jpn. J. Appl. Phys.*, vol. **43**. P. L1524, 2004.

[41] X. M. Zhang, *et al.*, “Fabrication of a HB Blue LED Using a ZnO-Nanowire Array Grown on p-GaN Thin Film,” *Adv. Mater.*, vol. **21**, p. 2767, 2009.

[42] C. H. Lee, *et al.*, “GaN/In1−xGaxN/GaN/ZnO nanoarchitecture light emitting diode microarrays,” *Appl. Phys. Lett.*, vol. **94**, p. 213101, 2009.

[43] W. Guo, *et al.*, “Catalyst-free InGaN/GaN nanowire light emitting diodes grown on (001) silicon by molecular beam epitaxy,” Nano *Lett.*, vol. **10**, p. 3355, 2010.

[44] H. W. Lin, *et al.*, “InGaN/GaN nanorod array white light-emitting diode,” *Appl. Phys. Lett.*, vol. **97**, p. 073101, 2010.

[45] L. Y. Chen, *et al.*, “High performance InGaN/GaN nanorod light emitting diode arrays fabricated by nanosphere lithography and chemical mechanical polishing processes,” *Opt. Exp.*, vol. **18**, p. 7664, 2010 2010, ,.

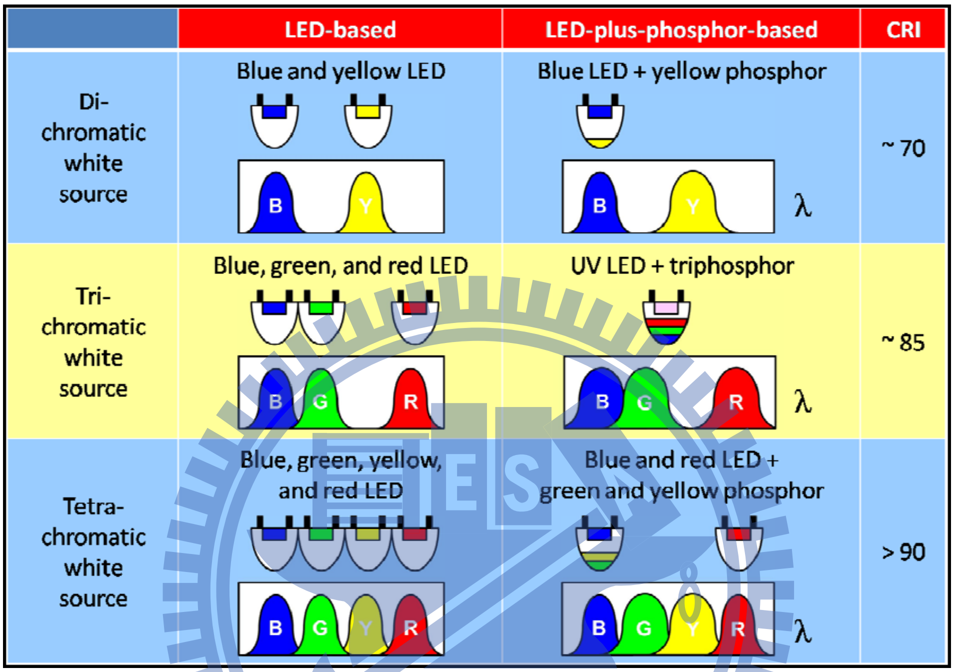

	LED-based	LED-plus-phosphor-based	CRI
Di-chromatic white source	Blue and yellow LED	Blue LED + yellow phosphor	~ 70
Tri-chromatic white source	Blue, green, and red LED	UV LED + triphosphor	~ 85
Tetra-chromatic white source	Blue, green, yellow, and red LED	Blue and red LED + green and yellow phosphor	> 90

Figure 6-1. Illustration of various potential white-light LEDs configurations [9].

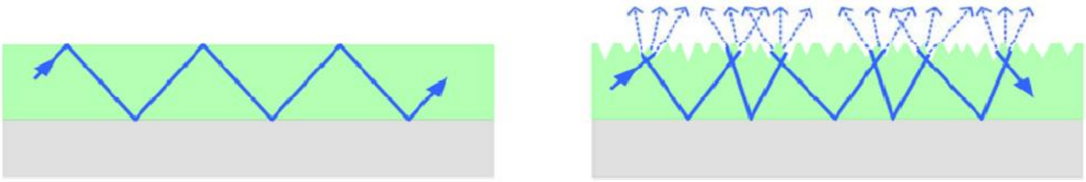

Figure 6-2. Light traveling within waveguides (left) with a smooth interface and (right) with a rough interface [1].

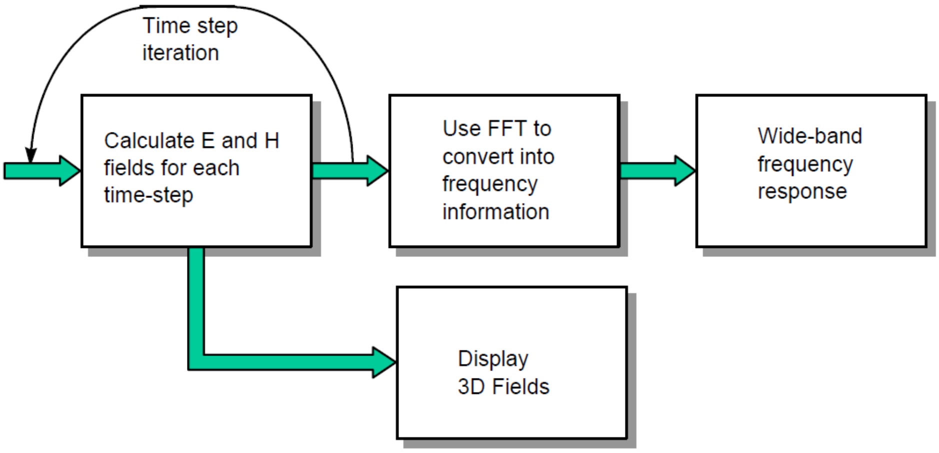

Figure 6-3. Simulation step of FDTD method.

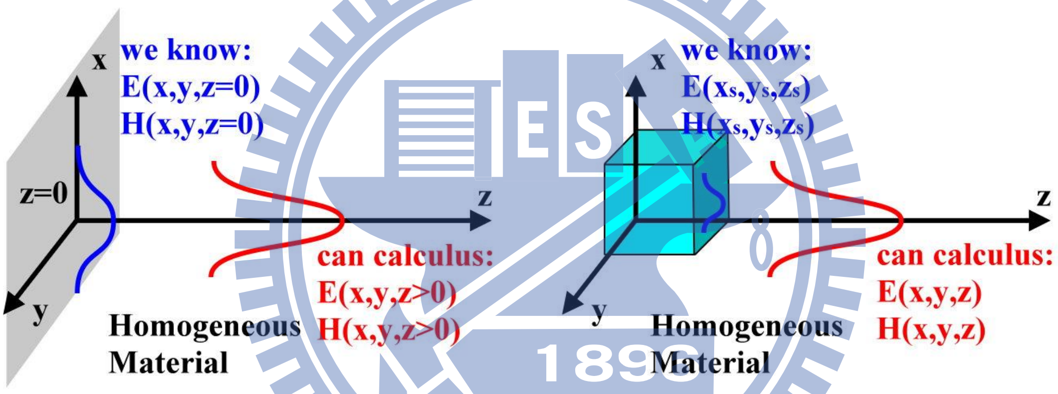

(a) (b)

Figure 6-4. FDTD calculus from near field transfer to far field.

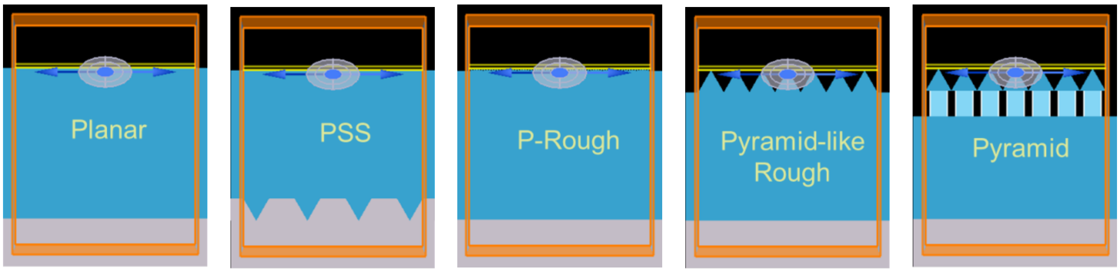

(a) (b) (c) (d) (e)

Figure 6-5. (a)-(e) are our diagram of simulation structure.

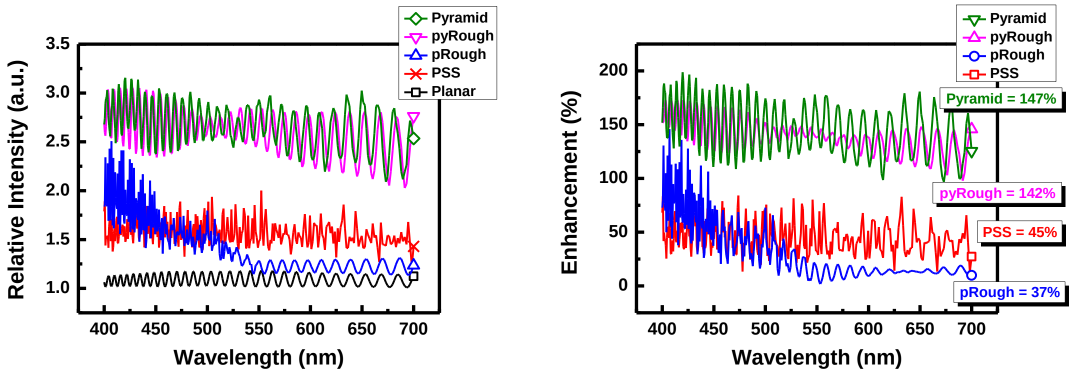

(a) (b)

Figure 6-6. (a) The output intensity various wavelength; (b) The enhancement of PSS, p-side rough, pyramid-like rough and pyramid.

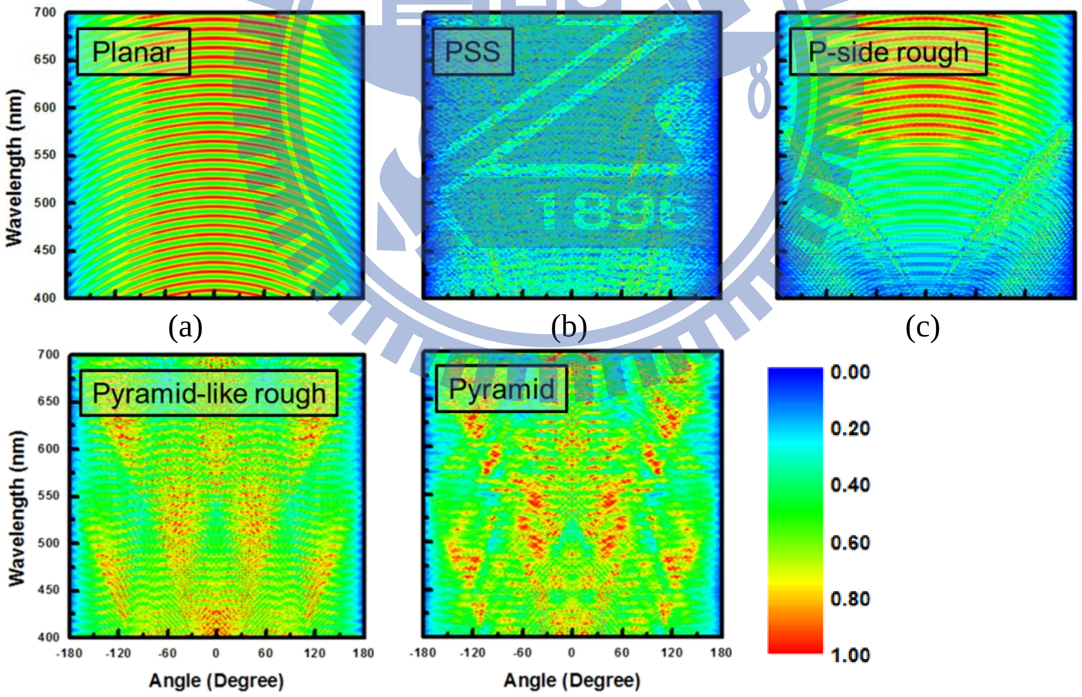

(a) (b) (c)

(d) (e)

Figure 6-7.The distribution of far-field angle for each structures

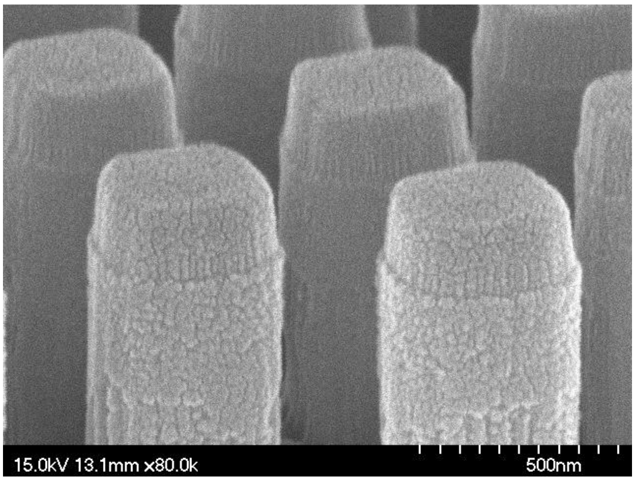

Figure 6-8. The SEM image of SiO_2 sidewall passivation

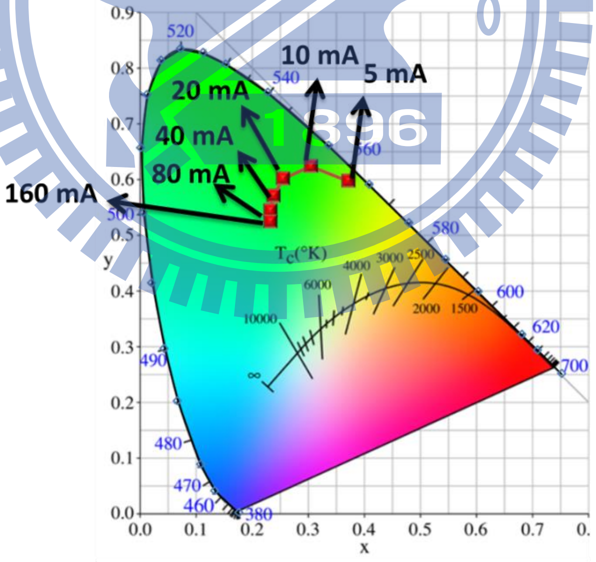

Figure 6-9. The emmision color of core-shell LED on CIE 1931 chromaticity diagram dependant on driving current of 5, 10, 20, 40, 80, 160 mA.

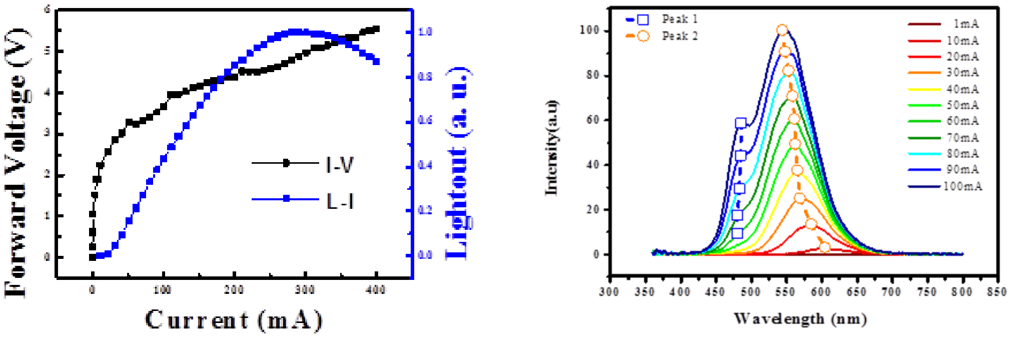

(a) (b)

Figure 6-10. (a) LIV Curve and (b) EL spectrum of the core-shell LED.

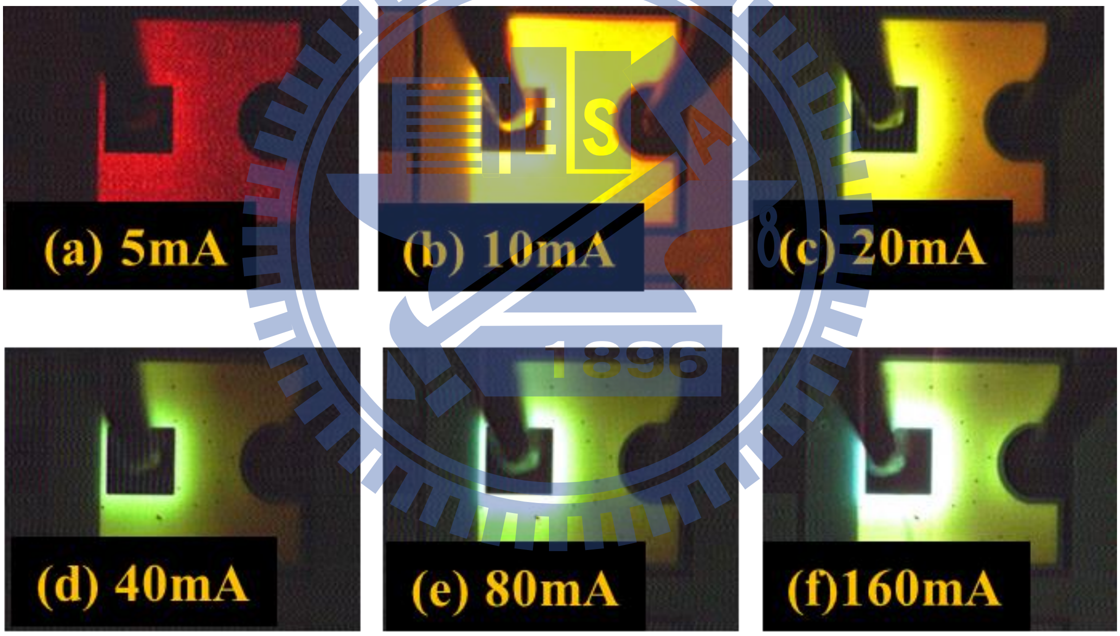

Figure 6-11. Light emission photographs of core-shell LED at a forward current of (a) 5mA, (b) 10mA, (c) 20mA, (d) 40mA, (e) 80mA, and (f) 160mA.

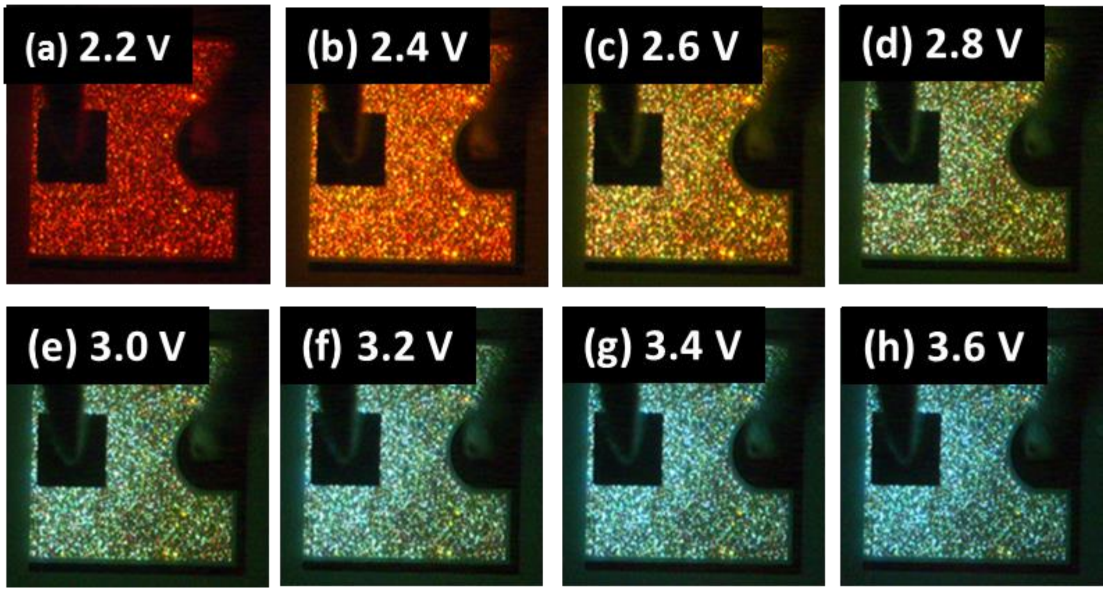

Figure 6-12. Light emission photographs of core-shell LED at a forward current of (a) 2.2 V, (b) 2.4 V, (c) 2.6 V, (d) 2.8 V, (e) 3.0 V, (f) 3.2 V, (g) 3.4 V, and (h) 3.6 V.

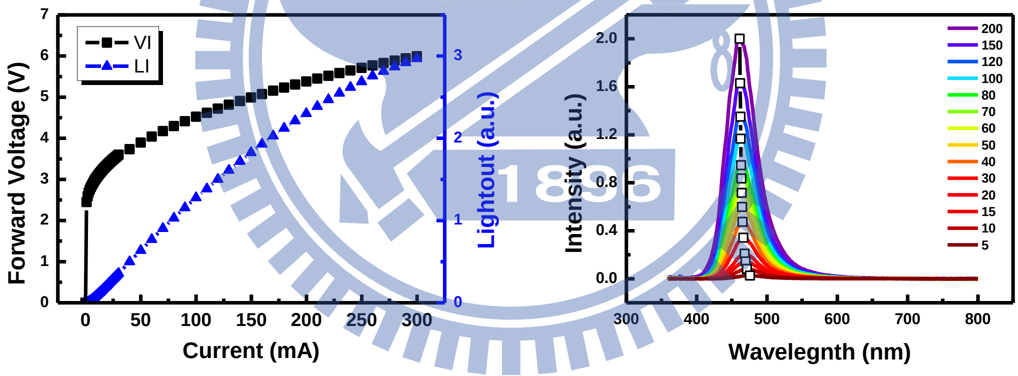

(a) (b)

Figure 6-13. (a) LIV Curve and (b) EL spectrum of Ref-LED.

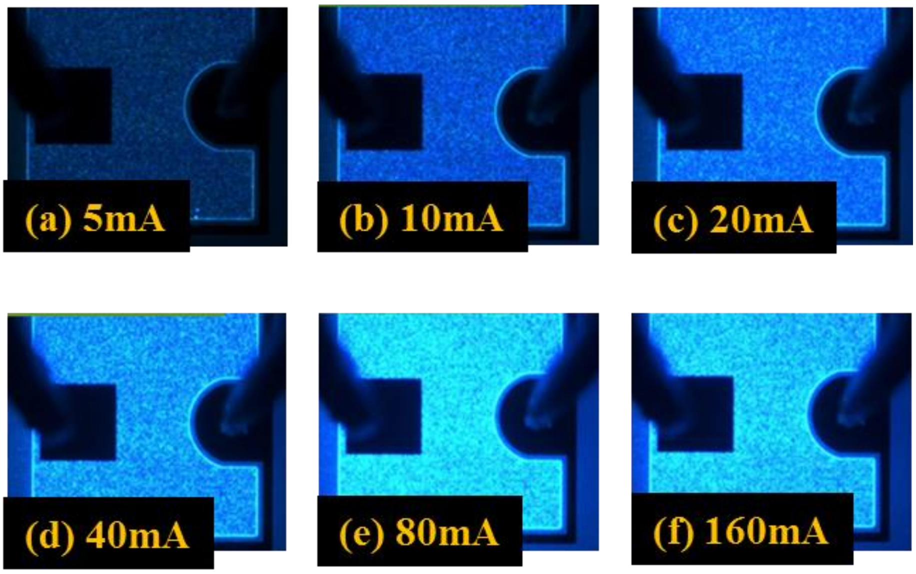

Figure 6-14. The optical microscope of polar blue LED at a forward current of (a) 5mA, (b) 10mA, (c) 20mA, (d) 40mA, (e) 80mA, (f) 160mA.

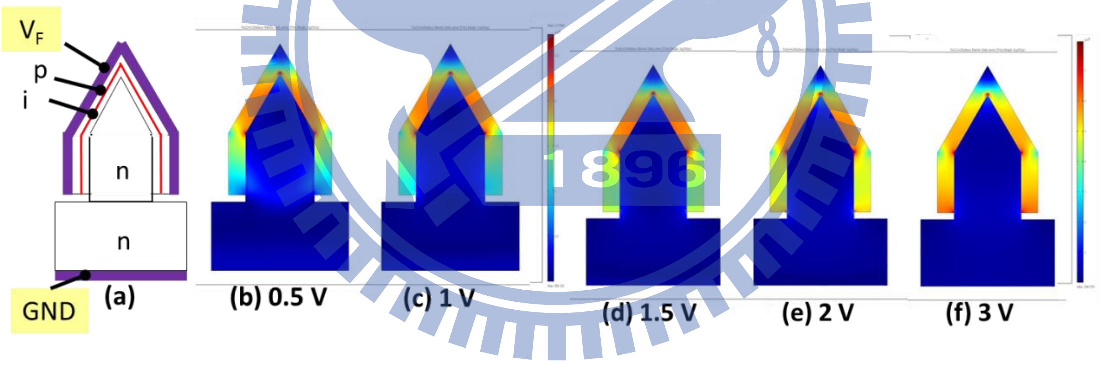

Figure 6-15. (a) The simulation region and structure; The geometric electrical field when applied voltage= (b) 0.5 V, (c) 1 V, (d) 1.5 V, (e) 2 V, and (f) 3 V.

Chapter 7

Conclusion

For top-down etching via the NIL process to translate 12-fold PQC pattern and eliminate dislocations on the template, the defect density was reduced at the magnitude of one order. The active area of core-shell nanorods under the regrowth process of MQWs is enlarged by a factor of 5. Also, we reported the observation of lasing action from an optically pumped gallium nitride quasicrystal nanorod arrays. The nanorods were fabricated from a GaN substrate by patterned etching, followed by epitaxial regrowth. The nanorods were arranged in a 12-fold symmetric quasicrystal pattern. The regrowth grew hexagonal crystalline facets and core-shell MQWs on nanorods. Under optical pumping, multiple lasing peaks resembling random lasing were observed. The lasing was identified to be from the emission of MQWs on the nanorod sidewalls. The resonant spectrum and mode field of the 12-fold symmetric photonic quasicrystal nanorod arrays is discussed. In addition, multiple lasing peaks emerged from broad emission background under optical pumping. The random laser action is achieved by the core-shell nanorod structure in the range of the wavelengths from 450 to 470 nm. The irregular multiple lasing peak wavelengths and the inverse dependence of threshold pump intensity on pump spot area shows the characteristics of a random laser. As a result, the polychromatic emission will be formed and the color temperature value can be tuned by the different regrowth parameters of MQWs nano-facets on nanorods.

Regarding to growth mechanism of core-shell semipolar and nonpolar InGaN/GaN multi-facets MQWs on GaN nanorods, two models are introduced to explain the different indium incorporation efficiency on core-shell nano-facets nanorods: First, the mass transport model is introduced to describe the indium incorporation efficiency of core-shell nanorods. The higher indium content of $\{10\bar{1}1\}$ planes compared to $\{1\bar{1}00\}$ planes, which is attributed to the different adatom reaction rate in the surface diffusion process. The adatom reaction rate is influenced by the density of atomic sites that are correlated with the surface energy. Therefore, the growth rate of the reactants on each facet was mainly influenced by the large surface energy with the large density of atomic sites. Because the surface energy of GaN $\{10\bar{1}1\}$ planes with 181.2 meV/Å^2 and $\{1\bar{1}00\}$ planes with 137.7 meV/Å^2, the higher incorporation efficiency was predictable for semipolar planes than nonpolar planes. In the other hand, the gradual indium content distribution on each facet is originated from the gas phase diffusion process. The accumulation of indium atoms was observed at the intersection of growth facets, such as the apex of nanorods, and the border region between $\{10\bar{1}1\}$ facets and $\{1\bar{1}00\}$ facets. Here, the second growth model of surface modification will be introduced to describe this phenomenon. The high accumulation at the intersection of facets can be ascribed to the chemical surface potential lowering by the nucleation process. Of note, asymmetrical thickness distribution for InGaN/GaN MQWs on the two $\{10\bar{1}1\}$ facets is observed in the TEM image. Due to $\{10\bar{1}1\}$ planes have an inclination angle of 62° relative to *c*-plane, the thick right-side inclination plane is the $\{10\bar{1}2\}$ facet. For the new-born $\{10\bar{1}2\}$ facets on $\{10\bar{1}1\}$ planes supposedly result in the tendency to minimize its total strain energy during growth process and increase the indium content. In addition, core-shell nanorods with the higher indium content can be attained by a reduced regrowth temperature of MQWs. Under a reduced regrowth temperature, the degraded sidewall surfaces of core-shell nanorods were caused by the lower species mobility with the lower temperature. We have observed a red shift as the location moves from the bottom to top portion of nanorods from the spatially resolved cathodeluminescence images. According to the APSYS modeling wavelength, cathodeluminescence images, the multiple peaks fitting from the PL spectrum, the internal electron field and its related indium content can be assigned to the location of core-shell nanorods. Furthermore, the internal electron field is found to be remarkably reduced by changing the growth planes from (0001) plane to $\{10\bar{1}1\}$ and $\{1\bar{1}00\}$ plane. As comparing with (0001) MQWs, the internal electron fields of $\{1\bar{1}00\}$ MQWs and $\{10\bar{1}1\}$ MQWs are remarkably reduced from 1.7 MV/cm to 0.02-0.4 MV/cm. Color temperature ~60,000 of sample HT is situated on the blue region of the CIE 1931 chromaticity diagram, whereas color temperature ~6,000 (a natural white light) of sample LT is situated on the white region. The tunable color temeprature is attainable by core-shell nanorods grew under a different regrowth temperature of MQWs.

In summary, we fabricated core-shell MQW nanopillar arrays by patterned top-down etching and a subsequent epitaxial regrowth. The regrowth results in crystalline hexagonal pyramid nanopillars with {10-10} nonpolar and {10-11} semipolar facets. The MQWs grown on these facets have large location dependent variations of In concentrations. The emission expands a broad spectrum from 420 to 520 nm. The PL emission spectrum remains fairly stable over two orders of carrier density change due to the low polarization field facets. The broad emission bandwidth and low polarization field make the core-shell MQW pillar structure an attractive design for LED lighting applications. For various electroluminescence colors, current injection paths were controlled through a continuous p-GaN layer depending on the applied bias voltage. Here, we report on the fabrication and characteristics of phosphor-free, monolithic, full-color, tunable LEDs, whose EL color can be tuned continuously from red to blue by adjusting the external electric bias. A phosphor-free white light emission is achieved by the core-shell nanorods technology. With a low regrowth temperature, core-shell LEDs have a natural white light with color temperature about 6,000K. In the future, the phosphor-free polychromatic emission LEDs are attainable by the core-shell LEDs.

Publication List

Journal Papers：

[1] **J. R. Chang**, T. H. Yang, J. T. Kua, S. G. Shen, Y. C. Chen, Y. Y. Wong, and C. Y. Chang, “GaN Growth on Si(111) Using Simultaneous AlN/Si3N4 Buffer Structure”, *Jpn. J. Appl. Phys.*, .**47**, 5572-5575 (2008).

[2] **J. R. Chang**, S. P. Chang, Y. J. Li, Y. J. Cheng, K. P. Sou, J. K. Huang, H. C. Kuo, and C. Y. Chang, “Fabrication and luminescent properties of core-shell InGaN/GaN multiple quantum wells on GaN nanopillars”, *Appl. Phys. Lett.*, **100**, 261103 (2012).

[3] **J. R. Chang**, S. P. Chang, K. P. Sou, M. C. Liu, Y. J. Cheng, H. C. Kuo, and C. Y. Chang, “Electrically Driven Green, Olivine, and Amber Color Nanopyramid Light Emitting Diodes”, pending to *Appl. Phys. Lett.* (2013).

[4] M.-C. Liu, Y.-J. Cheng, **J.-R. Chang**, S.-C. Hsu, and Chun-Yen Chang, “Optical properties of self assembled GaN polarity inversion domain boundary”, Appl. Phys. Lett. 99, 021103. (2011)

[5] S.-P. Chang, Y.-C. Chen, J.-K. Huang, Y.-J. Cheng, **J.-R. Chang**, K.-P. Sou, Y.-T. Kang, H.-C. Yang, T.-C. Hsu, H.-C. Kuo, and Chun-Yen Chang, “Electrically driven nanopyramid green light emitting diode”, Appl. Phys. Lett. 98, 211107. (2011)

[6] P. M. Tu, Chun-Yen Chang, S. C. Huang, C. H. Chiu, **J. R. Chang**, W.T. Chang, D.

S. Wuu, H. W. Zan, C. C. Lin, Hao-Chung Kuo, and C. P. Hsu, “Quaternary barrier cuts droop in UV LEDs”, Compound Semiconductor, 17, pp.37. (2011)

[7] P. M. Tu, Chun-Yen Chang, S. C. Huang, C. H. Chiu, **J. R. Chang**, W.T. Chang, D. S. Wuu, H. W. Zan, C. C. Lin, H. C. Kuo, and C. P. Hsu, “Investigation of efficiency droop for InGaN-based UV light-emitting diodes with InAlGaN barrier,” Appl. Phys. Lett., 98, 211107. (2011)

[8] Ching-Hsueh Chiu, Po-Min Tu, Chien-Chung Lin, Da-Wei Lin, Zhen-Yu Li, Kai-Lin Chuang, **Jet-Rung Chang**, Tien-Chang Lu, Hsiao-Wen Zan, Chiang-Yao Chen, Hao-Chung Kuo, Shing-Chung Wang, and Chun-Yen Chang, “Highly Efficient and Bright LEDs Overgrown on GaN Nanopillar Substrates”, IEEE JOURNAL OF SELECTED TOPICS IN QUANTUM ELECTRONICS, 17, 4, pp. 971 - 978. (2011)

[9] Jui-Tai Ku, Tsung-Hsi Yang, **Jet-Rung Chang**, Yuen-Yee Wong, Wu-Ching Chou, Chun-Yen Chang, and Chiang-Yao Chen, “Epitaxial Overgrowth of Gallium Nitride Nano-Rods on Silicon (111) Substrates by RF-Plasma-Assisted Molecular Beam Epitaxy” , Jpn. J. Appl. Phys., 49, 4, pp. 04DH06-04DH06-4. (2010)

[10] Y. Y. Wong, E. Y. Chang, T. H. Yang, **J. R. Chang**, J.K. Ku, M. K. Hudait, W. C. Chou, M. Chen, K.L. Lina, and Chun-Yen Chang, “The Roles of Threading Dislocations on Electrical Properties of AlGaN/GaN Heterostructure Grown by MBE”, Journal of The Electrochemical Society, 157, H746-H749. (2010)

[11] Yuen-Yee Wong, Edward Yi Chang, Tsung-Hsi Yang, **Jet-Rung Chang**, Jui-Tai Ku, Mantu K. Hudait, Wu-Ching Chou, Micheal Chen,f and Chun-Yen Chang,

"The Roles of Threading Dislocations on Electrical Properties of AlGaN/GaN Heterostructure Grown by MBE", Journal of The Electrochemical Society, 157, H746-H749. (2010).

[12] Yuen-Yee Wong, Edward Yi Chang, Tsung-Hsi Yang, **Jet-Rung Chang**, Yi-Cheng Chen, Jui-Tai Ku, Chun-Yen Chang and Chun-Wei Chang, "The effect of AlN buffer growth parameters on the defect structure of GaN grown on sapphire by plasma-assisted molecular beam epitaxy", Journal of Crystal Growth, 311, 1487–1492. (2009)

[13] T. H. Yang, J. T. Ku, **J. R. Chang**, S. G. Shen, Y. C. Chen, Y. Y. Wong, W. C. Chou, C. Y. Chen and Chun-Yen Chang, "Epitaxial Overgrowth of Gallium Nitride Nano-Rods on Silicon (111) Substrates by RF-Plasma-Assisted Molecular Beam Epitaxy", Journal of Crystal Growth, 311, 1997–2001. (2009)

Conference：

[1] **J. R. Chang**, T. H. Yang, S. G. Shen, Y. C. Chen, J. T. Kua, and C. Y. Chang, "The elimination of inversion domains in MBE-GaN grown using low temperature nitridation", *2007 Int. Conf. on Solid State Devices and Materials*, Ibaraki, Japan, September 18-21, 2007.

[2] **J. R. Chang**, T. H. Yang, Y. C. Chen, J. T. Kua, and C. Y. Chang, "Growth and Characterization of MBE-GaN on Si (111) using AlN/α-Si3N4 Buffer Structure", *213th ECS Meeting,* Phoenix, USA, May 18-22, 2008.

[3] **J. R. Chang**, T. H. Yang, S. G. Shen, J. T. Kua, and C. Y. Chang, “Study of GaN Nano-rods and Free-standing Layers Grown on Si(111) by Plasma-assisted Molecular Beam Epitaxy”, *2008 Int. Conf. on Solid State Devices and Materials*, Ibaraki, Japan, September 23-26, 2008.

[4] **J. R. Chang**, S. P. Chang, Y. J. Li, K. P. Sou, H. C. Kuo, and C. Y. Chang, “Electrically driven nanopyramid green light emitting diode”, *SPIE Photonics West 2012*, San Francisco, USA, Jan. 22-27, 2012.

[5] **J. R. Chang**, S. P. Chang, S. C. Lou, R. Xuan, Y. J. Cheng, H. C. Kuo, and C. Y. Chang, “Reduction of efficiency droop in InGaN light emitting diode by selective defect filtering”, *2007 International Workshop on Nitride Semiconductors*, Sapporo, Japan, Oct. 14-19, 2012.

Curriculum Vitae

Name: Jet-Rung Chang

Birthday: November 16th, 1982

Address: No.40, Xiangxing 3rd Ln., Sec. 2, Zhongxing Rd.
Dali Dist., Taichung City 412, Taiwan (R.O.C.)

Education:

National Taichung First Senior High School
(From September, 1998 to June 2001)

Department of Materials Science and Engineering, National Chiao Tung University
(From September, 2001 to June 2005)

Institute of Electronics, National Chiao Tung University
(From September, 2005 to May 2013)

Ph.D. Thesis:

Fabrication and Characterization of Three Dimensional Core-shell InGaN/GaN Multi-Facet Qunatum Wells Optoelectronics Devices on Semipolar $\{10\bar{1}1\}$ and Nonpolar $\{10\bar{1}0\}$ Plane